Max Planck Institute
for Intelligent Systems
Stuttgart

Novel X-ray Lenses for Direct and Coherent Imaging

Umut Tunca Sanlı

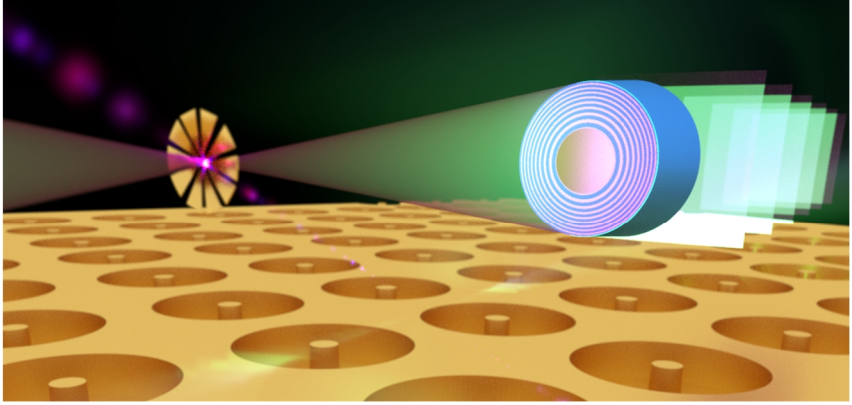

Dissertation an der
Universität Stuttgart

Novel X-ray Lenses for Direct and Coherent Imaging

Von der Fakultät Chemie der Universität Stuttgart zur Erlangung
der Würde eines Doktors der Naturwissenschaften
(Dr. rer. nat.) genehmigte Abhandlung

Vorgelegt von

UMUT TUNCA SANLI

aus Istanbul, Türkei

Hauptberichter:	Prof. Dr. Gisela Schütz
Mitberichter:	Prof. Dr. Joris van Slageren
Prüfungsvorsitzender:	Prof. Dr. Dr. h.c. Guido Schmitz
Tag der mündlichen Prüfung:	13. März 2019

Max-Planck-Institut für Intelligente Systeme, Stuttgart

2019

Table of Contents

List of Abbreviations

B	Magnetic field
c	Speed of light
d	Lattice spacing
e	Charge of electron
h	Planck's constant
$\hbar$	Reduced Plank's constant
λ	Wavelength
I	Intensity
γ	Lorenz factor
m_e	Mass of an electron
Δr	Outermost zone width

2PP	Two-photon polymerization
ALD	Atomic layer deposition
APD	Avalanche photodiode
BAM	Bundesanstalt für Materialforschung und Prüfung/ Federal Institute for Materials Research and Testing
BDEAS	Bis[diethylamino]silane
BESSY	Berliner Elektronenspeicherring-Gesellschaft für Synchrotronstrahlung - Berlin Electron Storage Ring Society for Synchrotron Radiation
CAD	Computer-aided design
CCD	Charge-coupled device
CRL	Compound refractive lens
CTF	Contrast transfer function

CWT	Coupled wave theory
DE	Diffraction efficiency
DLW	Direct laser writing
DOS	Density of states
EBID	Electron beam induced deposition
EBL	Electron-beam lithography
EDX	Energy-dispersive X-ray spectroscopy
EELS	Electron energy-loss spectroscopy
ePIE	Extended ptychographical iterative engine
EUV	Extreme ultraviolet
FEG	Field emission gun
FIB	Focused ion beam
FIBID	Focused ion beam induced deposition
FP-E	Full pixel exposure
FRC	Fourier ring correlation
FWHM	Full width at half maximum
FZP	Fresnel zone plate
GIS	Gas injection system
GPC	Growth per cycle
GS-IBL	Gray-scale ion beam lithography
GWL	General writing language
HAADF	High-angle annular dark-field
HHG	High harmonic generation
HRTEM	High-resolution transmission electron microscopy
IBL	Ion-beam lithography
IR	Infrared
KBM	Kirkpatrick-Baez mirror
LMIS	Liquid metal ion source
L:S	Line to space ratio

MAXYMUS	Magnetic X-ray microscope with UHV spectroscopy
ML-FZP	Multilayer Fresnel zone plate
MLL	Multilayer Laue lens
MP-E	Multi-pass exposure
NA	Numerical aperture
NEXAFS	Near edge X-ray absorption fine structure
OSA	Order-selecting aperture
PEALD	Plasma enhanced atomic layer deposition
PFIB	Plasma focused ion beam
REALD	Radical-enhanced atomic layer deposition
SASE	Self-amplified spontaneous emission
SEM	Scanning electron microscopy
SHARP	Scalable heterogeneous adaptive real-time ptychography
SP-E	Single-pass exposure
SS	Siemens Star
STEM	Scanning transmission electron microscopy
STXM	Scanning transmission X-ray microscopy
TEM	Transmission electron microscopy
TGA	Thin grating approximation
TMA	Trimethylaluminium
TXM	Transmission X-ray microscope
V-MACE	Vertical metal-assisted chemical etching
UV	Ultraviolet
VUV	Vacuum ultraviolet
WDX	Wavelength-dispersive X-ray spectroscopy
XFEL	X-ray free electron laser
XMCD	X-ray magnetic circular dichroism
XRM	X-ray microscopy

XPS	X-ray photoelectron spectroscopy
XRR	X-ray reflectometry

Zusammenfassung der Arbeit

Mit der Verfügbarkeit von modernen Synchrotronquellen, Freien Elektronen Lasern und der „High-Tech“ Erzeugung höherer Harmonischer mit Lasern hat sich die Nutzung zur Bildgebung zu einem leistungsfähigen Instrumentarium entwickelt in weiten naturwissenschaftlichen und technologischen Bereichen. Obwohl ihre kleinere Wellenlänge eine etwa 100-mal größere Auflösung als mit optischem Licht ermöglicht, erfordert ihr Brechungsindex, der nur 10^{-3} bis 10^{-6} von 1 abweicht, kompliziertere Strategien zu ihrer Fokussierung. Diese Anforderung an leistungsfähige Linsensysteme mit nanoskaligen Strukturen werden erfüllt durch die parallele Entwicklung von „top-down“ und „bottom-up“ Ansätzen in der Nanostrukturierung zur Realisierung leistungsfähiger Röntgenoptiken. In diesem Kontext, wie schon 1974 in ersten Röntgenmikroskopie-Studien gezeigt, wurde eine elegante Lösung durch das Fresnel-Zonenplatten (FZP)-Konzept gefunden. Mit lithographischen Herstellungsmethoden sind diese Optiken sehr leistungsfähig im weichen Röntgenbereich mit Auflösungen von ca. 20 – 30 nm. Allerdings ist ihre Effizienz zu klein für härtere Strahlung.

Ein moderner, heute vielfältig verfolgter Ansatz zur Erreichung der Wellenlängen-Begrenzung von wenigen nm und darunter basiert auf kohärenter Beugungsabbildung. Das aufgenommene Diffraktionsbild wird genutzt um das reale Bild mit einem iterativen Algorithmus zu rekonstruieren. Das sogenannte „Phasenproblem“ kann gelöst werden durch spezielle Techniken wie die Ptychographie. Der Fortschritt bei CCD Kameras und das schnelle Anwachsen von verfügbarer Rechenleistung machen diese Methoden äußerst attraktiv. Hierbei sind Optiken mit mittlerer Auflösung ausreichend, die Bildqualität hängt aber stark von der Linseneffizienz ab.

Im Rahmen dieser Promotion sind drei Ansätze erarbeitet worden um Fresnel-Zonenplatten für ausgewählte Anwendungen und Anforderungen hinsichtlich der Leistungsfähigkeit zu realisieren. Die Abbildungseigenschaften wurden untersucht an der

MAXYMUS Endstation bei BESSY II in Berlin, ein abteilungseigenes Instrument, ausgelegt für den weichen Röntgenbereich, das die besten Möglichkeiten für diese Aufgaben liefert.

Das erste Projekt war wesentlich verknüpft mit dem Ziel am MAXYMUS Endgerät Ptychographieverfahren zu implementieren. Hierfür wurden spezielle Entwürfe verschiedener FZP mit dem „Focused Ion Beam“ (FIB) Gerät am MPI-IS für die beste Qualität der ptychographischen Abbildung optimiert. In diesem Vorhaben wurde erkannt, dass der sog. „beamstop“ zur Ausblendung parasitärer Photonen eine entscheidende Rolle spielt. Diese Herausforderung wurde erfüllt in Kombination mit einer sehr großen aktiven Linsenfläche. Mit einer direkt gemessenen Effizienz von etwa 6 % haben diese Optiken den experimentellen Anforderungen exzellent genügt. Durch Nutzung dieser Linsen für Ptychographie wurde die maximale Auflösung von 4,9 nm erreicht, die nur durch die erreichbare Geometrie des UHV-Systems am MAXYMUS begrenzt wird. Darüber hinaus erlaubt die Präparationstechnik die Herstellung einer Linse in nur 30 min und FZP können mit maßgeschneiderten Abbildungseigenschaften für das jeweilige wissenschaftliche Projekt auf Bestellung in kürzester Zeit geliefert werden.

Die zweite Herausforderung war das sog. „bottom-up“ Verfahren zur Nanofabrikation von FZP mit Atomlagenabscheidung (ALD) auf Glasfasern und anschließendem FIB Schneiden und Dünnen für eine bessere Auflösung zu optimieren. Mit der gewählten Materialkombination HfO_2/Al_2O_3 wurde ein Rekord der Auflösung von 15 nm erreicht. Mit dieser Technik können vielfach FZP von der langen Glasfaser abgeschnitten werden mit unbegrenztem hohem Aspektverhältnis, was sie äußerst attraktiv für den Einsatz bei höheren Röntgenenergien macht. Generell gilt aber für eine Breite der äußersten Zonen unter $\sim$ 50 nm, dass die Bildqualität beträchtlich unter Wellenkopplungseffekten leidet. Auf der anderen Seite kann dieser Effekt vorteilhaft genutzt werden um durch eine Neigung der Zonen in die Braggbedingung die Effizienz der FZP entscheidend zu erhöhen. Dieses Konzept wurde übertragen und realisiert durch eine IBL Mikroherstellung eines Feldes von Gold-Mikrosäulen geeigneter Geometrie, worauf Al_2O_3/SiO_2 Zonen anschlie-

ßend mit ALD abgeschieden wurden. Anschließend wurden diese geneigten Multilagensysteme im FIB abgetrennt und als fokussierende Optiken präpariert. Dieser Prozess hat einige Vorteile gegenüber der Abscheidung auf Glasfasern. Zum einen kann der Durchmesser der Au Mikrosäulen genau kontrolliert und die Glätte der Wände besser garantiert werden im Vergleich zu den optischen Glasfasern. Zum anderen benötigt das System wegen des Goldkerns keinen „beamstop". Dadurch wird ein weiterer Präparationsschritt überflüssig und die parasitäre Abscheidung von Platin/Kohlenstoff auf den Zonen vermieden. Mit diesem ersten Versuch geneigte Multilagen FZP mit einer Breite der äußersten Zone von 20 nm herzustellen, wurde eine ptychographische Auflösung von 30 nm erzielt, die durch die noch geringe Effizienz der Optik (∼0,8 %) begrenzt war. Im Rahmen dieser ersten Versuche wurden jedoch erfolgversprechende Optimierungen erarbeitet.

Der dritte Ansatz war den 2-Photon-Polymerisation basierten 3D Nanodruck zu verwenden um erstmalig Kinoform FZP aus Plastik zu realisieren. Die genutzten Polymere haben exzellente optische Eigenschaften vergleichbar mit Diamant. Bei diesen parabolischen 3D Profilen wird eine Effizienz von bis zu 100 % theoretisch erwartet. Ihre Realisation mit „top-down" lithographischen Methoden ist aber extrem anspruchsvoll. Im Rahmen dieser Arbeit ist es gelungen exakte 3D Profile mit einer effektiven äußeren Zonenbreite von ∼ 400 nm in nur einer Minute herzustellen. Die Abbildungseigenschaften dieser neuartigen Kinoform FZP wurden in direkter Abbildung getestet und die erwartete Auflösung (half-pitch) von 240 nm erreicht, was die hohe Qualität der 3D Profile bestätigt. Extrem hohe Effizienzen von 20 % bei 1200 eV wurden in einem weiten Energiebereich von 800 bis 1800 eV erreicht. Diese Systeme sind hervorragende Optiken für Ptychographie, was entsprechend getestet und bestätigt wurde. Diese ersten Resultate für die Plastik FZP zeigen das große Potential dieser neuen, auf 3D Nanodruck basierten Strategie. Dies erlaubt in einer einfachen und schnellen Weise auch FZP Felder oder andere komplexe Fokussierungsoptiken auch für den harten Röntgenbereich herzustellen, was außerhalb der Möglichkeiten anderer Präparationmethoden liegt.

In allen drei Projekten wurden bedeutende Fortschritte zur Realisierung von leistungsfähigeren Fokussierungsoptiken für Röntgenstrahlen erzielt, die von Bedeutung für Anwendungen an den entsprechenden Großforschungseinrichtungen und zukünftigen Laborgeräten sind.

Abstract

With the advent of modern synchrotron sources, Free Electron Lasers (FELs) and high-end laboratory devices such as High Harmonic Generation (HHG) laser systems, the use of X-rays for imaging has become a powerful tool in a broad field of natural science and technology. Although the wavelength of X-rays can in principle provide >100 times higher resolutions than optical light, the real part of the complex index of refraction of most of the elements is only 10^{-3} – 10^{-6} smaller than unity in the X-ray regime, hence requires more sophisticated focusing strategies. The demands for high-performance lens systems with structures in the sub-µm scale are met by the development of top-down and bottom-up approaches in nanomanufacturing for realizing powerful X-ray optics. In this scenario, as already demonstrated in the first X-ray microscopy studies with sub-µm resolution in 1974, an elegant solution is found following the Fresnel Zone Plate (FZP) concept. With the use of lithographical production methods, FZPs have been very successful in the soft X-ray range with typical resolutions of about 20 – 30 nm. However, owing to the limited aspect ratio, their efficiencies are low for harder X-rays above 1 keV.

A modern and widely used approach towards the wavelength limit of a few nm or beyond is based on coherent diffraction imaging, where the recorded diffraction pattern is used to reconstruct a real image via an iterative feedback algorithm. The so-called “phase problem” can be overcome by using these coherent diffractive imaging techniques such as ptychography. The progress in X-ray CCD cameras and the immense increase of computing power led to a strong attraction to these methods. Here, optics with medium resolution are sufficient, but the imaging quality depends strongly on the available flux determined by the lens efficiency.

In the frame of this thesis, three different but highly complementary approaches have been worked out to realize FZPs for dedicated applications and demands concerning their performance. The focusing properties have been tested at the MAXYMUS end-

station at BESSY II, Berlin, which is run as the department's scientific instrument that offers the best possibilities for this task, however, limited to the soft X-ray energies.

The first project was vitally correlated with the goal to implement ptychographic techniques at the MAXYMUS end-station. Therefore, various FZPs with special designs were prepared using an in-house Focused Ion Beam (FIB) device. It was recognized that the beamstop to block the parasitic light plays an essential role in the performance of the ptychographic reconstruction. This challenge could be finally overcome with the development of a new beamstop fabrication technique. With a directly measured efficiency of about 6 %, the delivered optics met the experimental requirements excellently. By utilizing these lenses dedicated for ptychography, a maximum resolution of 4.9 nm was achieved, which was only limited by the available imaging geometries inside the UHV chamber of the MAXYMUS. Finally, the preparation route allows writing a single lens in about 30 minutes, which is important for providing in FZPs on-demand with tailored optical properties for supporting the X-ray microscopy science at MAXYMUS.

The second challenge was to optimize the bottom-up nanofabrication process of Atomic Layer Deposition (ALD) on optical glass fibers and subsequent FIB slicing towards improved resolution. With the chosen material combination of HfO_2/Al_2O_3, a record half-pitch resolution of 15 nm was achieved. With this technique, multiple FZPs can be cut out from a long fiber with unlimited aspect ratios, which make them very attractive for harder X-rays. In general, for outer-most zone widths below ~50 nm, imaging performance severely suffers by wave coupling effects. On the other hand, by tilting the zones to Bragg angle, this phenomena can be used in advantage for a substantial increase of the diffraction efficiency. A new concept for preparing conical substrates with precise tilt angles was put forth and achieved by IBL-micromachining of an array of gold micro-pillars of the proper shape, which were then coated by ALD with Al_2O_3/SiO_2 multilayers. Subsequently, multilayer stacks with tilted angles were cut out by FIB and prepared as focusing optics. This process has various advantages over using optical glass fibers. First of all, the geometry of the micro-pillars can be precisely controlled, and

sidewall smoothness can be ensured contrary to the case for optical fibers. Second, thanks to the use of single-crystal gold as the core material, the need for an additional beamstop can be eliminated. This improvement avoids an extra process step and the parasitic platinum/carbon mixture deposition on the zones. With this first trial to manufacture tilted multilayer FZPs with outermost zone width of 20 nm, a direct image resolution better than 30 nm was achieved which is limited by the efficiency of the optic (Efficiency ~0.8 %).

The third approach used two-photon polymerization based 3D printing to realize kinoform lenses out of plastic materials with a complex parabolic profile. The polymers used have excellent optical constants close to diamond. These 3D profiles are theoretically expected to achieve a 100 % diffraction efficiency but are extremely challenging to realize via top-down lithographic techniques. In the frame of this thesis, it was possible to print these exact 3D lenses with an effective outermost zone width of ~ 400 nm in only ~1 minute. The image performance of these novel kinoform FZPs was tested by direct imaging, and the expected half-pitch resolution of 240 nm was achieved, proving the high quality of the 3D profile. Extremely high efficiencies with maximum values of 20 % at 1200 eV were found in the energy range of 800 – 1800 eV making them excellent optics for ptychography as verified by the corresponding measurements. These first results on plastic FZPs demonstrate the enormous potential of these new routes based on direct nanoimprinting, which allows manufacturing in an easy and fast way also FZP arrays or other complex focusing systems even for hard X-rays that is out of reach for other nanofabrication techniques.

In all three projects, significant strides were made towards the realization of advanced X-ray focusing optics targeting applications both at large scale scientific facilities and future laboratory devices based X-ray science.

1. Introduction

1.1. Introduction to X-rays: A Brief History

In the late 1800s, various scientists working with accelerated electron beams in Crookes tubes realized a surprising effect: Photographic plates near Crookes tubes were fogged and dark even though not exposed to daylight, indicating the presence of invisible radiation. In 1895, Wilhelm C. Röntgen published his first systematic study on the phenomenon where he named them as X-rays, denoting to the unknown. He published his first X-ray absorption images of the human body parts and realized the potential of X-rays for medical use.[1,2]

Already in 1899 Haga and Wind experimented[3] diffraction effects of X-rays and estimated the wavelength to be $\lambda \sim 0.1$ nm. In 1912, following Max von Laue's proposals, Walter Friedrich and Paul Knipping observed the diffraction of X-rays from a crystal structure.[4] However it was W. L. Bragg and W. H. Bragg who established the relationship between the wavelength of the X-rays, their angle of incidence, and the crystal spacing, known as the Bragg law.[5]

A further challenge was establishing X-ray microscopy. Because the wavelengths of X-rays are so small (0.01 nm < λ < 10 nm), in theory, they could be focused to several orders of magnitude smaller dimensions compared to visible light ($\lambda_{visible} \sim 500$ nm). This indicated seeing smaller objects *via* microscopy and writing smaller patterns *via* lithography.

However, focusing X-rays is a very challenging task. Conventional refractive optics do not work for X-rays. This has two reasons. First, for X-rays the refractive index for all materials is slightly smaller but very close to unity, making single refractive lenses impractical for the X-ray regime. Second, the imaginary part of the refractive index, which defines the absorption, is large, especially for low energy (soft) X-rays, limiting the use of compound refractive lenses. Therefore, different approaches were considered.

Paul Kirkpatric and Albert Baez developed the first X-ray reflective optics in 1948, which are known as Kirkpatric-Baez mirrors (KBMs),[6] still used extensively at the synchrotron sources.

Another milestone in X-ray microscopy was the development of synchrotron sources. The first synchrotron-based X-ray microprobe was developed by Horowitz and Howell in 1972 which used a pinhole aperture as X-ray optic.[7] Later in 1976, Schmahl *et al.* built the first transmission X-ray microscope (TXM) that uses a Fresnel zone plate (FZP) as focusing optic and pioneered X-ray microscopy at the BESSY I.[8]

The development and advancement of the FZP optics in combination with highly brilliant synchrotron sources have been mainly responsible for the success of X-ray microscopy.

In the following sections, the properties of X-rays, X-ray matter interactions, X-ray sources, and X-ray optics will be discussed.

Properties of X-rays

The spectral limits of X-rays in the electromagnetic spectrum are loosely defined, and there is no consensus in the scientific community. In this thesis, the nomenclature of Attwood[9] will be used in defining the names and spectral limits of X-rays in the electromagnetic spectrum. A scientifically significant part of the electromagnetic spectrum, covering a region from gamma rays to radio waves is depicted in Figure 1.1. Photon energies from about 250 eV to about 2–3 keV are denoted as soft X-rays, and photon energies from about 2–3 keV to about 100 keV are denoted as hard X-rays. The indistinct region between soft and hard X-rays are sometimes named as tender X-rays.

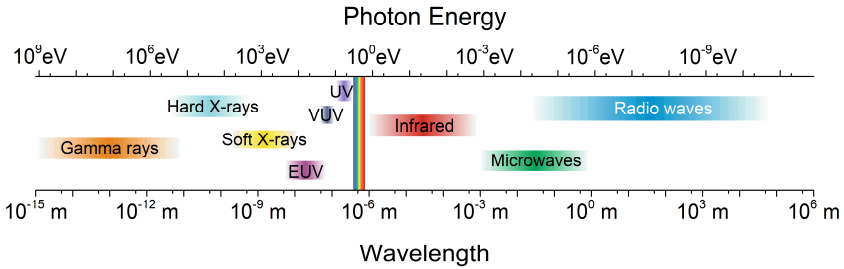

Figure 1.1 The electromagnetic spectrum. The shown regions with decreasing energy (and increasing wavelength) are, gamma rays*, hard X-rays, soft X-rays, extreme ultraviolet (EUV), vacuum ultraviolet (VUV), ultraviolet (UV), visible light (400–700 nm), infrared, microwaves and radio waves. Radiation with energies greater than EUV region is considered as ionizing radiation.

The correlation of photon energy and wavelength is given by the Planck-Einstein relation:

$$E = \frac{hc}{\lambda} = hf = \hbar\omega \tag{1.1}$$

where E is the photon energy, h is the Planck constant, c is the speed of light, and λ is the wavelength.

1.2. X-ray Interaction with Matter

1.2.1. Scattering

Scattering of radiation is a fundamental process. It happens on a submicroscopic scale, yet explains the propagation of light and macroscopic processes like transmission, reflection, and refraction.[10] In a broad definition scattering is the redirection of incident radiation over a very wide angular pattern.[9]

* Historically, electromagnetic radiation emitted by atomic nucleus are called gamma rays whereas radiation emitted by electrons are called X-rays. However, this is no longer valid as high-energy radiation can be produced without atomic nucleus.

The scattering of electromagnetic radiation from free electrons is called Thomson scattering.[11] For a free electron the oscillatory motion is given by Newton's second law of motion and the scattering cross-section is frequency independent.[9] Considering the semi-classical model, the equation of motion for a bound electron can be treated as a simple harmonic oscillator, with the positively charged nucleus acting as a restoring central force, causing a resonant frequency, ω_s.[9] The scattering cross-section depends on the frequency ω imposed by the incident photon and the resonant frequency, ω_s.[9] The Thomson model is related to the multi-electron atom by the atomic scattering factors.

Atomic Scattering Factors

Atomic-level interactions are described in terms of two atomic scattering factors, f_1^0 describing scattering and f_2^0 describing absorption. The frequency-dependent atomic scattering factor is given by:

$$f^0(\omega) = f_1^0(\omega) - if_2^0(\omega) \tag{1.2}$$

At very high photon energies (except the absorption edges), the binding energies become less significant, and electrons scatter like free electrons. Therefore f_1^0 asymptotes to atomic number Z and f_2^0 asymptotes to zero. Both f_1^0 and f_2^0 increases for higher atomic numbers. Sharp changes occur near absorption edges when the incident photons reach binding energies of inner atomic levels. The change of atomic scattering factors f_1^0 and f_2^0 as a function of photon energy for an aluminum atom is depicted in Figure 1.2 as an example.

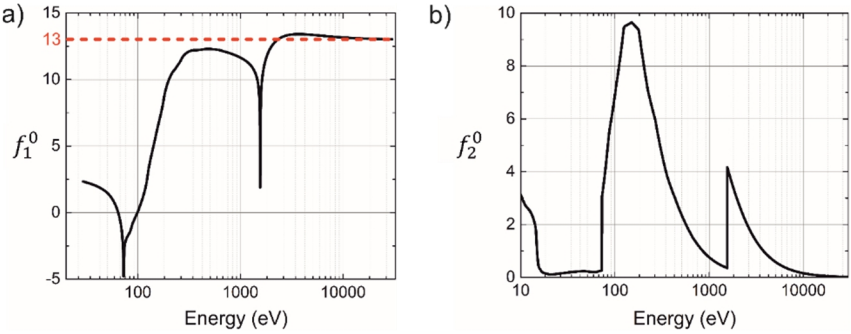

Figure 1.2 a) f_1^0, real part of the atomic scattering factor (related to scattering) and b) f_2^0, imaginary part of the atomic scattering factor (related to absorption) for aluminum atom as a function of photon energy. f_1^0 asymptotes to the atomic number of aluminum, Z=13, shown with red dashed line. Data were taken from http://henke.lbl.gov/, B.L. Henke, E.M. Gullikson, and J.C. Davis.[12]

Refractive Index

The complex refractive index is defined as:

$$n = 1 - \delta + i\beta \tag{1.3}$$

where the real part $1 - \delta$ corresponds to refraction and the imaginary part β corresponds to absorption. For the X-ray region, δ is generally very close to but slightly smaller than unity with values generally in the order of 10^{-6} to 10^{-2}. This has a very important consequence. Refraction of X-rays is very limited and single refractive lenses cannot be used to focus X-rays practically. The δ and β can be related to the atomic scattering factors by

$$\delta = \frac{n_a r_e \lambda^2}{2\pi} f_1^0(\omega) \tag{1.4}$$

and

$$\beta = \frac{n_a r_e \lambda^2}{2\pi} f_2^0(\omega) \tag{1.5}$$

where n_a is the number of atoms of type a per unit volume, r_e is the scattering cross-section, i.e., for a single electron, λ is the wavelength in vacuum. The combination of Eq. (1.4) and (1.5) gives the complex refractive index as a function of the two atomic scattering factors:

$$n = 1 - \frac{n_a r_e \lambda^2}{2\pi}(f_1^0(\omega) - i f_2^0(\omega)) \tag{1.6}$$

δ and β values as a function of X-ray energy are given for 2 different materials as an example in Figure 1.3. For higher energy X-rays δ/β ratio increases, which is essential for compound refractive lenses.

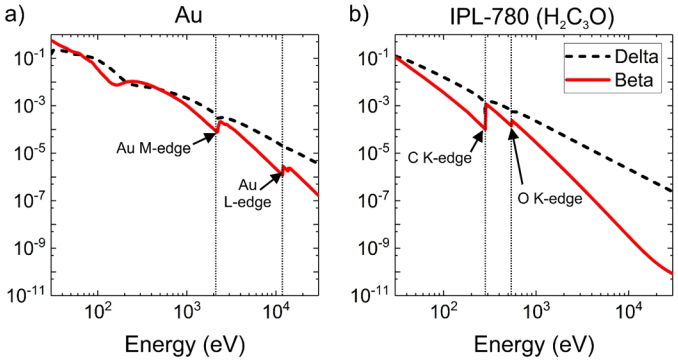

Figure 1.3 δ (Delta) and β (Beta) values as a function of photon energy for a) gold with a density of 19.32 g/cm³, b) H_2C_3O with a density of 1.50 g/cm³. Data were taken from http://henke.lbl.gov/, B.L. Henke, E.M. Gullikson, and J.C. Davis.[12]

1.2.2. Interference, Diffraction, Refraction, and Reflection

When two or more waves are incident on the same point, the resulting wave will have an amplitude equal to the vector sum of the amplitudes of the individual waves. This phenomenon is known as interference. If it happens between two plane waves of the same frequency, an interference pattern will be observed with areas of constructive and

destructive interference. Interference should be considered as a non-localized phenomenon, where constructive and destructive interferences are energy redistribution processes.[10]

Diffraction is the redirection of incident radiation either by an ordered array of scatters, such as atoms in a crystal structure or a well-defined geometric shape, such as a slit or a sharp edge.

An example to diffraction from a crystal structure with interference is the Bragg Diffraction. The Bragg's Law states, for a wavelength λ and crystal lattice spacing d, and angle θ, constructive interference will occur under the condition:

$$n\lambda = 2dsin\theta \tag{1.7}$$

where n is a positive integer and θ the angle of diffraction. The equation is illustrated in Figure 1.4.

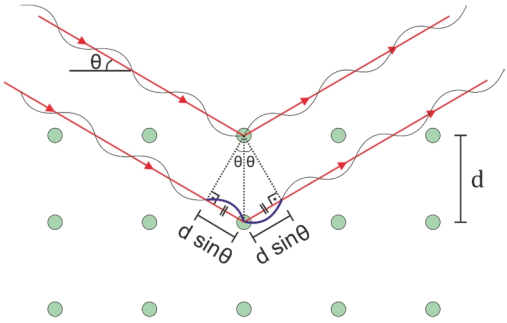

Figure 1.4 Bragg's Law. Constructive interference occurs when Bragg's Law is satisfied.

A classic example to diffraction from a geometric shape with interference is Young's double-slit experiment. The FZP is an advanced example of multiple slit diffraction with interference.

In a dense homogeneous medium, the scattered wavelets will interfere in the forward direction in a repetitive process. Each scattering (and re-scattering) process will

induce a phase shift and a consequent change in phase velocity depending on the wavelength and the medium. If the light beam passes through this interface at an angle, the change of phase velocity will cause the light beam to be bent. The bending of the light beam is known as refraction.[9,10]

When traveling wavelets encounter an interface between two transparent medium of different refractive index, some of the scattered wavelets will have constructive interference in the backward direction. This phenomenon is known as reflection.

1.2.3. Absorption

When a beam of electromagnetic radiation passes through a material its intensity is exponentially attenuated following the Beer-Lambert law:

$$I = I_0 e^{-\rho \mu x} \tag{1.8}$$

where I_0 is the incident intensity, ρ is the volumetric mass density, μ is the mass absorption coefficient, and x is the material thickness.

For soft X-rays, the contribution of scattering effects to attenuation is mostly negligible. The dominant process of attenuation is X-ray absorption. The energy dependence of absorption has two characteristics. The first behavior is a quasi-steady decay of absorption with increasing energy roughly proportional to E^{-3}. The second behavior is the sharp increase in absorption with increasing photon energy. When the photon energies reach binding energies of different atomic levels, they will be absorbed by photoelectric absorption, transferring all their energy to the atomic electron leaving behind an ionized atom resulting in element characteristic absorption edges.

In the X-ray energy region lies the absorption edges of most of the elements. This allows X-rays to be used for elemental and chemical identification. Especially soft X-rays are absorbed in very short distances (see Table 1.1). The K- and L_{23}- absorption edges (which are transitions of $1s \rightarrow (2)p_{1/2}$ and $(2)p_{3/2} \rightarrow (3)d$ following dipole selection rules) of selected elements, and the attenuation lengths for 1 keV and 10 keV X-rays are listed in Table 1.1.

Table 1.1. K- and L_3- absorption edges for selected elements. Retabulated from Attwood[9] with permission.

				Attenuation length (μm)	
Element	**Z**	**K-edge (eV)**	**L_3-edge (eV)**	**1 keV**	**10 keV**
Be	4	112	-	9.0	9600
C	6	284	-	2.1	2100
N	7	410	-	-	-
O	8	543	-	-	-
H_2O	-	-	-	2.3	2000
Al	13	1,560	73	3.1	160
Si	14	1,839	99	2.7	130
S	16	2,472	163	1.9	100
Ca	20	4,039	346	1.3	69
Ti	22	4,966	454	0.38	20
V	23	5,465	512	0.26	14
Cr	24	5,989	574	0.19	10
Fe	26	7,112	707	0.14	7.4
Ni	28	8,333	853	0.11	5.4
Cu	29	8,979	933	0.10	5.1
Se	34	12,658	1,434	0.96	52
Mo	42	20,000	2,520	0.19	12
Sn	50	29,200	3,929	0.17	11
Xe	54	34,561	4,782	-	-
W	74	69,525	10,207	0.13	5.6
Au	79	80,725	11,919	0.10	4.5

1.2.4. Near Edge X-ray Absorption Fine Structure

Near Edge X-ray Absorption Fine Structure (NEXAFS) is a spectroscopy technique based on energy-dependent absorption behavior of X-rays in matter around the absorption edges. The absorption coefficient of a material can be precisely measured by transmission experiments. Following the Fermi's Golden Rule the energy-dependent absorption coefficient can be related to the density of the final states (DOS) by,

$$\mu(E) \propto |M_{fi}(E)|^2 \cdot \rho(E) \tag{1.9}$$

where $M_{fi}(E)$ is the energy-dependent dipole transition matrix element from the initial (core) state to the final (photo-electron) state and $\rho(E)$ is the energy-dependent density of the final states.[13]

In a small energy range around the absorption edge up to about 20 eV, the transition matrix element can be considered to be constant. Thus, with an experiment mapping the energy dependence of X-ray absorption in the near edge, one can estimate the unoccupied DOS, which is directly correlated to the chemical state of the atomic species.

1.2.5. X-ray Circular Magnetic Dichroism

X-ray magnetic circular dichroism (XMCD) is a powerful experimental technique for characterizing the magnetic properties of materials. It depends on the physical phenomena of dichroism, which refers to the difference in the absorption of polarized light in a material due to its direction of polarization.[14] The origin of XMCD can be understood in a simplified two-step model. An example explanation for the two-step model for 3d $L_{2,3}$ transition metals is as follows:

Step 1: Conservation of Angular Momentum

When a circularly polarized photon is absorbed, its angular momentum will be transferred to the generated photoelectron as spin polarization. The spin direction of the photo-electron depends on the handedness of the polarization of the absorbed photon. For the 2p initial state of, e.g. 3d transition metals, spin-orbit coupling causes a split into two spin-orbit partner levels, $2p_{1/2}$ $(l-s)$ and $2p_{3/2}$ $(l+s)$ which are the initial states for the L_2 and L_3 absorption edges, respectively. The quantum mechanical vector couplings have to be calculated by *Clebsch-Gordan* coefficients.[15] Absorption of a right circularly polarized photon in an initial $p_{1/2}$ spin orbit state will give a photoelectron with a spin polarization of $\langle S\rangle = -\frac{1}{2}$ and an orbital polarization of $\langle L\rangle = \frac{3}{2}$.

Step 2: Selective Occupation of Exchange Spin-split Bands

For example, in ferromagnetic metals, the d band is split into minority (spin down) and majority (spin-up) states with different DOS due to a shift in energy with respect to each other. 'Pauli Exclusion Principle' suggests that electrons with the same spin have to avoid each other. This limits the spin-polarized photo-electrons excited in the first step to one of the split-states depending on their spin direction. As a consequence, the absorption cross-section is spin-dependent. Thus the XMCD effect is given with a modified version of Eq. (1.9) in which the spin-dependent DOS are included[13]:

$$\Delta\mu(E) = \mu^{-}(E) - \mu^{+}(E) \sim (\rho^{-} - \rho^{+})|M_{fi}(E)|^2 \qquad (1.10)$$

A unique feature of the XMCD is its capability to determine the spin (ρ^{spin}) and orbital (ρ^{orb}) contributions of the magnetic moments individually on the base of the sum rules. This is done by using the spin-orbit split nature of the elements. Excitations from the spin-orbit split L_2 and L_3 edges give two different XMCD spectra which can be elegantly used to solve for the two unknowns ρ^{spin} and ρ^{orb}.

1.3. Sources of High Energy Radiation

1.3.1. Laboratory Size X-ray Sources

X-ray Tubes

Electron matter interactions result in X-ray emission by two main processes: Bremsstrahlung and characteristic radiation. Bremsstrahlung occurs when an electron with a kinetic energy E_k decelerates because of the Coulomb field of the nucleus. The emission spectrum is a broad continuum, and the wavelength is limited on the lower edge (λ_{min}) by the kinetic energy of the incident electron. Characteristic radiation takes place when the incident electron is energetic enough to knock-out an electron from the inner atomic shells of the target element, thus creating a vacancy, which is subsequently filled

by an outer-shell electron. This relaxation process creates an intense X-ray fluorescence with a narrow bandwidth. A schematic drawing of bremsstrahlung and characteristic emission spectrum is depicted in Figure 1.5.

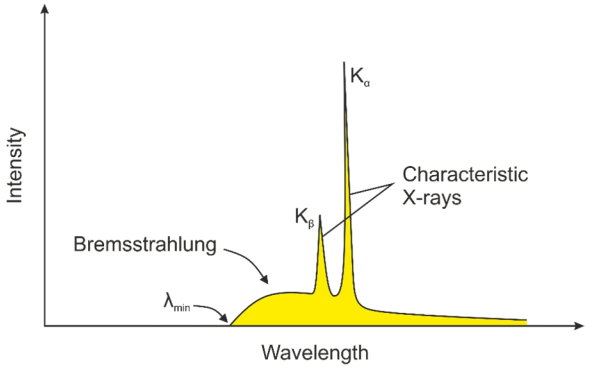

Figure 1.5 Schematic drawing of bremsstrahlung and characteristic X-ray emissions as a function of wavelength and intensity. The bremsstrahlung emission is a broad continuum. On the other hand K_α and K_β emissions constitute a characteristic narrow bandwidth.

The most common X-ray laboratory sources are the electron impact X-ray sources, where electrons generated by a hot cathode are accelerated to the target metal (anode) in a vacuum tube to generate bremsstrahlung and characteristic X-rays. Cu, Ga, Mo, In, and W have found widespread use as target metals. The conventional design has been based on a solid target or a rotating anode with electron beam power densities limited by the thermal load.

Liquid metal anodes were developed to overcome the thermal limitations offering several orders of magnitude higher brightness.[16] The commercial liquid metal jet devices use either a Ga-rich or an In-rich alloy as the anode material to generate characteristic X-rays of 9.2 and 24.2 keV respectively.

Hot Dense Plasmas

Another X-ray generation method is based on hot dense plasmas. Owing to high temperatures combined with high densities, hot dense plasmas are bright sources of EUV and soft X-rays. The emitted radiation from a hot dense plasma often has a broad spectral continuum as well as line emission originating from the element used for the plasma generation. Typical electron temperatures in a plasma range between 10^5 to 10^7 K.

High Harmonic Generation

A third method to create EUV or soft X-rays is by illuminating a noble gas with an intense (10^{14} – 10^{15} W/cm^2), infrared (IR), femtosecond pulsed laser. The electric field of the intense pulsed laser causes bound electrons to be tunneled through the barrier to become a free electron. The free electron is then accelerated by the electric field of the laser. When the electric field reverses, the electron may travel back to its bound state with additional kinetic energy. Consequently, radiative recombination may occur with a photon energy that is the sum of the ionization energy and the kinetic energy of the accelerated electron. This energy can reach up to several keV depending on the order of the harmonic. This process is called high harmonic generation (HHG). As the starting laser is femtosecond pulsed, the X-rays emitted in a single pulse in the HHG process constitutes a high peak spectral brightness with a short duration, suited well for dynamical measurements.

1.3.2. Synchrotron Radiation

Synchrotron Radiation using Bending Magnet

When a relativistic electron travels under a uniform magnetic field following a circular path, it will emit radiation in a tangentially outward direction with a narrow cone shape.[9] When the electrons are forced to follow a circular path by using magnets, this

is called bending magnet radiation, which has a broad spectrum. The median of the radiated power is defined as the critical photon energy and is given by [9]

$$E_c = \hbar\omega_c \frac{3e\hbar B\gamma^2}{2m} \tag{1.11}$$

where E_c is the median energy of the emitted spectrum, e is the charge of the electron, B is the magnetic field of the bending magnet, m is the mass of the electron at rest and γ is the Lorenz factor. The Lorentz factor is given by [9]

$$\gamma \equiv 1/\sqrt{1 - v^2/c^2} \tag{1.12}$$

where v is the velocity of the electron and c is the speed of light.[9]

The angular pattern of the bending magnet radiation experiences a compression from the electron's frame of reference to the laboratory frame of reference due to the Lorenz transformation following [9]

$$\theta \simeq \frac{1}{2\gamma} \tag{1.13}$$

where θ is the angular pattern observed in the laboratory frame of reference, giving the emitted radiation a narrow cone shape and high brilliance.

Synchrotron Radiation from Undulators

Undulators consist of periodic structures of magnetic dipoles that stimulate forward-directed radiation with high intensity. In general, electrons traversing a periodic magnetic field (i.e., of the undulators) are forced to oscillate and emit radiation, greatly reduced in wavelength by a factor of $2\gamma^2$. The reduction in the wavelength can be explained in two steps. The first step is the Lorentz contraction. Because of relativistic effects, electrons traveling close to the speed of light will experience, in their frame of reference, a magnet structure with a contracted period, hence oscillate with a frequency according to the contracted period, given by:

$$\lambda_U' = \frac{\lambda_U}{\gamma} \tag{1.14}$$

where λ_U is the period of the undulator and λ_U' is the period of the Undulator in the electron's frame of reference. The oscillations will cause radiation of a frequency in the reference frame of the electron given by:

$$f' = \frac{c}{\lambda_U'} \tag{1.15}$$

The wavelength of the emitted radiation in the stationary laboratory frame of reference will be further reduced due to Doppler shift. The final on-axis wavelength will be proportional to λ_U/γ^2. At the BESSY II, the electrons reach a speed of about 99.99999% of the speed of light, corresponding to a Lorentz factor of $\gamma \sim 3327$. [17]

Frequency Selection in Undulators

The wavelength of the emitted radiation is controlled by changing the amplitude of the oscillation of the electrons. An increase in the amplitude decreases the mean forward velocity of the electrons. Consequently (and quite non-intuitively), a stronger magnetic field is used for stimulating the emission of lower energy photons, altered by changing the gap between the magnetic rails of the undulator. The energy of the photons is limited on the lower end by how far the magnetic rails can close. On the higher end the energy asymptotes to the energy of a non-deflected electron, correlated with a beam intensity that asymptotes to zero.

1.3.3. X-ray Free Electron Lasers

The X-ray free-electron lasers (XFELs) also use an undulator to generate radiation. The biggest difference of the XFELs is the higher electron energy of 7-17 GeV with a much longer undulator (>100 m at XFEL vs. ~1 m at Synchrotron) reducing the size and the divergence of the electron bunch and providing a much higher peak power, and shorter

pulses (see Figure 1.6). For instance, the average brilliance at the European XFEL reaches 10^{25} photons/(s.mm^2.mrad^2 0.1% bandwidth) roughly six orders of magnitude greater than the brilliance offered by the beamline used for the results obtained in this thesis (UE46-PGM2 at the BESSY II). A comparison of brilliance values is shown in Figure 1.7.

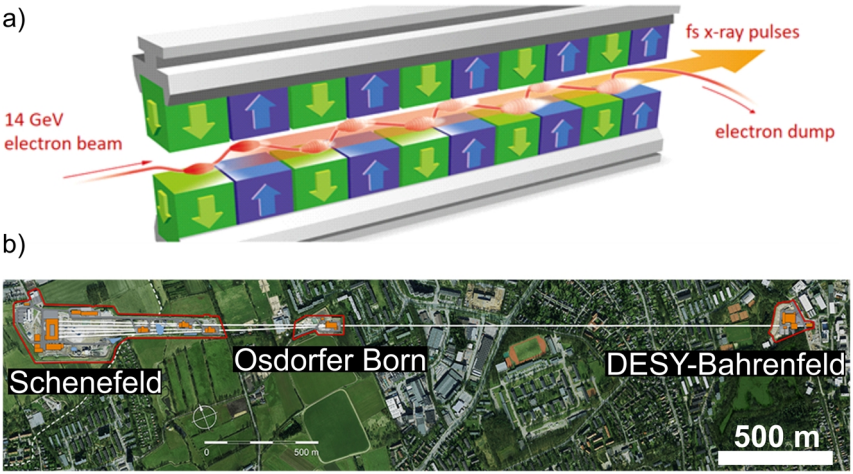

Figure 1.6 a) Working principle of an X-ray Free Electron laser: A high-relativistic electron beam(E ~ 7 – 17 GeV) passes an undulator-like structure and emits ultra-short X-ray flashes. Courtesy of European XFEL. b) Dimensions of the XFEL at DESY Hamburg. Courtesy of "European XFEL / Aerial photos: FHH, Landesbetrieb Geoinf. und Vermessung."

At the >100 meters long undulator used at the XFELs, the radiated fields are so strong that they affect the electron motion through Lorentz force causing a redistribution of the random electron positions into an orderly and strongly correlated electron wave such that the electron beam causes the radiated wave to interfere constructively. This effect is called self-amplified spontaneous emission (SASE).[18]

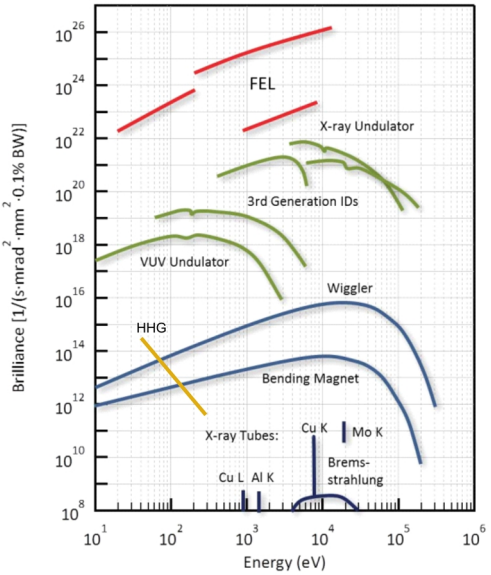

Figure 1.7 Average spectral brightness as a function of the photon energy of various X-ray sources. Adapted from Ref[19] with permission.

1.4. An Overview on X-ray Optics

1.4.1. Reflective Optics

Single Surface X-ray Mirrors

Single surface X-ray mirrors operate in total external reflection. The reflection angle changes by the angle of incidence and is wavelength-independent. This eliminates the need for refocusing the sample in X-ray microscopy for different energies. Owing to small angles required for total external reflection, ($\theta < \sqrt{2\delta}$) single surface X-ray mirrors need to be very long, depending on the material of the mirror. Using a high δ ma-

terial allows for shorter mirrors, nevertheless even the highly refractive Pt coated mirrors are about 100 mm long. In the optimum case, the single surface X-ray mirror should have an ellipsoidal and an atomically smooth surface. However, fabricating a large ellipsoidal surface with an atomically smooth surface finish is very challenging. As a consequence, a less challenging alternative, known as the Kirkpatrick-Baez mirror (KBM), is mostly used instead of the single ellipsoidal mirrors. The KBM system consists of two concave spherical mirrors with line focuses that are aligned perpendicular to each other to achieve a point focus (see Figure 1.8).[6] An active wavefront correction method enabled very high-resolution KBMs.[20] However, conventional KBMs usually have micron size focal spots. Furthermore, KBMs need to be aligned in 6 axes (X, Y, Z, pitch, yaw, roll) on two stages which are challenging.

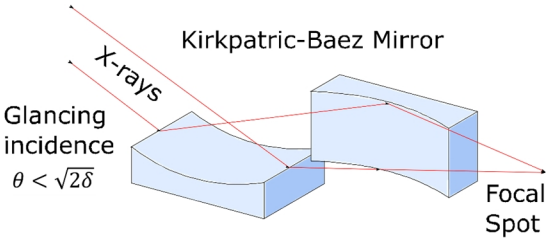

Figure 1.8 Schematic representation of the KBM system.

Multilayer Mirrors

Multilayer mirrors generally consist of alternating layers of low and high refractive index materials. Waves incident with an angle satisfying the Bragg condition (Eq. 1.7) will be strongly reflected from the multilayer interfaces. This angle can be much larger than that for total external reflection. Because the transmitted waves are bent due to refraction, the peak reflectivity occurs at an angle slightly larger than the Bragg angle.[21] For focusing, the multilayers should be curved.

1.4.2. Refractive Optics

Compound Refractive Lenses

Single refractive optics do not work efficiently in the soft X-ray regime because of low δ and significant β. As the X-ray energy increases, β decreases much more drastically compared to δ. The change of δ and β as a function of energy has been shown for two materials in Figure 1.3. The focal distance of a single refractive optic is given by

$$f = \frac{R}{2\delta} \tag{1.16}$$

where R is the radius of curvature. Owing to small δ in the hard X-ray regime, the focal length of single refractive optics is impractically long. For example, a single refractive optic made from Be with a radius of curvature of 100 μm has a focal length of about 59 m for 20 keV X-rays. To increase refraction and decrease the focal length, Snigirev *et al.*[22] proposed stacking multiple refractive lenses. These optics are called Compound refractive lenses. Their focal distances are given by

$$f = \frac{R}{N2\delta} \tag{1.17}$$

where N is the number of stacked lenses. There is a tradeoff in the number of stacked lenses and absorption. A material with a high δ/β ratio is generally preferred for compound refractive lenses.

1.4.3. Diffractive Optics

The Fresnel Zone Plate Lens

The invention of the FZP dates back to 1871[†‡], where Lord Rayleigh in his notebook wrote: "The experiment of blocking out the odd Huygens zones to increase the light at center succeeded very well".[23,24]

A monochromatic wave emerging from a point source *S* will have a spherical wavefront. Each point on the wavefront can be thought of a point source of spherical wavelets (Huygens Principle), where all the wavelets are in-phase. The wavefront can be imagined to constitute multiple numbers of annuli, in which every adjacent annulus has a distance that differs by $\lambda/2$ to a point *P* on the central axis. Consequently, each adjacent zone will tend to annihilate each other at point *P*. These annuli are called Fresnel zones.[§10] The idea of Fresnel zones is depicted in Figure 1.9. In an FZP, either odd or even Fresnel zones are blocked *via* a screen to avoid annihilation and achieve a substantial increase in the intensity at multiple points on the optical axis. The points where the intensity increases are called focusing orders.

The Fresnel zone radii for each zone can be calculated from Pythagorean Theorem

$$f^2 + r_n^2 = \left(f + \frac{n\lambda}{2}\right)^2 \tag{1.18}$$

thus,

$$r_n^2 = n\lambda f + \frac{n^2\lambda^2}{4} \tag{1.19}$$

[†] Lord Rayleigh never published this study. According to R. W. Wood, Physical Optics, 3rd ed. (Macmillan, New York, 1934), p. 37, Lord Rayleigh thought that his demonstration does not contribute anything new to the theory.

[‡] The first paper that includes the demonstration of an FZP was published by Soret in 1875.

[§] Lord Rayleigh alluded the annuli as "Huygens zones" in his notebook, however the term "Fresnel zones" is more commonly used.

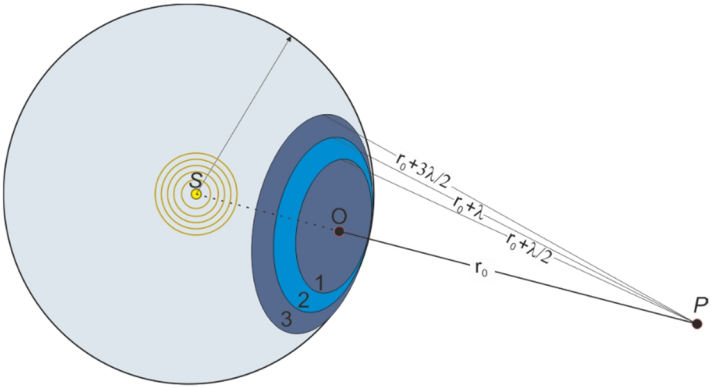

Figure 1.9 Propagation of a monochromatic wave from a point source S with a spherical wavefront. Three Fresnel zones are depicted. Going from the central axis to outer regions, each Fresnel zone is $\lambda/2$ further away to a point P on the central axis, hence annihilating each other due to destructive interference. The figure is adapted from Hecht.[10]

For $f \gg n\lambda/2$, which is mostly true for the X-ray range, the equation simplifies to

$$r_n \simeq \sqrt{n\lambda f} \tag{1.20}$$

The outermost zone width is an important parameter for calculating the spatial resolution and the focal length of the FZP, and is defined as,

$$\Delta_r = r_N - R_{N-1} \tag{1.21}$$

From Eq.(1.20) and Eq. (1.21) and after simplification, the focal length can be calculated by,

$$f \simeq \frac{D\,\Delta_r}{m\lambda} \tag{1.22}$$

where D is the diameter, and m is the diffraction order. The numerical aperture is then given by,

$$NA \simeq \frac{m\lambda}{2\Delta_r} \tag{1.23}$$

In a simple binary zone plate with equal odd and even zone areas, only odd-numbered focusing orders (also called diffraction orders) will satisfy the condition for constructive interference on the central axis. Theoretically, the number of focusing orders is infinite, but the diffraction efficiency will be substantially reduced for higher focusing orders. The diffraction efficiency of a zone plate is defined as the fraction of energy diffracted to each order to the incident energy. For a binary FZP with alternating opaque and transmissive zones (see Figure 1.10a) the diffraction efficiency for different diffraction orders is given by

$$\eta_m = \begin{cases} 0.25 & m = 0 \\ 1/m^2\pi^2 & m\ is\ odd \\ 0 & m\ is\ even \end{cases} \tag{1.24}$$

where "m" is the diffraction order. In the binary FZP design, 50 % of the incident radiation will be absorbed by the opaque zones. Zero diffraction order ($m = 0$) defines the non-diffracted radiation that is transmitted in the forward direction through the transmissive zones of the FZP. The zero-order constitutes 25 % of the radiation. About 10.1 % of the incident radiation will be diffracted to the 1st order ($m = 1$). An equal amount of about 10.1 % will be diffracted to the divergent (virtual) -1st order ($m = -1$). The rest of the radiation will be diffracted to higher odd diffraction orders in equal amounts for positive and negative orders. The 1st, 3rd, and 5th focusing orders are depicted in Figure 1.10a.

The angular distribution of the first order focal plane intensity of an FZP lens is given by,

$$I_1(\theta) = I_0\, N^2 \left|\frac{2J_1(ka\theta)}{ka\theta}\right|^2 \tag{1.25}$$

where $I_1(\theta)$ is the first-order intensity, I_0 is the illumination intensity, N is the number of zones, J_1 is a Bessel function of the first kind, order one, $k = 2\pi/\lambda$, $a = D/2$, $\theta = r/f$. The function $|2J_1(ka\theta)/ka\theta|^2$ is the Airy pattern function.[10] It has its first null at $ka\theta = 3.832$ so that

$$r_{null} = \frac{0.610\,\lambda}{NA} \tag{1.26}$$

which also corresponds to the spatial Rayleigh resolution of the FZP given by:

$$\delta_{Rayleigh} = \frac{0.610\,\lambda}{NA} \tag{1.27}$$

where δ is the point to point resolution according to the Rayleigh criterion. Combining equations Eq. (1.23) and Eq. (1.27), the resolution of an FZP can be directly correlated to the outermost zone width.

$$\delta_{Rayleigh} = \frac{1.22\,\Delta r}{m} \tag{1.28}$$

If the opaque Fresnel zones are replaced with transmissive phase-reversal ones, where the phase reversal zones induce a $\lambda/2$ phase shift relative to open zones, the electric field E in the focus will increase by up to two times. Because the intensity is proportional to E^2, the diffraction efficiency would increase by up to four times (up to 40 %). The required optical thickness of the phase-shifting zones can be calculated by,

$$\Delta t = \frac{\lambda}{2\delta} \tag{1.29}$$

The phase-reversal zones would absorb some of the radiation depending on the X-ray energy and material of the phase-reversal zones. This brilliant suggestion was made for the first time by Lord Rayleigh in his article on wave theory in 1888[25] and was demonstrated for the first time by R.W. Wood in 1898.[26] This specific type of FZP is

called as Rayleigh-Wood phase reversal zone plate. Figure 1.10b shows an illustration of the upper half part of a Rayleigh-Wood phase reversal zone plate.

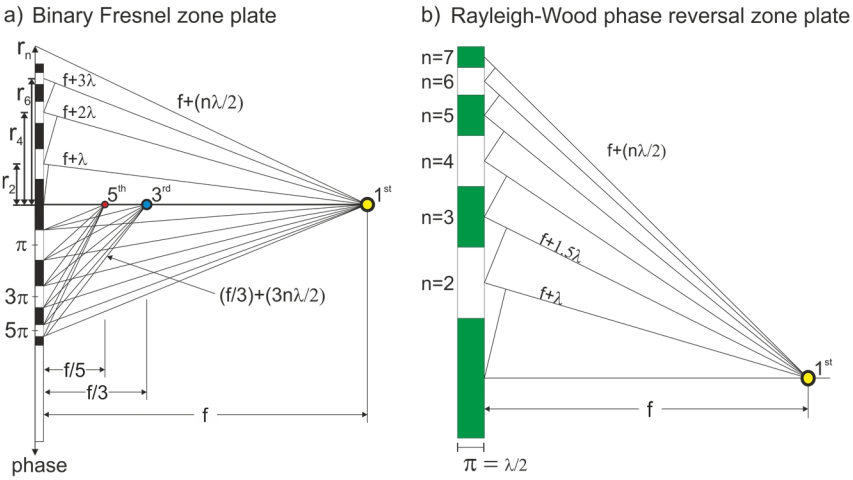

Figure 1.10 a) Sketch is showing a binary FZP from the side. Black (opaque) and white (transmissive) zones are shown. b) Sketch showing the upper half region of a Rayleigh-Wood phase-reversal zone plate from the side. Opaque zones are replaced by phase-reversal ones and contribute to the intensity at the focus. For simplicity, only the 1st order focus is depicted. Both zone plates are illuminated from the left side.

Kinoform Zone Plates

In the kinoform zone plates, there are no alternating transparent and opaque zones, but each zone constitutes a phase correcting profile so that the transmitted waves combine at the focus with a constant phase. Within adjacent zones, the phase leaps by 2π. Hence, one kinoform zone corresponds to two zones of an FZP.

The resolution and the focal distance of the kinoform zone plate can be calculated with the same equations for the FZP, considering each zone of the kinoform zone plate to correspond to two zones of an FZP. If the absorption is neglected, the theoretical diffraction efficiency of the kinoform lens is 100 %. A conceptual drawing of the kinoform zone plate is shown in Figure 1.11.

Figure 1.11 Sketch showing the side view of a kinoform type zone plate.

Multilayer Laue Lenses

Multilayer Laue lenses (MLL) are a linear version of FZPs and arose from the difficulty of fabricating FZPs with tilted zones. A single MLL has a line focus. Point focus can be obtained by stacking two MLLs that are crossed to each other, as shown in Figure 1.12. MLLs have even more stringent alignment requirements compared to KBMs owing to the chromatic nature. Very recently, 2D sub-10 nm resolution has been reported, reinforcing the potential of multilayer optics.[27]

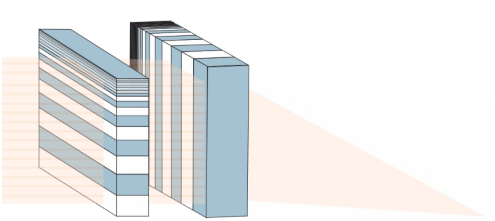

Figure 1.12. Illustration of crossed MLLs.

1.5. Diffraction Efficiency Estimation of FZPs

The diffraction behavior of FZPs can be categorized in three regimes, the Raman-Nath diffraction regime, the Bragg diffraction regime, and an intermediate regime in which both diffraction behaviors should be expected.[28]

As a rule of thumb, the diffraction behavior of low aspect ratio and low-resolution FZPs correspond to the Raman-Nath diffraction regime, whereas the diffraction behavior of very high aspect ratio and very high-resolution FZPs correspond to the Bragg diffraction regime. FZPs in the intermediate region having medium to very high-aspect ratios and resolutions show properties of both regimes.

The diffraction behavior of the multilayer FZPs (ML-FZPs) discussed in this thesis (see Chapter 4) fall in this complex intermediate regime where both diffraction behaviors play a role. The diffraction behavior Ion-beam lithography (IBL) (see Chapter 3) and 3D printed (see Chapter 5) zone plates developed for ptychographic imaging experiments are in the Raman-Nath regime. The boundaries of the Raman-Nath, Bragg and intermediate diffraction regimes have been discussed in depth by Maser and Schmahl.[28]

Historically, zone plates that behave in the Raman-Nath diffraction regime are named as optically thin. In this regime, the diffraction behavior depends on the profile of the zone plate, and is not affected by the angle of incidence hence the diffraction efficiency does not change by the tilt angle of the zones. As discussed previously, a phase zone plate in the Raman-Nath diffraction regime with rectangular zones (considering an ideal case with no absorption) can reach a theoretical diffraction efficiency of 40% in its 1st diffraction order, where the rest of the intensity is distributed to other diffraction orders.

1.5.1. Thin Grating Approximation

The diffraction efficiency of the optically-thin zone plates can be described with the planar diffraction theory. The equation for estimating the amplitude in the first order is for a general case is given by the Kirz formula,[29]

$$A_1 = \frac{C}{2\pi}\int_0^{2\pi} e^{-\eta\phi(\theta)} e^{i[(\theta-\phi(\theta)]} d\theta \tag{1.30}$$

where *C* is the incident amplitude, $\eta = \beta/\delta$, ϕ is the phase shift generated by the phase reversal zones ($\phi = 2\pi t\delta/\lambda$), and θ is the optical path length difference to the focal spot over one lens period.[30] The diffraction efficiency (DE) is then calculated by;

$$\mathrm{DE} = \mathrm{A}_1^2/\mathrm{C}^2 \times 100 \tag{1.31}$$

Before we apply the thin grating approximation (TGA) to phase reversal and kinoform zone plates let's first describe a general FZP with an arbitrary profile and an arbitrary phase shift as shown in Figure 1.13,

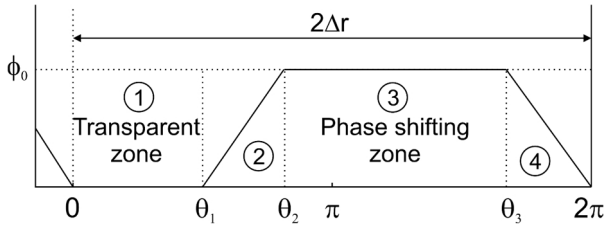

Figure 1.13 Description of the phase change and phase difference for an FZP period with an arbitrary profile.

where the local FZP period is divided into the following four regions:

$$\phi_0 = \begin{cases} 0, & 0 < \theta < \theta_1 \\ (\phi_0/\alpha)(\theta - \theta_1), & \theta_1 < \theta < \theta_2 \\ e^{-\eta\phi_0}, & \theta_2 < \theta < \theta_3 \\ (\phi_0/\alpha)(2\pi - \theta), & \theta_3 < \theta < 2\pi \end{cases} \tag{1.32}$$

region 1 is the transparent region, where the phase shift is zero. Region 3 is the phase-shifting region, with a phase shift of ϕ_0 and an amplitude attenuation of $e^{-\eta\phi_0}$. Regions 2 and 4 are the intermediate regions.

For $\theta_1 = \theta_2 = \pi$, $\theta_3 = 2\pi$, and $\phi_0 = \pi$ the rectangular FZP with a line to space ratio of 1 is defined. This configuration gives a binary FZP for $\eta = \infty$ and a perfect Rayleigh-Wood FZP for $\eta = 0$.

In the Raman-Nath regime, the diffraction efficiency of the FZP can be improved by manipulating the profile of the FZP to achieve a perfect phase-shifting within each zone. A special arrangement, where $\theta_1 = 0$, $\theta_2 = 2\pi$ and $\phi_0 = 2\pi$ is called the kinoform lens. For $\eta = 0$ a kinoform lens has a theoretical diffraction efficiency of 100 %.[28]

1.5.2. Coupled Wave Theory

When the aspect ratio of the FZP is to be increased, either for achieving higher resolution or for focusing higher-energy X-rays, the diffraction properties of the FZP can no longer be accurately estimated by the planar diffraction theory. Thus, the Kirz formula fails. Instead, coupled wave theory (CWT) has to be applied.[28]

The CWT has been applied by Koegelnik to volume gratings in 1969[31] and to high-aspect-ratio FZPs by Maser and Schmahl in 1992.[28]

The CWT gives a more general description of the interaction and propagation of the electrodynamic waves in materials. For solving arbitrarily shaped FZP profiles, Fourier expansion is used. CWT also allows calculating the performance of the FZPs with slanted zones, zone roughness, and for higher diffraction orders. The FZP simulation using CWT leads to a set of first-order differential equations, which cannot be solved analytically. One approach to solve the equations numerically is to use the Runge-Kutta algorithm.[28] In this thesis, an updated version of the CWT is applied which uses a matrix formalism instead of the Runge-Kutta algorithm. The matrix formalism is considered to be advantageous to Runge-Kutta because second-order derivatives and boundary diffraction may be included to deliver a rigorous coupled-wave analysis of the FZP.[32]

The system of first-order differential equations for the forward diffracted amplitudes $\boldsymbol{A}(z)$ can be written as matrices which include the X-ray optical parameters of the FZP material as well as the slanting angle and is given by [32]

$$\frac{d\boldsymbol{A}(z)}{dz} = \underline{\underline{\mathbf{M}}}\boldsymbol{A}(z) \tag{1.33}$$

where $\underline{\underline{\mathbf{M}}}$ is the complex general matrix. A new matrix $\underline{\mathbf{Q}}$ is defined for solving the equation, which consists of calculated eigenvectors of the matrix $\underline{\underline{\mathbf{M}}}$. The general solution is then given by:

$$\boldsymbol{A} = \underline{\mathbf{Q}}\,(\mathbf{C}\boldsymbol{e}^{\boldsymbol{x}}) \tag{1.34}$$

where $\mathbf{C}$ is the complex solution vector, x is the zone height, and $\underline{\underline{\mathbf{Q}}}$ is the complex eigenvector matrix of $\underline{\underline{\mathbf{M}}}$. The solution at $x = 0$ leads to a system of linear equations,

$$\boldsymbol{A}(x = 0) = \underline{\underline{\mathbf{Q}}}\,\mathbf{C} \tag{1.35}$$

where $\mathbf{C}$ denotes the unknown coefficients.

The diffraction behavior of the optically thick FZP is strongly dependent on the tilt angle of the zones and is affected very little by the grating shape.[28**] In Figure 1.14, the diffraction efficiency of one tilted and one non-tilted Al_2O_3-SiO_2 FZPs are calculated for 14.4 keV X-rays as a function of the outermost zone width, using the Kirz formula and the CWT. The theoretical diffraction efficiencies are calculated for the optimum FZP thickness for each outermost zone width.

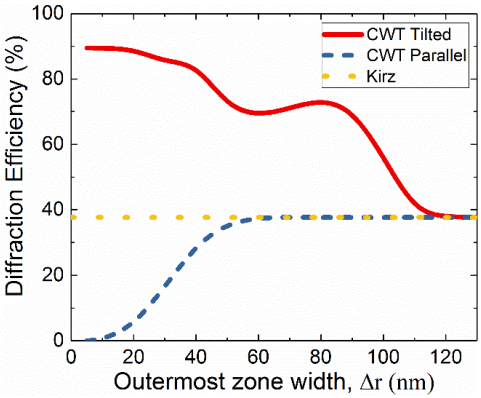

Figure 1.14 Calculated diffraction efficiencies of Al_2O_3-SiO_2 FZPs with tilted and parallel zones in the first diffraction order for 14.4 keV X-rays. The DEs are calculated using CWT and planar diffraction theory (Kirz). The CWT calculations are done locally for the outermost zone.

** The width of individual zones get smaller for outer zones according to the zone plate law. A zone plate can have zones that behave in the Raman-Nath diffraction regime close to the center and zones that behave in the Bragg diffraction regime at the outer zones.

The calculations show that tilting the zones of the FZP does not improve the DE for outermost zone widths greater than 120 nm, for the suggested materials and X-ray energy, a behavior expected in the Raman-Nath diffraction regime. The CWT calculations also show that DEs as high as ~90 % are achievable for very small outermost zone widths if the zones are tilted to the Bragg angle.

In the ideal circumstance, each Fresnel zone of the FZP should be tilted to its local Bragg angle. This results in zones that are wedged and therefore is sometimes named as wedged zone plates. The concept of flat, tilted, and wedged FZPs is illustrated in Figure 1.15

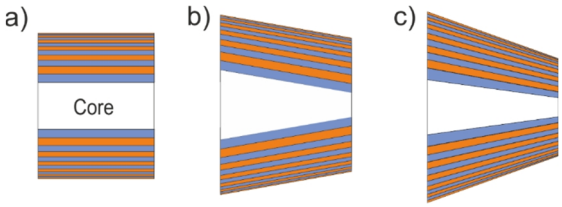

Figure 1.15 The concept of rectangular, tilted, and wedged zone plates are illustrated. Figure is partly published by Sanli *et al*.[33]

2. Overview of the Experimental Techniques

2.1. Atomic Layer Deposition

Atomic layer deposition (ALD) has emerged as an advanced thin-film growth technique providing excellent conformality and precise thickness control with applications ranging from microelectronics to solar cells.[34,35]

ALD thin film growth relies on alternating self-limiting surface reactions between a gas phase precursor and a solid surface. The growth is accomplished in two half-reactions, which are separated by an inert gas purging.[36] An ALD reaction cycle is depicted as an example deposition of Al_2O_3 in Figure 2.1.

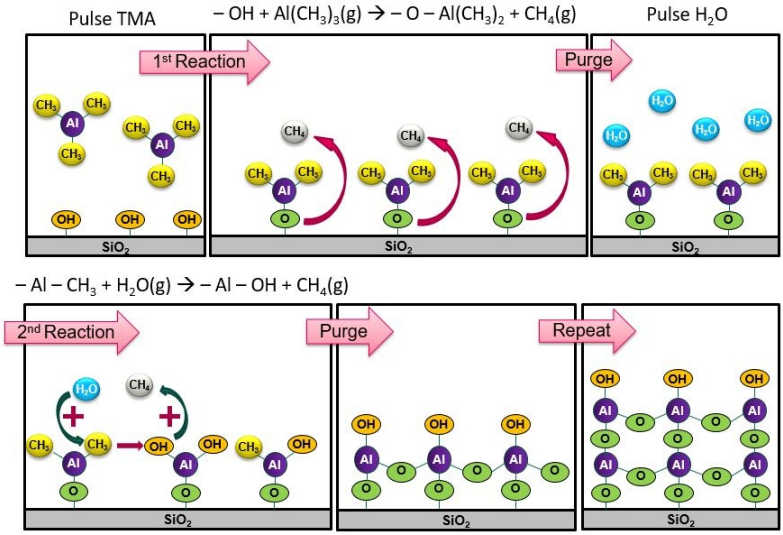

Figure 2.1 Schematic illustration of a typical ALD growth cycle to form Al_2O_3 using Trimethylaluminum (TMA) and H_2O precursors.

The reaction cycle starts with pulsing of the first gaseous precursor to the reaction chamber under vacuum, generally <1 Torr.[37] A waiting time (typically several 10's of

milliseconds up to a second depending on the material) is necessary to allow the precursor to chemisorb on the surface and reach chemical equilibrium. The excess precursor and reaction by-products are then purged using an inert gas. At this point, the first half-reaction is finished. Next, a second gaseous precursor is pulsed and purged similar to the first half-reaction to deposit the desired material with a thickness of up to one monolayer. The ALD cycle can be repeated multiple times to achieve the desired thickness.

For an ALD growth, the surface reactions should be self-limiting: after reaching a chemical equilibrium, the surface has to be saturated with the chemisorbed precursor. For an ideal ALD growth, the precursors should neither be physisorbed nor decomposed on the surface. Also, the desorption of the chemisorbed precursor should be negligible.[38]

These requirements set a temperature window for ALD growth. If the substrate temperature is too high, the first precursor may decompose on the surface before reacting with the second precursor, which will increase the growth per cycle (GPC). Another possibility is the desorption of the first precursor from the surface before the second precursor is pulsed. This will result in reduced GPC.

If the growth temperature is too low, the reactivity of the precursor may decrease, which will decrease the GPC. Alternately, in too low temperatures, an excess amount of precursor may condense on the surface, resulting in a high GPC. The concept of self-limiting growth, precursor condensation, precursor decomposition, and precursor desorption is illustrated in Figure 2.2. The self-limiting growth assures the GPC to be a certain and constant value.

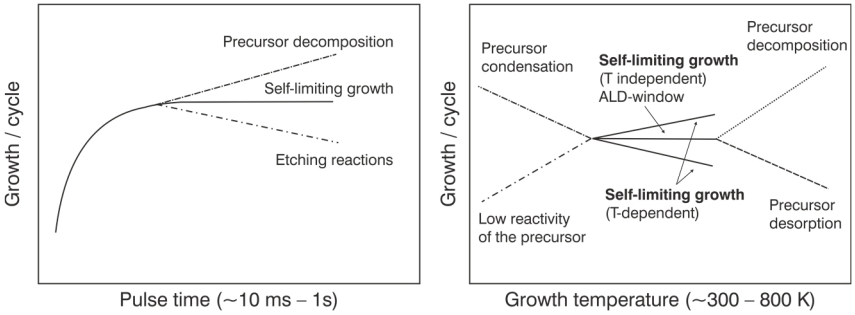

Figure 2.2 ALD growth concept is illustrated. Self-limiting growth can both be temperature dependent and independent. The ALD window is confined by precursor decomposition or desorption for high temperatures and by precursor condensation or low reactivity for low temperatures. Typical precursor pulse times are 10 ms to 1 s. Typical deposition temperatures are between 300 and 800 K. Adapted from Pinna N, Knez M: Atomic layer deposition of nanostructured materials. (p. XXIII, 2012). Copyright Wiley-VCH Verlag GmbH & Co. KGaA. Reproduced with permission.[39]

The thickness of the GPC is generally lower than one monolayer, owing to steric hindrance occurring between the ligands of the chemisorbed precursor.[40] Discussions about the growth mechanisms in ALD can be found in the literature.[38-40]

In the meanwhile, a wide range of materials can now be deposited by ALD. These materials include oxides, nitrides, sulfides, semiconductors as well as single-element metals or non-metals. Ternary compounds, quaternary compounds or compounds with an even higher number of elements can also be deposited using ALD. A non-exhaustive selection of single-elements as well as oxides, nitrides, and sulfides that have been deposited using ALD is shown in the periodic table (see Figure 2.3).

Compound thin film materials such as oxide ceramics can be grown through elementary exchange type reactions, where the metal precursor and the nonmetal precursor exchange their ligands. The success of ALD also depends on the availability of the precursor materials. For instance, for ceramic materials, suitable precursors are readily available making their deposition relatively easy compared to elemental metals. A straightforward route to deposit metal films is probably to implement a reduction reaction, for instance, using hydrogen. However, only a few metals such as Pt, Fe, Co, Ni,

and Cu can be deposited through a reduction reaction owing to the lack of precursors. Moreover, the growth rates for metals are much lower than for oxides, indicating that the chemistry is not as favorable. Plasma enhanced ALD is therefore often used for the deposition of metals.

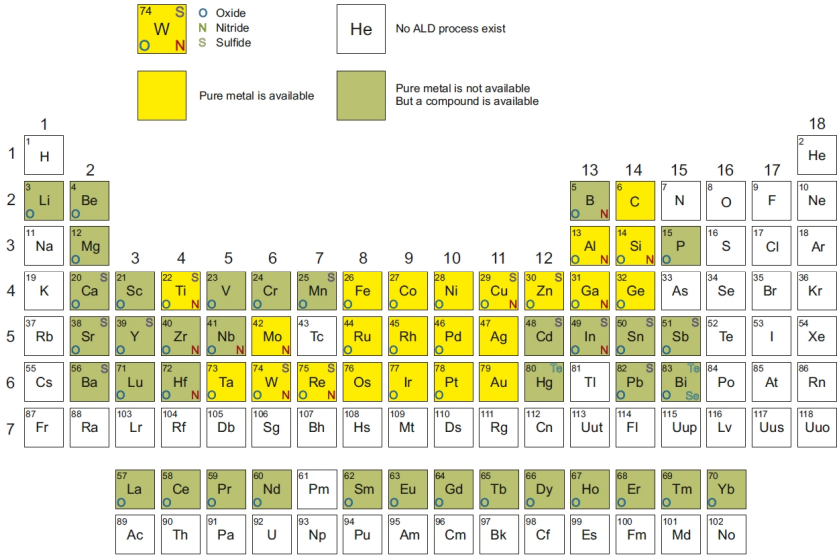

Figure 2.3 Materials available to ALD depicted on the periodic table. The list includes single elements, oxides, nitrides, and sulfides. (Based on references[37,40] however other materials such as Au are added).

Plasma ALD

From Figure 2.2, it is evident that the temperature constraint of ALD deposition puts stringent requirements on the selected precursors. Moreover, if a precursor is reactive at temperatures where it decomposes or desorbs, the ALD window disappears. For some materials, especially for many single-element films of metals and semiconductors, there exists no ALD temperature window.

One approach to overcome this limitation is to use free radicals, as one of the reactants. One of the simplest ways to create a free radical is through a glow discharge (plasma) in a low-pressure chamber.[41] The technique is known as plasma-enhanced ALD (PEALD) or radical-enhanced ALD (REALD). Different types of plasma reactor configurations and their implications are detailed in the literature.[39,41,42]

Besides realizing otherwise impossible thin films to be deposited by ALD, PEALD brings several other advantages. It has been reported that for some materials, PEALD has improved the thin-film density, reduced the impurity content, and resulted in better electronic properties at lower deposition temperatures.[39] Moreover, growth rates can be significantly improved using PEALD. The radicals are known to create a higher density of reactive surface sites improving the GPC.[39] PEALD also avoids the long H_2O purge times required for low-temperature thermal ALD processes.

The ALD Instrument

The ALD instruments consists of a heated vacuum reactor operating generally between 1 to 40 Pa with a heated sample stage, liquid precursors preserved in stainless steel heated bubblers, valves to insert precursors in the desired time and quantity, a plasma source for PEALD and finally gas lines to carry the precursor molecules and the plasma species into the chamber. An ALD reaction chamber is illustrated in Figure 2.4. In this thesis, a SENTECH ALD instrument was used. The details of the ALD system is given in Appendix D.

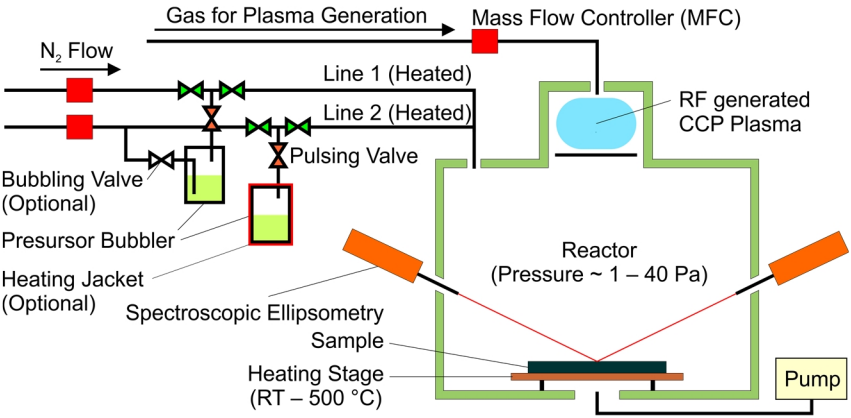

Figure 2.4 Illustration of the ALD reaction chamber. The precursors are stored in stainless steel precursor bubblers which can be heated to achieve the required vapor pressure. The time-controlled pulsing valves let a desired amount of precursor to reach the ALD lines, where the gas phase precursor is carried to the reaction chamber using N_2 gas flow. The reactor is kept under vacuum using a vacuum pump with typical process pressures between 1–40 Pa. The sample temperature can be adjusted between room temperature (RT) and 500 °C using the sample heating stage. Optical thickness measurements, which allow for precise thickness control, is done using spectroscopic ellipsometry.

2.2. Focused Ion Beam and Scanning Electron Microscopy

The focused ion beam (FIB) is a multi-purpose nanofabrication and characterization instrument. The technique was developed in the 1970s[43] and commercialized in the 1980s[44], and since then the FIB technology has advanced rapidly. The range of materials used in ion sources in the FIB instruments has also grown, improving the micromachining capabilities. In this thesis, the FIB is primarily used for sputtering and depositing platinum structures.

Interaction of Ions with Solids

Ions can interact with solids in numerous ways depending on the ion energy (see Figure 2.5).[45] These interactions can be used for thin-film deposition (see chapter 2.1), numerous analytical methods, sputtering as well as ion implantation.

In this chapter, the phenomena that occur at typical ion energies at FIB instruments will be discussed, which range from 5 keV to 150 keV.

The interaction of focused ion beams with solids are substantially different from electron beam—solid interactions. Electrons at the suggested energy range can transfer their energies only to other electrons located at the atomic shells or at the energy bands of the subject matter, whereas ions, being much heavier than electrons, can interact with the atomic nuclei and can easily reach the energy densities for breaking the bonds of the substrate material. This allows FIBs to be used for direct-write lithography or for slicing hard materials.

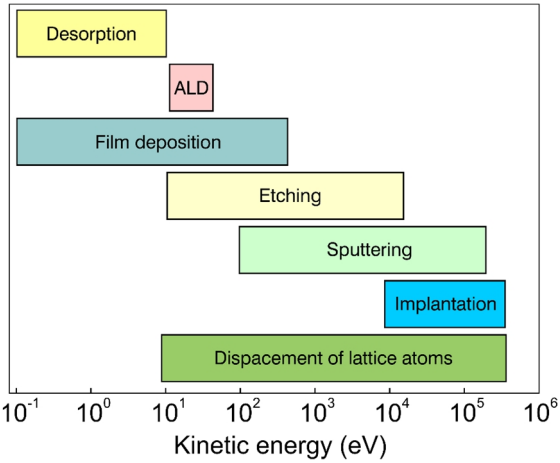

Figure 2.5 Ion matter interaction for different applications as a function of ion energy. Schematic is inspired from Takagi,[45] Pinna *et al.*,[39] Hellborg *et al.*,[46] and Jacobs.[47]

Possible interactions between a FIB and surface is depicted in Figure 2.6. When an incident high energetic ion strikes a solid, its kinetic energy is distributed over several atoms. These atoms will then strike other atoms creating a collision cascade. During this process, the incident ion slows down and comes to a rest when it loses all of its kinetic energy. The ion that is trapped in the material is called an implanted ion. The substrate atom that escapes the surface as a result of the collision cascade is called the sputtered

ion. The collision will also displace the atoms in the lattice from their original positions creating lattice defects such as vacancies and interstitials. Inelastic processes such as secondary electron emission also occur as a result of the ion-matter interaction.

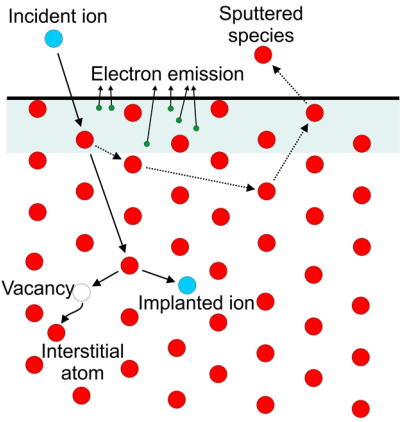

Figure 2.6 Illustration of the atomic displacement and the collision cascade that happens when a highly energetic ion penetrates a solid material. The red circles represent the lattice atoms.

Dual-beam Instruments

The dual-beam instrument combines the imaging capabilities of a scanning electron microscope (SEM) and the micromachining capabilities of the FIB instrument making the Dual-Beam device. The two complementary instruments together make an extremely capable imaging and micromachining tool. On the one hand, using the FIB column the sample can be structured, doped, sliced, deposited, etc., and on the other hand, the sample can be imaged using both the electron and ion beams. The former is a non-destructive imaging modality with a resolution down to a single nanometer, while the latter is destructive. However, imaging with ions also has its advantages, such as a strong channeling contrast.

With the addition of a gas injection system (GIS), the dual-beam offers enhanced etching, focused ion beam induced deposition (FIBID) and electron beam induced deposition (EBID). A micro manipulating needle can be used to transfer samples from the bulk to a sample holder.

Figure 2.7 shows a schematic drawing of a dual-beam instrument. In the SEM column, the electrons emitted from a field emission gun (FEG) are accelerated toward the anode with typical acceleration voltages between 0.5 to 30 kV. A well-defined electron probe of nanometer size is formed by the condenser and probe forming lenses. The probe is scanned in a raster pattern across the sample using the deflection coils. The electron-beam matter interaction generates X-rays, Auger electrons, backscattered and secondary electrons which are collected by various detectors to construct an electron microscopy image.[48]

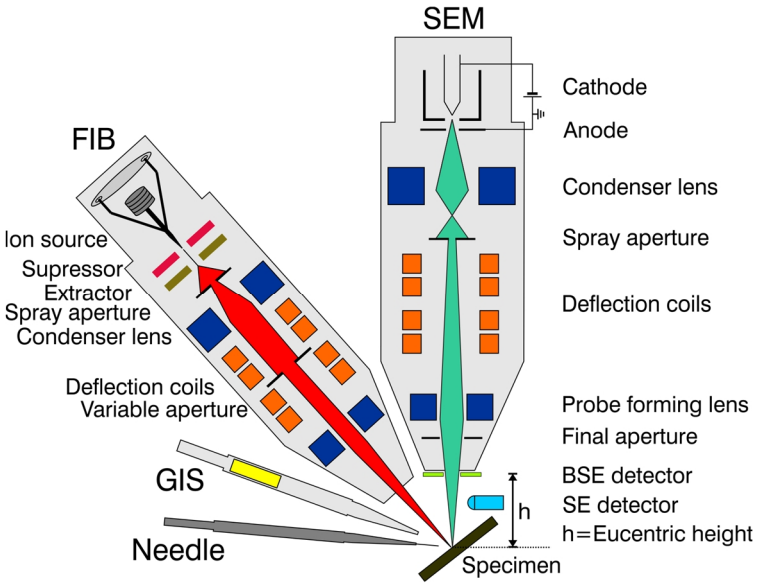

Figure 2.7 Schematic representation of a typical dual-beam instrument. The ion column rotated 52° with respect to the optical axis of the electron column.

In most modern FIB column, the ion beam is generated using a liquid metal ion source (LMIS). The most common metal used in LMIS is gallium, owing to its low melting temperature (29.8°C), low vapor pressure, efficient ionization and sufficiently high atomic number required for effective sputtering. The ion beam is generated using a strong electric field. The electric field causes the liquid film to protrude from the tip of the needle, forming a very sharp tip known as a Taylor cone. Ionization and field emission of the gallium atoms happens when the electric field at the tip reaches about 10^{10} V/m.[49] Typical ion beam currents in Ga^+ FIBs are between 1 pA and 65 nA, which is defined by the variable aperture. The beam current sets a trade-off between a well-defined high-resolution beam for delicate micromachining or imaging with less damage and a strong low-resolution beam for rough milling applications.

Other ion beam sources such as Xe^+ Plasma (electron cyclotron resonance source) or He^+ (gas field ionization source) ion beams can be used for much higher beam currents or much higher resolutions respectively.

Focused Ion Beam Induced Deposition (FIBID)

The FIB can be used to deposit materials onto almost any surface using a chemical vapor deposition like method, which is known as focused ion beam induced deposition (FIBID).

FIBID method uses a volatile metal compound as the precursor, which is decomposed to nonvolatile species upon interacting with the FIB and adsorbed on the surface. The materials that can be deposited by FIBID is limited to the availability of the precursors with the desired properties such as having a high enough sticking probability at room temperature as the FIB sample stage is not heated, and upon interaction with the FIB, the precursor must decompose before it is sputtered away.

In this thesis, FIBID of Pt was used for making a beamstop on IBL- and ML-FZPs (see Chapters 3 and 4) and for preparing TEM lamellas (see Appendix F). The organometallic compound (methylcyclopentadienyl)trimethyl platinum was used as the precursor for Pt deposition.

The FIB parameters have to be selected carefully for a successful FIBID. There are many parameters that affect the quality and speed of the FIBID. Some of these parameters are the beam current, scan area, pixel dwell time, beam overlap, GIS needle distance to the sample surface, GIS needle diameter, and the crucible temperature. For instance, the pixel-dwell-time must be low to avoid any sputtering after the precursor is adsorbed on the surface but must be long enough to decompose enough precursor to enable a practically fast deposition. The purity of the deposition also depends on the pixel dwell time. Another parameter is the beam current. Likewise, too-large beam current sputters, and too low beam current is inefficient. The optimum beam current is experimentally found to be between 2–6 pA/µm^2, as shown in the technical note given by the Thermo Fischer Company (see Figure 2.8).

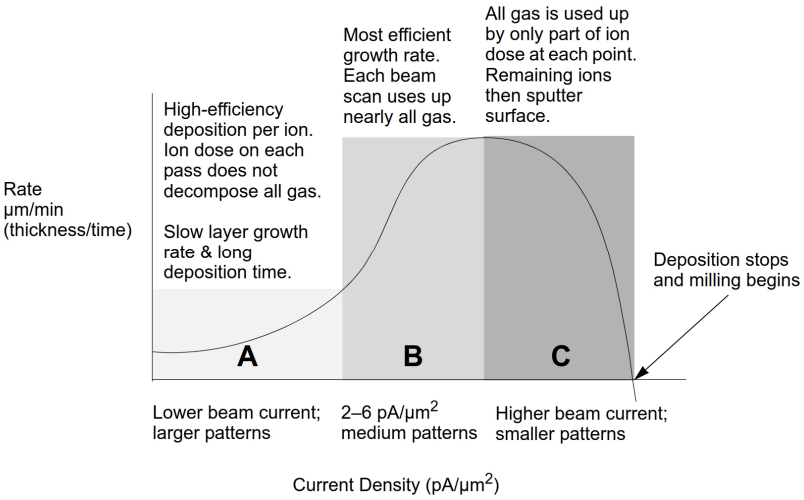

Figure 2.8 FIBID Pt deposition rate as a function of current density. The figure is taken from platinum deposition technical note with permission. Courtesy of Thermo Fischer Scientific Incorporation.

2.3. Two-Photon Polymerization

Two-photon polymerization (2PP) boosted the precision and the resolution of 3D printing to a level, where it can now be applied to realize some of the most demanding functional geometries required by nanotechnology, with feature sizes down to about 20 nm.[50] The additive manufacturing process that utilizes 2PP is called 3D direct laser writing (DLW), which is also known as 3D laser lithography or 3D microprinting.

The experimental set-up used in this work[††] is as follows: A femtosecond pulsed, infrared (IR) laser beam is focused by using a high numerical aperture objective of 63x into a liquid mixture of monomeric matrix molecules and photo-initiators (see Figure 2.9a and b). Single IR photons do not have the necessary energy to excite the electrons. However, a simultaneous absorption of two-photons doubles the energy and is enough to bring the molecule to an excited state (see Figure 2.9b). The two-photon absorption is a non-linear event, where the probability depends on the square of the incident photon flux. As the intensity of the laser beam is highest in the center of the focal beam and decreases roughly by the square of the distance, the two-photon absorption rate decreases roughly with the fourth power of the distance from the focal spot. Hence, two-photon absorption in the regions other than the focal spot is negligible.

The two-photon absorption triggers photochemical cross-linking of the photoresist, leading to polymerization, and solid formation. The photopolymerization reaction is inhibited by the presence of oxygen, which is found in the photoresist or in the ambient. Therefore, enough number of initiating radicals should be generated for solid formation before the reaction is impeded. The non-linearity of the two-photon absorption together with the number of necessarily excited molecules establishes an intensity threshold for polymerization (see Figure 2.9c). The polymerization threshold causes the interaction volume (voxel) of the laser beam to be smaller than the wavelength of the IR photons, allowing sub-wavelength structures to be written.

[††] In this work Nanoscribe Photonic Professional GT2 instrument was used which belongs to the Physical Intelligence Department of the Max Planck Institute for Intelligent Systems.

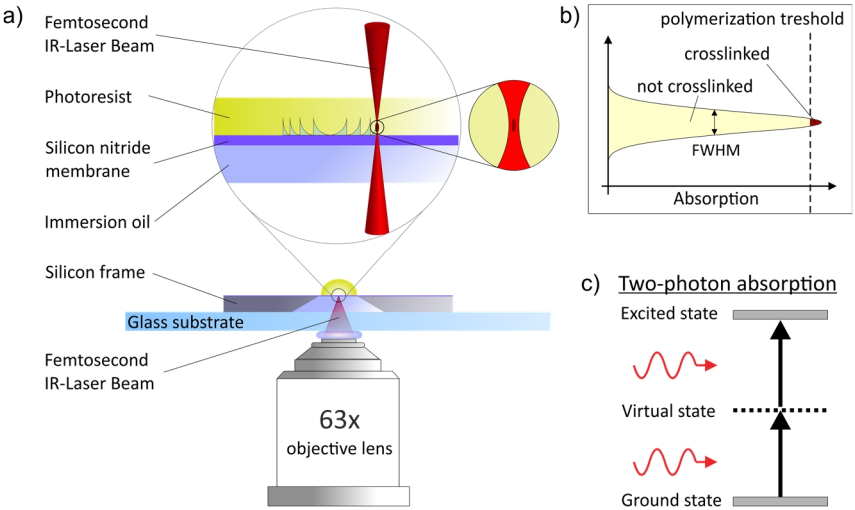

Figure 2.9 Overview of the experimental set-up for 2PP direct-laser writing. a) Schematic representation of 3D nano-printing set-up for the fabrication of plastic X-ray lenses on X-ray transparent Si_3N_4 support membranes. A femtosecond pulsed laser beam is focused by a 63x objective lens through a glass substrate, immersion oil, and Si_3N_4 membrane and scanned in the photoresist. b) Schematic representation of the sub-wavelength voxel size due to the threshold principle. The polymerization reaction is triggered only when the laser intensity reaches a certain threshold, known as the polymerization threshold. This allows features smaller than the FWHM of the focal spot to be printed. c) Schematic representation of two-photon absorption. Simultaneous absorption of two photons can excite the molecules. The figure was partly published by Sanli *et al*.[30]

2.4. Scanning Transmission X-ray Microscopy

A scanning transmission X-ray microscopy (STXM) beamline with elliptical undulator of the APPLE II type (UE46-PGM2) located at BESSY II (a 3rd generation synchrotron source) and named as MAXYMUS was utilized for the synchrotron experiments. The MAXYMUS beamline is operated by the Department of Modern Magnetic Systems of the Max Planck Institute for Intelligent Systems. However, experimental time at the synchrotron (named as beamtime) is allocated by an external committee, which requires a written application with the proposed experiments at least 6 months in advance. MAXYMUS is a unique tool for time-resolved studies and is heavily overloaded. Owing to the high

demand ptychography experiments is a side project at the MAXYMUS. The details about MAXYMUS can be found in Ref[19].

The key components of the MAXYMUS are illustrated in Figure 2.10. The soft X-rays are generated using an undulator and monochromatized by a grating monochromator with an energy resolution of $\Delta E/E \sim 10^{-4}$. The energy is selected by a double-slit arrangement, which defines the illumination of the optical focusing length located about 3 m downstream.

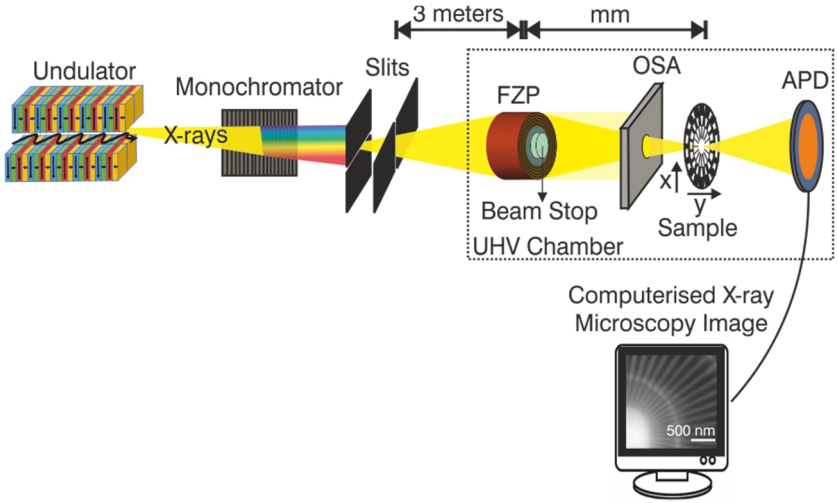

Figure 2.10 Schematic diagram of the STXM MAXYMUS. X-rays are created at the undulator. A monochromator and two slits are used to have both monochromatic and coherent X-rays. An FZP is used to focus X-rays onto the sample, which is raster scanned in two dimensions. A beamstop and an order-selecting aperture (OSA) inhibits non-diffracted (zero-order), and high-order diffracted radiation from reaching the sample. The transmitted light is transformed into an electronic signal by an avalanche photodiode (APD). An image is constructed in the computer electronically, corresponding to a 2D map of sample absorption.

A plane grating monochromator and a spatial filter are used to monochromatize the beam. The spatial filtering is necessary because the light emitted from the monochromator is spatially energy-dispersive. Its size selection creates a trade-off between monochromacity and photon flux. A smaller slit also improves coherence, which is

needed for high-resolution microscopy.[19] The flux is generally significantly lowered by the use of the spatial filter. One reason for the need for a highly brilliant synchrotron source is this great reduction of photon flux necessary to obtain highly coherent and monochromatic light. The coherent and monochromatic X-rays are then focused onto the sample of interest using an FZP. Zero and higher-order radiation are eliminated using a beamstop and an order selecting aperture (OSA). The total transmitted light is detected and transformed into an electronic signal using a point detector, which is in the present set-up an avalanche photodiode (APD) as the sample is raster scanned in two dimensions. The amount of transmitted light at each scanning position is directly correlated to the absorption of the sample at that position. This gives localized absorption as a function of sample position. Using this information, a computerized absorption contrast image can be created.

Photon Flux at the MAXYMUS

The MAXYMUS beamline is designed for operation at the soft X-ray regime; hence, the photon flux reduces significantly for higher photon energies, as shown in Figure 2.11.

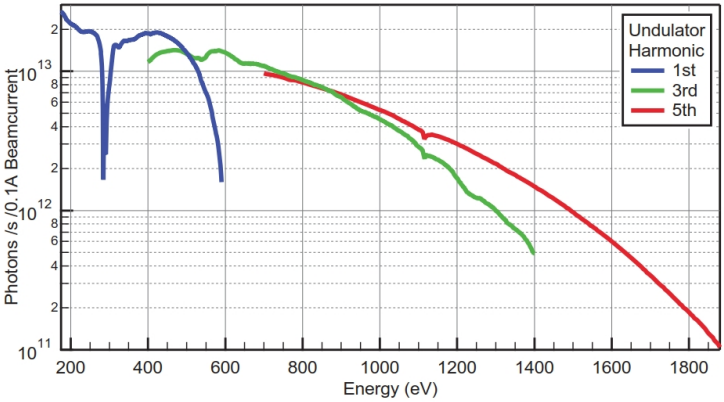

Figure 2.11 Photon flux at the UE46-PGM2 beamline of MAXYMUS for a 90 µm wide exit slit. The intensity for the 5th undulator harmonics decreases by a factor 400 for increasing the energy from 800 eV to 1800 eV. The figure is taken from Ref.[19] with permission.

Resolution Test Samples

Two commercially available certified test samples, the Siemens Star (SS) test sample (Carl Zeiss AG, Germany) and the BAM-L200 (Bundesanstalt für Materialforschung und prüfung) test sample were mainly used in testing the performance of the FZPs.

SS's features are made out of 180 nm thick Au features, therefore gives a high absorption contrast. The inner-most features and space between adjacent features are roughly 30 nm in width. However, due to nanofabrication related imperfections, some features are smaller and some are larger than intended. In the SS imaging results, several dark gray regions can be seen which looks like image artifacts. These regions are covered (unwillingly) with carbon due to extended imaging experiments and testing. The regions where carbon is present absorb some portion of the incident X-rays, hence appear darker in the absorption images. The effect of carbon presence is also present in the phase-contrast images. An SEM image of the SS test sample is shown in Figure 2.12.

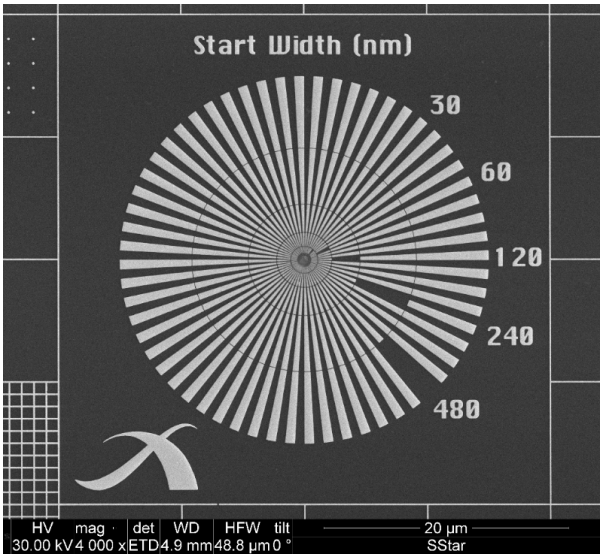

Figure 2.12 SEM Image of the Siemens Star test sample

The BAM-L200 test sample is made up of GaAs/$Al_{0.7}Ga_{0.3}As$ multilayers. The X-ray absorption contrast of the BAM-L200 is not as good as the SS test sample. Therefore, it is generally used when the targeted resolution is smaller than the feature size of the SS test sample. The specifications of the BAM-L200 test sample can be found in the literature.[51] SEM images of the BAM-L200 sample is shown in Figure 2.13.

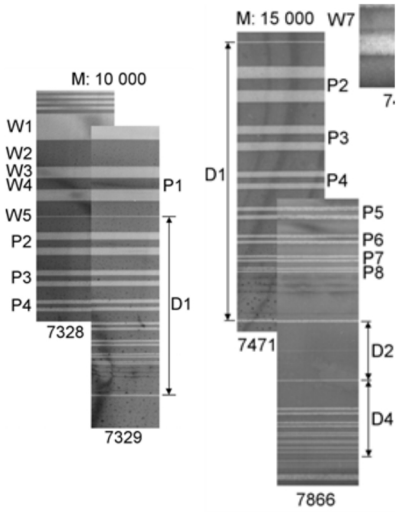

Figure 2.13 SEM images showing the BAM-L200 test sample. The regions denoted by D1 and D4 are particularly important because these regions have been imaged with X-rays in this thesis. The figure was taken from BAM Certification File. Courtesy of M. Senoner.

2.5. Ptychography

X-ray ptychography is a microscopy technique that offers superior resolution compared to conventional STXM at the expense of solving the challenging phase problem which requires advanced algorithms and state-of-the-art hardware for computation.

In ptychography, the sample is scanned using a coherent X-ray beam with overlapping illumination positions, and the far-field diffraction pattern is detected for each illumination position. It is assumed that the scattered wavefield reaching the Charge-

coupled device (CCD) is the Fourier transform of the samples transmission function, which necessitates the sample plane illumination to be coherent. The basic idea is to reconstruct the sample by an inverse Fourier transform of the detected diffraction pattern. As the incident light will be diffracted from feature sizes as small as its wavelength, the reconstructed image resolution is ultimately limited by the wavelength.

Since the CCD only detects the intensity of the wavefield, the phase information is lost during detection, which is known as the phase problem.

In ptychography, the overlap in the scanned regions provide over-determination of information in the detected diffraction pattern and allows the use of iterative reconstruction algorithms to solve the phase problem and reconstruct the amplitude and phase of the object as well as to retrieve the illumination function.[52] An elementary experimental scheme is depicted in Figure 2.14.

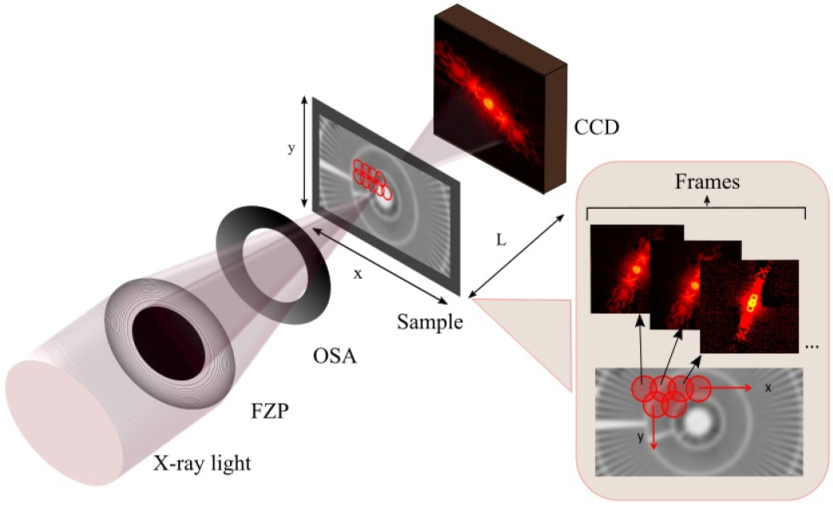

Figure 2.14 Schematic representation of the experimental set-up for ptychography. The X-rays are focused onto the sample of interest. The sample is raster-scanned with a scan step smaller than the full width at half maximum (FWHM) of the focal spot allowing for a sequence of diffraction images to be detected from overlapping regions to create data redundancy, which helps a fast convergence of the reconstruction algorithm. Image courtesy of Iuliia Bykova.[53]

Iterative Reconstruction Algorithm

In this thesis, the SHARP (Scalable Heterogeneous Adaptive Real-time Ptychography) software developed initially for the Advanced Light Source was used for the ptychographic reconstructions, which is based on an iterative phase retrieval algorithm.[54]

An example of the ePIE iterative reconstruction algorithm is shown in Figure 2.15. The reconstruction algorithm starts with an initial guess of the illumination function, $P_j(r)$, and the object function, $O_j(r)$. The exit wave is then determined by the multiplication of the initial guess of the object function multiplied by the illumination function:

$$\Phi_j(\mathrm{r}, R_{n(j)}) = O_j(\mathrm{r}) P_j(\mathrm{r} - R_{n(j)}) \tag{2.1}$$

The Fourier transform of this multiplication gives a phase and amplitude value in the reciprocal space.

$$\Phi_j(\mathrm{k}, R_{n(j)}) = FT\left[\Phi_j(r, R_{n(j)})\right] = A_j(\mathrm{k}, R_{n(j)}) e^{i\alpha_j(\mathrm{k}, R_{n(j)})} \tag{2.2}$$

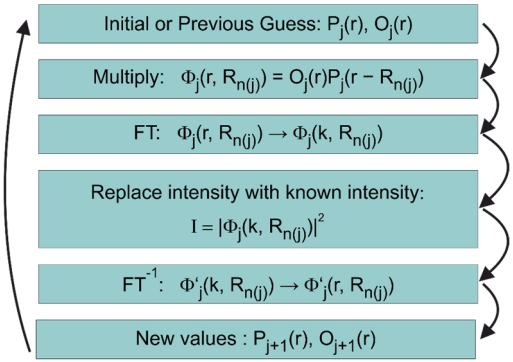

Figure 2.15 Flowchart of ePIE iterative reconstruction algorithm.

Because the intensity of the far-field diffraction pattern is known, the reconstructed intensity is replaced with the known intensity. An inverse Fourier transform allows reconstructing a new exit wave in the real space that is better than the previous

guess. The algorithm is iterated enough times until the error between the reconstructed exit wave and estimated exit wave is small enough or converges to a value.

Although in principle, the resolution in ptychography is limited by the wavelength of the incident X-rays and the angle of the scattered light that is detected by the camera (camera detector size and distance), one obstacle impeding atomic resolution is the low intensity of the high-angle scattered light coming from small features. For instance, it has been theoretically calculated that for resolving single carbon atoms a dose density of at least 9 x 10^{10} photons/nm^2 would be required.[55] Hence, the resolution in ptychography is theoretically limited by the incident coherent photon intensity, I_c on the sample which is given by:[56]

$$I_c = \frac{F_c}{A_{eff}} \propto Br \frac{\Delta E}{E} NA^2 DE \tag{2.3}$$

where F_c is the coherent flux, A_{eff} is the effective area of the focus, Br is the brilliance of the source, $\Delta E/E$ is the energy bandwidth, NA is the numerical aperture of the optic, and DE is the diffraction efficiency of the optic.

Besides the dose requirements, the dynamic range and the physical size of the CCD, the accuracy of the scanning stages, the success of the reconstruction algorithm, the reconstructed pixel size and the scan parameters such as the sample overlap also limits the achieved resolution.

Reconstructed Pixel size

Considering a perfect illumination, the resolution at the MAXYMUS is limited by the pixel size of the ptychographic reconstruction, which is given by:

$$\Delta x = \frac{\lambda \cdot L}{N \cdot p} \tag{2.4}$$

where λ is the wavelength, L is the distance between the sample and the CCD, N is the number of pixels on the CCD in one direction which is 264, and p is the physical

pixel size, which is 48 µm. The details about the CCD is given in Appendix C. Only λ and L are free variables. The effective pixel size Δx as a function of photon energy for $L = 4\ cm$ and $L = 8\ cm$ is calculated and shown in Figure 2.16. The smallest reconstructed pixel size is achieved when the CCD is at its closest position to the sample and at the high energy end. Choosing higher energies for achieving smaller effective pixel sizes may seem like a straightforward choice, however, in real-life scenarios the wavelength λ is most of the time not a free variable because of the discrete energies of absorption edges. Two frequently used energies; the Fe L-edge and O K-edge are labeled in the figure to emphasize the wavelength pixel size relationship of ptychographic reconstruction.

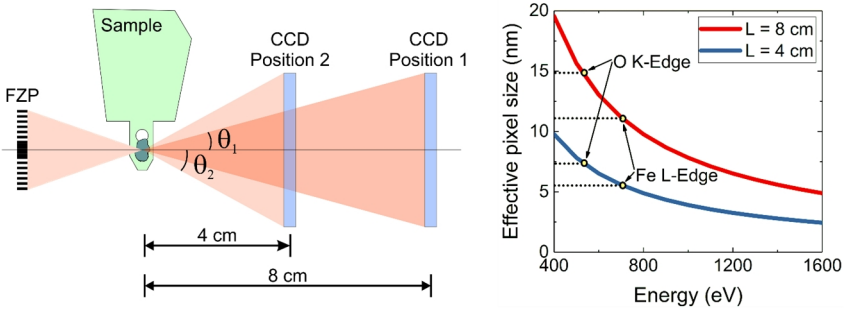

Figure 2.16 Effective pixel size as a function of photon energy for two different CCD-Sample distances. O K- and Fe –L edges are marked to emphasize energy constraint of ptychographic reconstruction.

At the MAXYMUS, the closest distance we can get the camera to the sample is 8 cm owing to the physical size of the components as shown in Figure 2.17.

For reducing the effective pixel size, in some experiments, the piezo stage (labeled in Figure 2.17) is removed, and the CCD – sample distance can be reduced down to 4 cm. As the sample-piezo scanning stages are removed, this high-resolution set-up requires the FZP stage to be raster scanned while the sample is stationary. A record 5 nm resolution will be shown in Chapter 3 using the high-resolution mode.

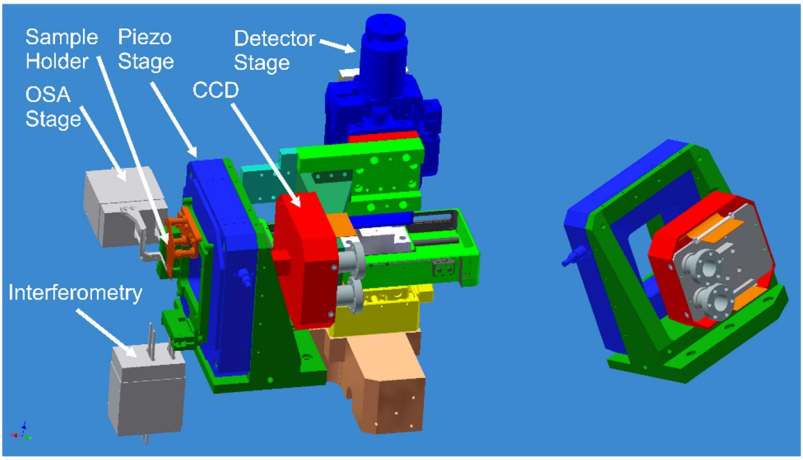

Figure 2.17 Schematic representation of MAXYMUS experimental set-up arranged for ptychography experiments. The CCD — sample distance is limited by the physical dimensions of the experimental components. The image on the right shows the CCD is larger than the middle opening of the Piezo stage, hindering the CCD to come closer to the sample. The drawing is courtesy of Christian Wolter.

FZP Design for Ptychography

As discussed above a high coherent flux is a necessity for high-performance ptychographic reconstruction. The focusing optic has to be illuminated coherently to achieve a coherent focal spot illumination. FZPs with larger diameter require an incident beam with a greater coherence length, which can be achieved by reducing the opening between the spatial filtering slits shown in Figure 2.10. The dependence of coherence length and the degree of coherence on slit size is depicted in Figure 2.18.

Due to increased diffraction effects from small slits, the intensity decreases nonlinearly for smaller slit sizes. Therefore, the FZP with the largest diameter will not give the highest coherent light intensity. The perfect ptychographic FZP for the MAXYMUS beamline is therefore not the one with the largest diameter.

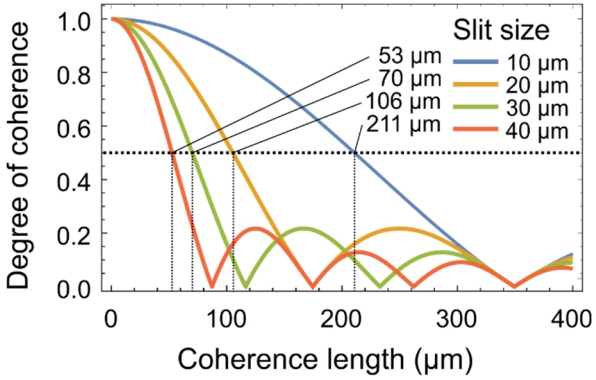

Figure 2.18 The dependence of coherence length and the degree of coherence on slit size calculated for 1000 eV photon energy.

Eq.(2.3) indicates that the theoretical dose limited resolution would increase as the outermost zone width of the FZP gets smaller. Although this is theoretically correct, it is of little practical importance due to several reasons. First, the image resolution after ptychographic reconstruction is, most of the time, not dose limited. The need for higher resolution FZPs for ptychography would only arise for targeting subatomic resolutions, which is currently out of the scope of the MAXYMUS beamline.

Second, as the focal spot size gets smaller, the number of scanning points have to increase to image the same field of view, increasing the computation time required for the reconstruction. Indeed, considering a ptychographic image of the same field of view, the intensity loss arising from using a low numerical aperture optic can be compensated by increasing the scanning time of each point. Therefore, an increase in the resolution by using a smaller focal spot can be achieved in the expense of reducing the field of view.[57] Moreover, the maximum number of scanning points at the MAXYMUS is 170 X 170 in x- and y- directions limited by the GPU memory (8x12 GB). For instance, using a high-resolution FZP with an 18 nm outermost zone width and a FWHM focal spot size of 18.5 nm (θ_{FWHM} = 1.028 λ / D) would give a maximum field-of-view of 943.5 x 943.5 nm^2 for a typical overlap value of 70 %.

When deciding on the diameter of the FZP, the outermost zone width and the resulting focal distance should be considered simultaneously. The size of the vacuum chamber and the size of the components inside the chamber such as the motorized stages or the CCD camera as well as their degree of freedom limits the allowable focal distance. Two other aspects are the depth of focus, which decreases quadratically by increasing the NA of the lens and significantly lower diffraction efficiencies achieved by high-resolution FZPs.

3. IBL-FZPs for Pychography and Direct Imaging

The following persons contributed to the work presented in this chapter: The coupled-wave theory simulations were done using a software provided by Prof. Dr. Gerd Schneider. The MATLAB codes for thin grating approximation used in diffraction efficiency simulations was developed by Dr. Nicolas Teeny and Dr. Kahraman Keskinbora. The MATLAB code for generating GDSII files was provided by Dr. Kahraman Keskinbora. The direct laser written (DLW) beamstop is fabricated by Robert Sittig. Robert Sittig was co-supervised by Umut T. Sanli and Margarita Baluktsian.

3.1. Introduction

X-ray imaging using ptychography has developed rapidly in recent years with extremely attractive resolutions limited in theory only by the wavelength. As described in Chapter 2, the required sample illumination spot size is much larger, with an optimum of about 100 nm. Since the resolution of ptychography also depends on the registration of the weak speckles at high angles, which generally have very weak intensities, the diffraction efficiency of the focusing optic is the most important parameter. A new ptychographic set-up has been realized at the beamline UE46-PGM2, MAXYMUS located at the BESSY II, Berlin for coherent imaging and spectroscopy experiments.

The purpose of the presented work was to support ptychographic coherent diffractive imaging experiments at the MAXYMUS beamline by developing high-performance FZPs in a fast and reliable manner adjusted for the evolving needs of the beamline and the beamline scientists.

A spot size in the order of 75 to 200 nm is optimum for maximizing imaging throughput, as a strong overlap between neighboring pixels is an ultimate necessity for ptychography. Therefore, FZPs having a Δr = 75–120 nm with diameters adjusted for the coherence requirements and conditions of the beamline were fabricated. It was possi-

ble to achieve this, using a relatively out of date, in-house Ga^+ focused ion beam instrument. The design of the IBL-FZPs, such as the outermost zone width, the diameter, the beamstop size or the focal length are decided based on the requirements of the MAXYMUS beamline, considering the limitations and requirements of the MAXYMUS microscopy set-up.

Five IBL-FZPs (IBL-P1 to IBL-P5) have been prepared in 3 generations, particularly for realizing/advancing ptychography experiments. In addition, an IBL-FZP (IBL-D1) with a relatively small 50 nm outermost zone width was also developed for supporting direct imaging experiments.

3.2. Preparation Route of IBL-FZPs

IBL-FZPs are fabricated on commercially available Si_3N_4 membrane windows with a membrane thicknesses of 50 or 100 nm (Silson Ltd., United Kingdom) (see Figure 3.1a). Thin Si_3N_4 membrane windows have the necessary transparency in the X-ray regime (100 nm Si_3N_4 transmits 92.5 % of 1000 eV X-rays). If the FZP is going to be used in even lower energies, using a 50 nm thick membrane instead of a 100 nm would have significance. For instance, for 500 eV X-rays, transparency of Si_3N_4 is 62.4 % for 100 nm thickness and 79.0% for 50 nm.

The fabrication is done in several steps. In the first step, a Au thin film of thickness generally between 100 to 500 nm is deposited using magnetron sputtering (see Figure 3.1b). Au is chosen due to its high mass density and high refraction in the X-ray regime, minimizing the required optical thickness, and relaxing some of the nano-fabrication challenges. Furthermore, Au has one of the highest Ga^+ sputter yield[‡‡] and an excellent chemical stability.

In the second step, the zone positions are simulated using the zone plate law according to the desired FZP diameter and outermost zone width. A design file containing

[‡‡] 15.75 atoms/ion at 30 keV for 0° incident ions, it ranks 6th among the elements up to an atomic number of 92, outmatched only by Hg, Zn, Tc, Pa and Cd.

the positions of the empty zones (zones that will be milled out) is created using a MATLAB (The MathWorks, Inc. USA) script where the GDSII files are generated.[§§,58] The GDSII file is then transferred directly to the Raith Multibeam lithography attachment. The GDSII patterning file can also be manipulated in the Raith Multibeam software, which allows changing the width of the patterning lines, scaling the pattern file adding or deleting individual zones, etc. and also circular beam paths.

In the third step, the FZP zones are milled out using the optimized ion beam parameters (see Figure 3.1c). A drift correction step during the milling process may be necessary depending on the milling strategy, which requires the patterning of an alignment mark using FIBID. This step is not shown in Figure 3.1. After the FZP patterning a reference hole can be drilled to the membrane to be able to measure the incident X-ray intensity, I_0 during the synchrotron testing, which improves the accuracy of the diffraction efficiency calculations (see Figure 3.1d). To improve the image contrast and resolution, a beamstop is added using either focused ion beam induced deposition (FIBID), or direct-laser-write (DLW) (see Figure 3.1e). The effect of having a beamstop will also be discussed in Chapter 4.1.2.[***] If the beamstop is going to be made by FIBID, it has to be deposited after the FZP is patterned because of the unavoidable spillover deposition on the patterning area during the FIBID, which acts as a barrier and impedes FIB patterning. If the beamstop is going to be made by DLW, it is added after the Au sputtering step. This is because the patterning precision is higher in FIB compared to the in house DLW and the FZP zones can be patterned around the beamstop with better accuracy.

[§§] The MATLAB code that generates the GDSII files is written by Dr. Kahraman Keskinbora

[***] The negative effect of the beamstop is much more pronounced in multilayer FZPs because of the larger beamstop to diameter ratio.

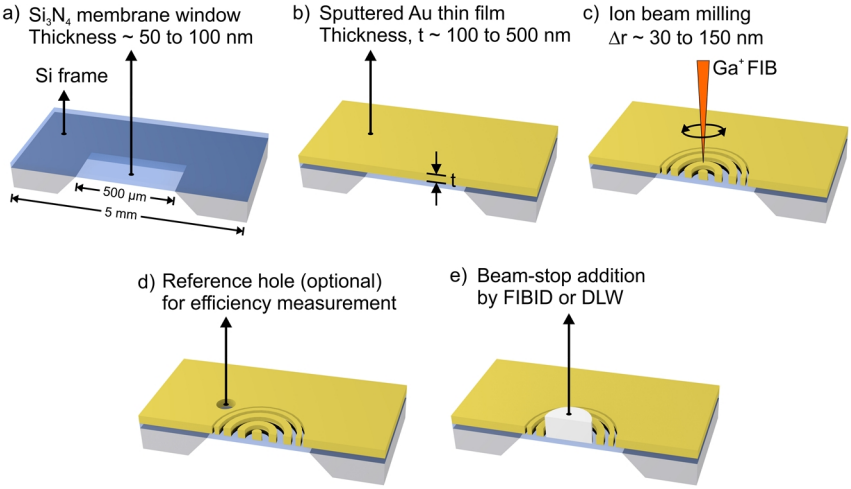

Figure 3.1 Schematics showing the fabrication stages of IBL-FZP. a) Cutaway drawing of the commercially available Si_3N_4 membrane. The membrane window is a Si_3N_4 rectangle of 50–100 nm located in the middle of a Si frame. b) Au thin film is sputtered using magnetron sputtering at a thickness generally between 100–500 nm depending on the desired X-ray energy range. c) The empty zones of the FZP are milled out using a Ga^+ FIB. The resulting FZP generally has an outermost zone width between 30–150 nm. d) For accurate diffraction efficiency measurement, a reference hole can be milled using Ga^+ FIB. This stage is optional as it only serves to improve the accuracy of efficiency measurements. e) A beamstop is added using FIBID or DLW.

3.3. Different FIB Milling Strategies and Consequences

Effect of Beam Voltage and Beam Current on Beam Size

The precision in FIB micromachining and achievable patterning resolution is dependent on the beam size and shape as well as the ion/matter interactions. The spot size is orders of magnitude worse than the wavelength of the ion beam owing to chromatic aberrations resulting from the space charge effects at the ion source and spherical aberrations resulting from the lens imperfections.[59] Nevertheless, the size and the shape of the focused ion beam can be altered by changing the accelerating voltage and the beam current. The beam current (and spot size) is adjusted by controlling the strength of the electrostatic lenses and by changing the aperture size.[60] In the FIB used for this thesis

(FEI Nova Nanolab 600), four different acceleration voltages can be selected, each having a different set of apertures delivering different beam intensity profiles and spot sizes. The expected spot sizes for different accelerating voltages and beam currents are shown in Figure 3.2.

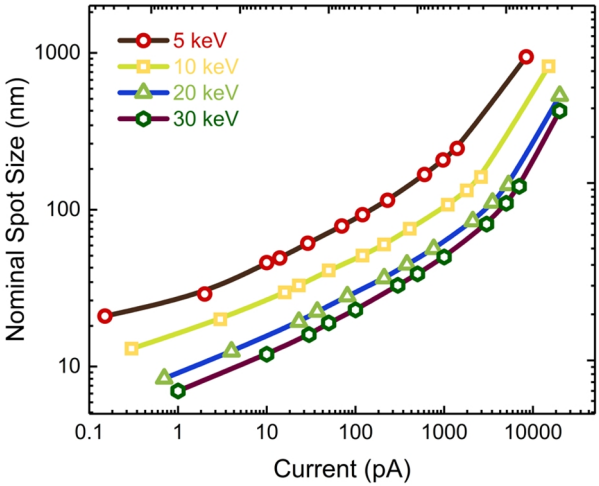

Figure 3.2 Expected spot size at the FIB used in this study as a function of accelerating voltage and beam current.

A tradeoff exists between the selected beam current and sputter rate. The beam current should be selected considering the desired feature size, depth, and area of the pattern.

The accelerating voltage also plays an important role in sputter rate, as the sputter yield (number of ejected particles per incident ion) changes drastically by the acceleration voltage. The sputter yield for Au at 0-degree projection is given in Table 3.1 for 5 and 30 keV Ga^+ ions.

Table 3.1 The effect of Ga^+ accelerating voltage on sputter characteristics based on TRIM calculations (ion channeling is neglected). Data were taken from Giannuzzi et al.[61]

	5 keV	30 keV
Sputter yield of Au at 0 degrees (atoms/ions)	10.19	15.75

Owing to a combination of reduced aberrations, smaller spot sizes, larger sputter yields, and longer ranges, a 30 keV accelerating voltage has been used for patterning the FZP structures for this thesis.

Different Milling Strategies

Various milling strategies that can be adopted when milling nano-patterns via IBL are summarized in Figure 3.3. Various factors that need to be taken into the account when deciding on the patterning strategies are also discussed below.

Single-Pass Exposure (SP-E)

Single-pass exposure patterning strategy is used generally for fast patterning. Longer beam dwell times are required because the necessary dose should be delivered to the sample in a single beam pass. When combined with high beam currents, the single-pass process may be fast enough that a drift correction hence the deposition of an alignment mark may not be required. The necessity of an alignment mark is also reduced if the feature sizes will be large.

However, the use of higher beam currents causes the beam size to be also large (see Figure 3.2). Therefore, the single-pass strategy is generally used when patterning FZPs with moderate or low resolutions. IBL-P3 is patterned using a single pass exposure strategy. Single-pass requires greater beam currents to be able to pattern fast so that there is not much beam shift.

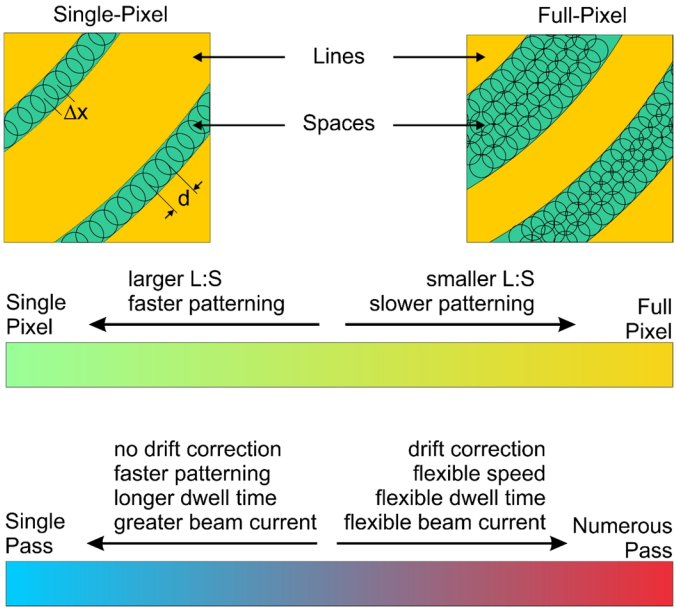

Figure 3.3 Schematic representation of IBL milling strategies. All the milling strategies are defined by two basic parameters, which are the number of patterning pixels and the number of beam passes. Different combinations of pixel and beam pass numbers can be optimized for different patterning properties.

Multiple Pass Exposure (MP-E)

In multiple pass exposure patterning strategy, the desired structure is patterned in multiple beam passes. It is generally used when the volume of milling is large. When patterning an FZP, two different multiple pass strategies can be used. In the first strategy, individual FZP zones are patterned starting from the outer zones in multiple exposures to their final depth and width before patterning an adjacent zone. This strategy delivers precisely placed outer zones and is used mostly to mill deeper structures than a single pass, to get rid of the re-sputtered material during previous passes without the need for a drift correction step. However, if the drift correction is to be avoided, the number of passes are kept rather low. IBL-P5 was fabricated using this strategy.

A second strategy in multi-pass exposure is to pattern every zone of the FZP in a single pass exposure; however, with a low dose and repeat this process multiple times until the necessary dose is reached. Generally, a drift correction of the sample is done after every single pass exposure of the full FZP pattern. The use of drift correction allows milling of large volumes with high precision. The drift correction also allows the beam speed, dwell time and beam current to be selected flexibly. IBL-P1, IBL-P2, and IBL-D1 are patterned using the MP-E strategy.

Single-Pixel Exposure

In single-pixel exposure patterning strategy, the FZP zones are milled along a single-pixel width, which is defined by the beam size. This causes every patterned zone to constitute the same width. Because the period of an FZP changes from inner to outer zones, FZPs produced by single-pixel exposure strategy has varying line to space (L:S) ratio. The single-pixel strategy is used for ultimate speed, and generally with a trade-off in first-order diffraction efficiency of the FZP. Besides, an L:S deviating from unity may cause higher diffraction orders to be more efficient. Therefore, FZPs fabricated using single-pixel strategy can be used for higher-order imaging. IBL-D1 is fabricated using a single-pixel strategy and has been shown to perform very well in high order imaging. It has to be noted that the diffraction efficiency of inner and outer zones will be different owing to different L:S ratios.

Full-Pixel Exposure (FP-E)

In FP-E patterning strategy, the width of the overlapped pixels in y-direction equals the zone width for a 1:1 L:S (see Figure 3.3 upper right image). In FP-E the beam spot size is generally selected to be much smaller than the zone with to avoid beam damage, making the patterning slower compared to single-pixel exposure. When optimized properly, FP-E strategy makes high-quality FZPs with 1:1 line to space ratios. Hence, the full pixel strategy is generally used for low-resolution FZPs with small diameters.

Any number of pixels between SP and FP is named in this thesis as Multi-Pixel Exposure (MP-E). MP-E strategy allows for using higher currents for the same zone width compared to FP-E, lowers the beam damage to adjacent zones and can be optimized to give a 1:1 line to space ratio, which is not available in SP-E. IBL-P2 and IBL-P3 were fabricated using MP-E strategy.

Patterning Parameters and Dose Calculation

Ion beam dose is a function of the beam current ($I\ [C/s]$), dwell time ($t[s]$) and step size in x and y axes (Δx and Δy) and is calculated by the following equation:

$$D_{CD}[{}^{C}/_{m^2}] = \frac{I\ [{}^{C}/_{s}] \cdot t[s]}{\Delta x \cdot \Delta y\ [m^2]} \qquad \text{Eq.(3.1)}$$

however, the necessary dose to reach a certain milling depth for a specific material is only a rough estimate and may vary significantly for different step sizes, beam currents and dwell times.[59] For example, considering the same dose, a multi-pass scan generally yields shallower milling compared to a slow single-pass scan because some of the ion dose will be sacrificed in the resputtering of the redeposited species during each beam pass.

In the case of a single-pixel patterning, there are no steps in y axis, and the dose is calculated according to:

$$D_{CD}[{}^{C}/_{m}] = \frac{I\ [{}^{C}/_{s}] \cdot t[s]}{\Delta x\ [m]} \qquad \text{Eq.(3.2)}$$

Probable scenarios owing to the use of a wrong dose are depicted in Figure 3.4. Figure 3.4a shows a typical overdose scenario. In this case, the tail[†††,62] of the ion beam

[†††] The ion beam intensity profile can be approximated by superposition of a narrow Gaussian function and a wider exponential function. Although the exponential function constitutes a lower current, it can still damage and worsen the patterning resolution.

focal intensity destroyed the Au zones. A strategy to reduce the damage to the neighboring zones is to decrease the pattern width. In Figure 3.4b, the same dose as Figure 3.4a was used, but instead of a 75 nm pattern width, 48 nm pattern width was used. Although using a smaller pattern width improves the structure quality and reduces beam damage on the neighboring zones if the used dose is too high the top parts of the neighboring zones will still be milled out, lowering their height. An example can be seen in Figure 3.4c, where the height of the Fresnel zones (denoted with the arrow 1) is ~30 % smaller than the height of the deposited Au (denoted with arrow 2). This phenomenon induces a hard limit to the desired aspect ratio.

The use of overdose will also cause the pattern to be milled too deep. For example, the structures in Figure 3.4b are milled too deep, owing to overdose. Unfortunately, the milling depth cannot be observed in a top-down view and a FIB cross-section and a tilted image is necessary. The region between the yellow arrows in Figure 3.4d shows the thickness milled into the Si frame.

For practical purposes and to reduce the optimization costs, the dose optimization is generally performed on the Si frame but has to be optimized with much more precision when patterning on the ~50 nm thick Si_3N_4 membrane window. If the dose is too high, then the beam will mill the thin Si_3N_4 membrane, and the structural integrity will be lost as depicted in Figure 3.4e. For a too low dose, then the Au will not be milled thoroughly, which will reduce the DE of the FZP.

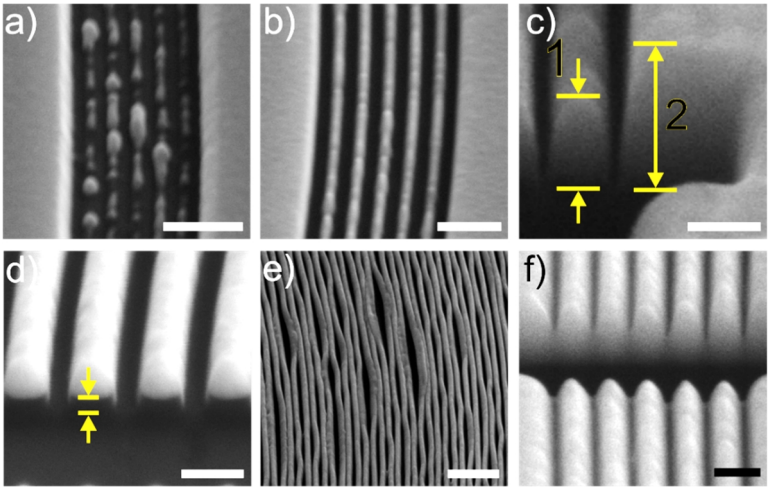

Figure 3.4 SEM images showing the effects of different line to space ratio and the dosage. a) Full pixel patterned with overdose. Scale bar is 500 nm. b) Less pixel patterned with the same dose as a. Scale bar is 500 nm. c) Cross-sectional image is showing the beam damage on the zones, causing a shortening of the Au zones (1) compared to the deposited Au (2). Scale bar is 50 nm. d) Cross-sectional image is showing too deep milling due to overdose. The section denoted with the yellow arrow is the frame. Scale bar is 250 nm. e) Au zones of an FZP patterned on the 50 nm thick Si3N4 membrane. The beam mills through the membrane deteriorating the structure of the FZP zones. Scale bar is 1 µm. f) Cross-sectional image of milled zones with an insufficient dose. Scale bar is 250 nm.

3.4. Design, Fabrication, and Results of IBL-FZPs

General Note on Imaging and Efficiency Experiments

X-ray testing of the IBL-FZPs were conducted at the MAXYMUS beamline. Besides the Siemens Star (SS) and the BAM-L200, a commercial Au-FZP made by e-beam lithography with an outermost zone width of 18 nm was also used as a test sample in this chapter. Additionally, ptychographic imaging of a Cu-Ni core-shell sample is demonstrated. The design parameters of the fabricated FZPs are summarized in Table 3.2.

Table 3.2 Summary of ion beam lithography parameters for different FZPs.

	IBL-P1	IBL-P2	IBL-P3	IBL-P4	IBL-P5	IBL-D1
Diameter	50 µm	100 µm	120 µm	120 µm	120 µm	75 µm
Δr	125 nm	75 nm	100 nm	100 nm	100 nm	50 nm
Zone Area	1473 µm^2	5026 µm^2	8482 µm^2	8482 µm^2	7678 µm^2	3927 µm^2
Beamstop	FIBID	FIBID	FIBID	FIBID	DLW	FIBID
Beamstop Diameter	20 µm	40 µm	56 µm	47 µm	67 µm	20 µm
Central Obs.	25 µm	60 µm	60 µm	60 µm	68 µm	25 µm
Thickness	220 nm	220 nm	225 nm	325 nm	350 nm	275 nm
Beam Current	100 pA	50 pA	100 pA	100 pA	300 pA	50 pA
Spot size	24 nm	19 nm	24 nm	24 nm	31 nm	19 nm
Dwell time	6 µs	2 µs	7.5 µs	240 µs	100 µs	470 µs
Step size	12 nm	10 nm	12 nm	12 nm	20 nm	10 nm
Dose	4.2 C/m^2	1.0 C/m^2	5.2 C/m^2	166.7 C/m^2	75 C/m^2	2.3 µC/m
Pass (No. of)	35	110	30	Single Pass	2	110
Total Dose	14583 C/m^2	11000 C/m^2	15625	16667 C/m^2	15000 C/m^2	258.5 µC/m
Drift Corr.	Yes	Yes	Yes	No	No	Yes
Strategy	FP-E	MP-E	MP-E	MP-E	FP-E	SP-E

IBL-P1

IBL-P1 was designed for being used during the commissioning of the new ptychography set-up at the MAXYMUS beamline starting on July 2015. At that date, commercial FZP with similar parameters cost over 10K€ with a delivery time of roughly six months.

Following the rough estimations on the optimum FZP parameters, a diameter of 50 µm combined with an outermost zone width of 125 nm, delivering a focal distance of 4.0 mm at 800 eV was decided as a first approach. A large focal spot size was chosen to reduce the necessary scanning points for less demanding computation during ptychographic reconstruction (discussed in Chapter 2.5). A larger depth of focus due to the relatively large outermost zone width also contributed to the easiness of the first ptychographic imaging.

In its fabrication, a FP-E strategy with image recognition based drift correction was used with the parameters given in Table 3.2, optimized to achieve a thickness of 220 nm and an aspect ratio of 1.76 and line to space ratio L:S of 1.

A beamstop made out of Pt of diameter 20 µm and thickness 2.1 µm was deposited using FIBID in the center of the FZP in three steps using the parameters listed in see Table 3.3. We start with the deposition a smaller disc (diameter 5.5 µm) of 1 µm thickness for a fast and straightforward Pt deposition. The spillover deposition of Pt around the 1st disc acts as a seed layer and provides nucleation sites for subsequent Pt layers and the deposition of the second step is faster. From my experience, starting directly with a large patterning area such as 20 µm directly with the parameters of Step 3 drills a hole into the Au layer and the membrane. The 3 Step deposition method also secures the center of the membrane. In the second step, a disc of 0.8 µm thickness covering a total area of 12 µm was deposited. The last Pt layer has a thickness of 0.3 µm and 20 µm diameter. Figure 3.5a shows SEM images of the IBL-P1 before and after beamstop deposition (inset image). Higher magnification SEM images in Figure 3.5b and Figure 3.5c show the outer and inner zones in higher detail, respectively.

Details of beamstop deposition and the amount of parasitic effects will also be discussed in Chapter 4.

Table 3.3 Beamstop deposition parameters.

	Diameter	Beam Current	Z size
Step 1	5.5 µm	100 pA	1 µm
Step 2	12 µm	0.5 nA	0.8 µm
Step 3	20 µm	1 nA	0.3 µm

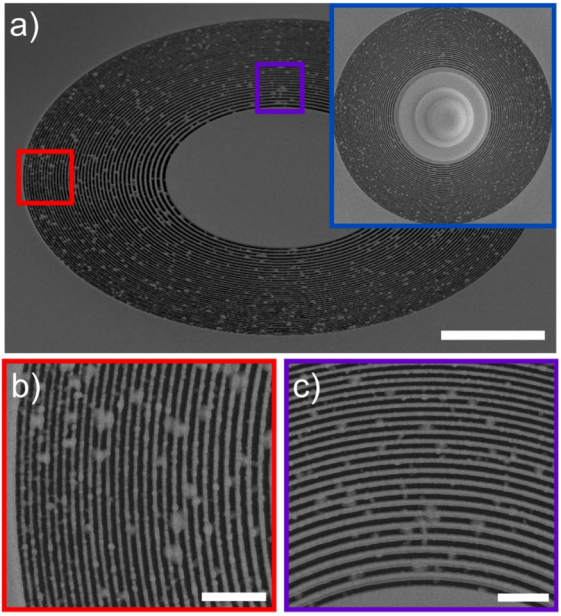

Figure 3.5 SEM images of IBL-P1. a) Low magnification image showing the whole FZP. Scale bar is 10 µm. Inset figure denoted with blue square shows the FZP after beamstop deposition. b) High magnification image showing the outermost zones from the red rectangle in the overall image. Scale bar is 2 µm. c) High magnification image showing the inner-most zones from the purple rectangle in the overall image. Scale bar is 2 µm.

Ptychographic imaging tests were conducted using the IBL-P1 as the focusing optic and a commercial EBL-FZP as the sample to reconstruct the phase and amplitude images

of an EBL-FZP.[‡‡‡] The ~20 nm outer zones of the EBL-FZP were clearly resolved in the reconstructed images as depicted in Figure 3.6a-b. The simultaneously reconstructed illumination function at the focal plane and in the propagation direction is shown in Figure 3.6c and d, respectively. The reconstructed illumination function fits well to the theoretical expectations.

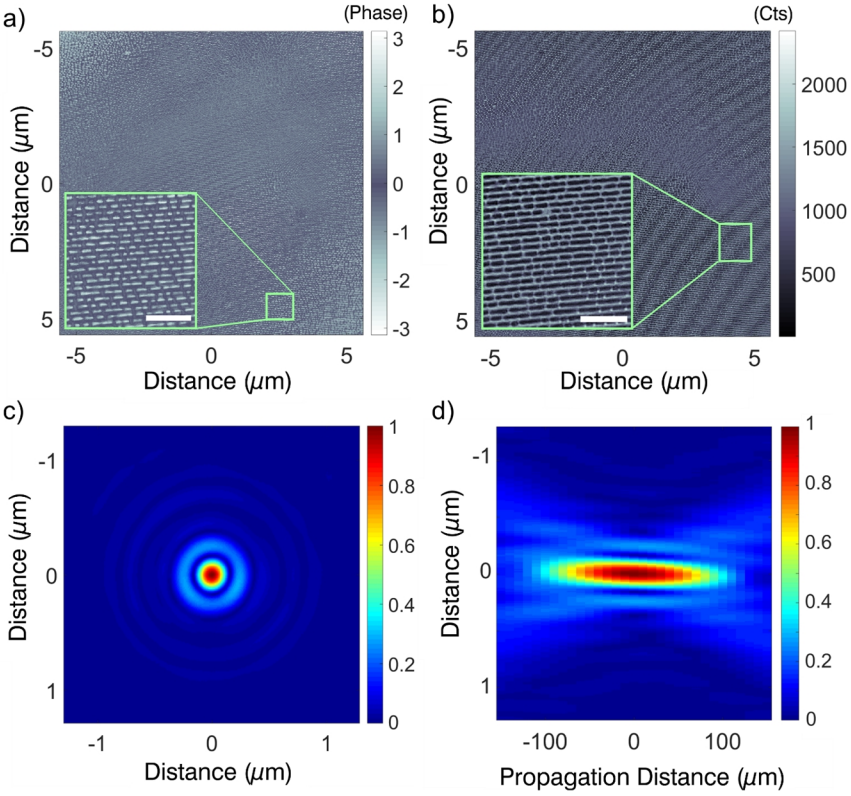

Figure 3.6 Ptychography test results of IBL-P1. A commercial EBL-FZP is used as a test sample. a) Reconstructed phase and b) reconstructed magnitude of the zones of EBL-FZP. Energy is 800 eV.

[‡‡‡] Due to the limited beam time available for these studies, a quantitative estimation of the diffraction efficiency was not possible for this zone plate.

Step size is 90 nm. Camera distance is 8 cm. 100x100 pixels. Effective pixel size is 9.8 nm c) Reconstruction of the illumination function at the focal plane. d) YZ-slice of the normalized magnitude of the wavefield propagated from -150 till 150 µm.

The far-field diffraction pattern obtained from a random scanning point (see Figure 3.7) shows that zero-order illumination (light passing through the beamstop of the FZP) is present on the CCD, covering almost 4 pixels. The intensity of the zero-order in Figure 3.7 is much less than the maximum intensity on the first diffraction order (1772 counts in the brightest pixel of the central 4 pixels vs. 4898 counts on the brightest pixel of the first diffraction order) which does not disturb the reconstruction. Unfortunately, the FIBID beamstop was too transparent at higher photon energies, transmitting roughly an order of magnitude more photons per 100 eV increase of X-ray energy. Therefore, for higher X-ray energies, the zero-order transmitted light saturated the central pixels. It has been experimentally observed that a saturated central pixel also saturates every pixel on the same horizontal axis (y=0) disturbing the reconstruction.

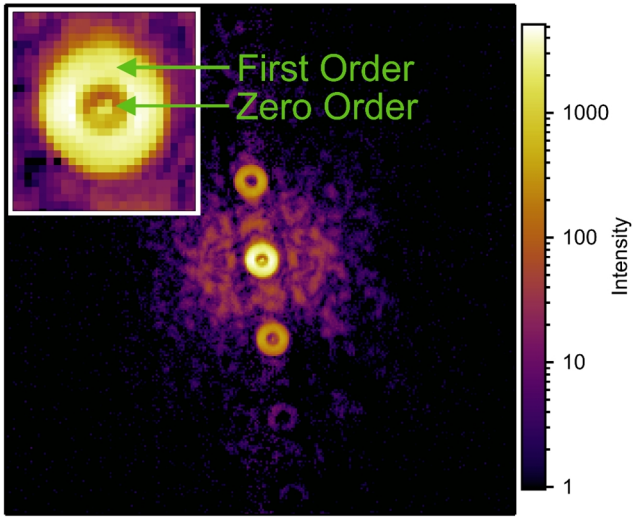

Figure 3.7 Far-field diffraction pattern of a random scan point captured with the CCD at 800 eV. The commercial EBL-FZP is used as a sample using the IBL-P1.

IBL-P2

Following the experiences using IBL-P1 for ptychography, IBL-P2 was designed as an upgrade. With a diameter of 100 µm and an outermost zone width of 75 nm, IBL-P2 has a NA of 0.01033 at 800 eV (1.6 times greater than IBL-P1) and an active zone area of 5026 μm^2 (3.4 times greater than IBL-P1).

In its fabrication, a MP-E strategy was used, with an altered design file (see Table 3.4) to achieve a roughly constant L:S ratio of ~4:1. A 50 pA beam current, 30 keV beam voltage, 2 µs beam dwell time, 10 nm step size, and 110 number of passes gave an area dose of 11000 $\mu C/m^2$, optimized to achieve a thickness of 220 nm and an aspect ratio of 2.93 (see Table 3.2). To account for any stage drifts and beam shifts, an image recognition based drift correction was performed after every pass.

Table 3.4 Selected pattern zone widths for IBL-P2.

	Inner Zones	**Middle Zones**			**Outer Zones**
Selected Pattern Width (nm)	80	70	60	50	40
Number of Zones	2	5	10	20	70

Also, the Pt beamstop design was altered for improved 0^{th} order suppression. The beamstop was deposited in 25 steps achieving a diameter of roughly 40 µm. At each step, a disk of diameter 12 µm and thickness of 1 µm was deposited using 0.5 nA beam current. The 12 µm diameter was selected to maximize the FIBID deposition rate.

Figure 3.8a shows SEM images of the IBL-P2 before and after beamstop deposition (inset image). Higher magnification SEM images in Figure 3.8b and Figure 3.8c show the outer and inner zones in higher detail, respectively. The effect of a slight overdose can be seen in the outermost zones in Figure 3.8b.

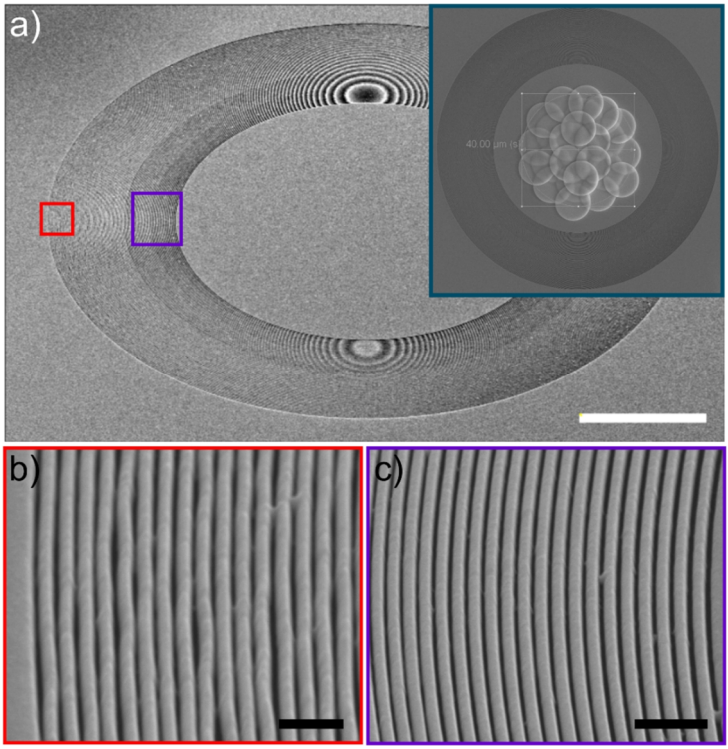

Figure 3.8 SEM images of IBL-P2. a) Low magnification image showing the whole FZP. Scale bar is 20 µm. Inset figure denoted with dark green square shows the FZP after beamstop deposition. b) High magnification image showing the outermost zones from the red rectangle in the overall image. Scale bar is 500 nm. c) High magnification image showing the inner-most zones from the purple rectangle in the overall image. Scale bar is 1 µm.

The performance of IBL-P2 is tested in direct imaging and ptychography experiments. On the membrane of the IBL-P2, there is no reference hole. So for an estimation of the DE, the flux passing the not-structured Au layer of 220 nm thickness was measured, and the incident intensity on the FZP was estimated using the Beer-Lambert law to be 293 using the parameters listed in Table 3.5 . Details of the diffraction efficiency calculation are explained in Appendix A. The DE was estimated to be 2.25 ± 0.34% at 1100 eV. The estimated efficiency value is strongly dependent on the measured Au thin

film thickness. An error of 10% is possible in the thickness measurement, which would yield a 15% uncertainty in the efficiency estimation.

Table 3.5 Parameters used in estimating Io for diffraction efficiency calculation.

I (counts)	μ (cm^2/g)	d (g/cm^3)	x (nm)
54	4015	19.15	220

Direct imaging experiments of the SS test sample were done at 800 eV. The second inner ring consisting of 60 nm lines and spaces at its inner edge were resolved (Figure 3.9a). Ptychographic imaging tests were done to reconstruct the phase and amplitude images of the SS test sample. Also with this FZP at 800 eV, and with a camera distance of 8 cm an effective pixel size of 9.8 nm was achieved. The innermost ring of the SS test sample with 30 nm lines and spaces is clearly resolved (see Figure 3.9b and c).

The simultaneously reconstructed illumination function at the focal plane and in the propagation direction is shown in Figure 3.9c and d, respectively. The reconstructed illumination function matches well with theoretical expectations. The first null was measured to be at 68.5 nm, where the theoretical first null is at 71 nm. The far-field diffraction pattern obtained from a random scan point of the 100 x 100 scanning points of Figure 3.10 shows a strong zero-order illumination on the CCD with 3386 number of counts (center pixel) versus only a maximum of 2061 in the first-order diffraction. For the same reasons discussed for IBL-P1, IBL-P2 would also suffer from pixel saturation at high X-ray energies.

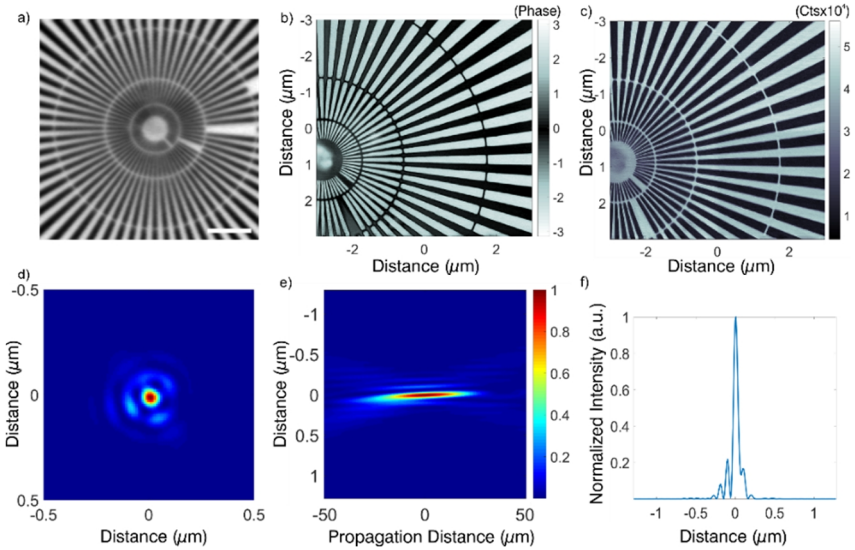

Figure 3.9 a) Direct imaging result of IBL-P2 using SS as a test sample. 60 nm lines and spaces of the second inner ring is clearly resolved. Energy is 800 eV. Scale bar is 2 µm b) Reconstructed phase and c) reconstructed magnitude of the zones of EBL-FZP. Energy is 800 eV. Step size is 60 nm. Camera distance is 8 cm. 100 x100 scanning points. Effective pixel size is 9.8 nm d) Reconstruction of the illumination function at the focal plane. e) YZ-slice of the normalized magnitude of the wavefield propagated from -50 till 50 µm. f) The measured focal spot intensity distribution

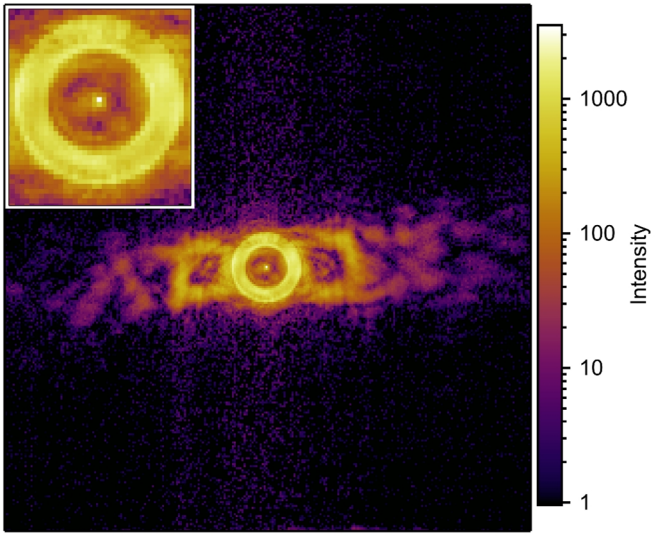

Figure 3.10 Far-field diffraction pattern of a random scan point captured with the CCD at 800 eV. The SS is used as a test sample.

IBL-P3

Besides increasing the diffraction efficiency, another way to increase the number of photons in focus is to make the spatial filtering slits wider, which also decreases the coherence. However, this may be partly overcome by using multi-mode ptychographic reconstruction algorithms.[63] Nevertheless, an increased incoming flux would create saturation points in the CCD camera if the beamstop is unable to stop the incoming beam. The IBL-P4 was designed as an FZP with a large beamstop. With a diameter of 120 µm and an outermost zone width of 100 nm, IBL-P3 offers a moderate focal spot size, and 1.7 times improved active zone area of 8482 µm^2.

For its fabrication, a MP-E was used with an altered design file (see Table 3.6) to achieve an L:S ratio of ~2.8:1 for the inner zones and ~4:1 in outer zones. A 100 pA beam current, 30 keV beam voltage, 7.5 µs beam dwell time, 12 nm step size, and 30 number of passes gave an area dose of 15625 µC/m^2, optimized to achieve a thickness

of 225 nm and an aspect ratio of 2.2. To account for any stage drifts and beam shifts, an image recognition based drift correction was performed after every pass.

Table 3.6 The selected pattern zone widths for IBL-P4

	Inner Zones	Middle Zones		Outer Zones
Selected Pattern Width (nm)	75	60	50	25
Number of Zones	7	16	50	49

A Pt beamstop of roughly 56 µm diameter was deposited in 30 steps. At each step, a disk of diameter 12 µm and thickness of 1 µm was deposited using 0.5 nA beam current. Figure 3.11a shows SEM images of the IBL-P4 before (left) and after (right) beamstop deposition. Excessive parasitic deposition of Pt over the FZP zones is clearly visible after the beamstop deposition. Higher magnification SEM images in Figure 3.11b and Figure 3.11c show the outer and inner zones before the beamstop deposition in higher detail, respectively.

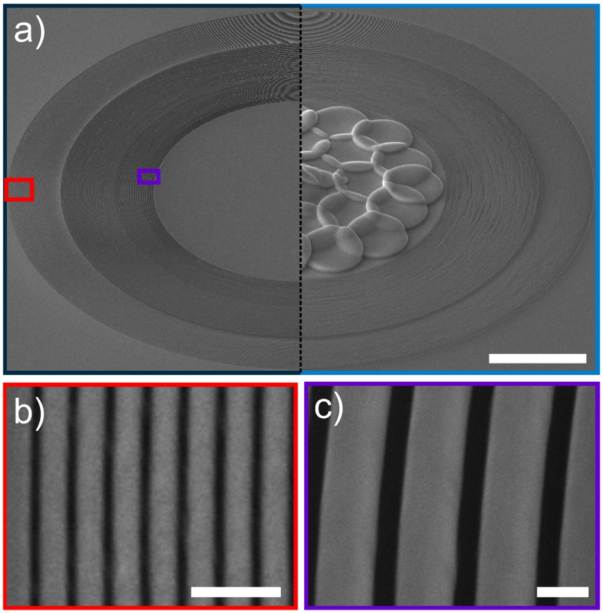

Figure 3.11 SEM images of IBL-P4. a) Low magnification image showing left half and right half of the FZP before and after beamstop deposition respectively. Scale bar is 20 µm. b) High magnification image showing the outermost zones from the red rectangle in the overall image. Scale bar is 500 nm. c) High magnification image showing the inner-most zones from the purple rectangle in the overall image. Scale bar is 250 nm.

As expected, the spillover Pt^{+} deposition on the zones of the FZP (see Chapter 4 for further discussion) caused a significant drop in the diffraction efficiency reaching only 0.63% ± 0.095 at 1200 eV. The diffraction efficiency test was done without a reference hole and estimated using the beer lambert law using the parameters listed in Table 3.7.

Table 3.7 The parameters used in estimating Io for diffraction efficiency calculation.

I (counts)	µ (cm^2/g)	d (g/cm3)	x (nm)
1563	3502	19.15	225

Ptychographic imaging tests were done to reconstruct the phase and amplitude images of the SS test sample. The innermost ring of the SS test sample with 30 nm lines

and spaces is clearly resolved with a reconstructed pixel size of 10.7 nm (see Figure 3.12a and b).

The simultaneously reconstructed illumination function at the focal plane and in the propagation direction is shown in Figure 3.12c and d, respectively. The first null was measured to be at 85.2 nm, much smaller than the theoretically expected value of 101 nm. The most probable reason for the smaller focal spot size is the spillover Pt^+ deposition covering the inner zones of the FZP. This causes the FZP to have a much larger central obstruction, and the focal spot intensity distribution would change accordingly. Calculations show that an FZP with the same diameter and outermost zone width would require a central obstruction of ~95 µm to yield a first null of at 85 nm. The high intensity in the side lobes (see Figure 3.12e) also supports this idea.

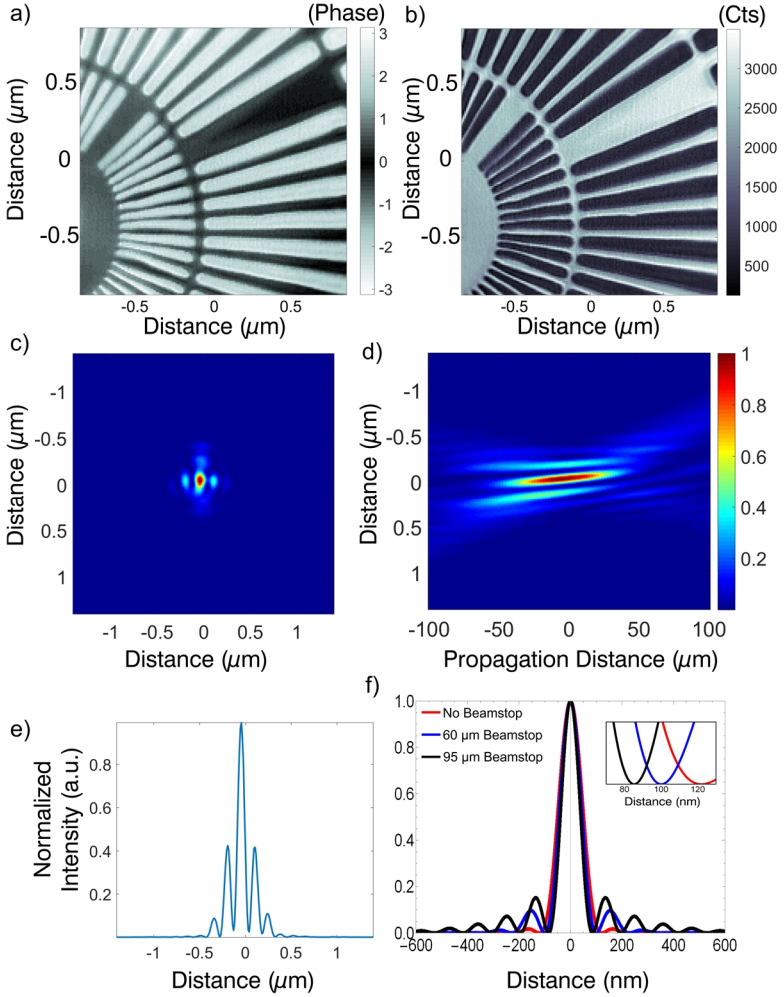

Figure 3.12 a) Reconstructed phase and b) reconstructed magnitude of the SS test sample. Energy is 780 eV. Step size is 60 nm. Camera distance is 8.5 cm. 20 x 20 scanning points. Effective pixel size is 10.7 nm c) Reconstruction of the illumination function at the focal plane. d) YZ-slice of the normalized magnitude of the wavefield propagated from -100 till 100 μm. e) Measured focal spot intensity distribution f) Simulated focal spot intensity distribution for an FZP with no central obstruction, 60 μm central obstruction, and 95 μm central obstruction.

To reduce the reconstructed pixel size, the sample should be as close as possible to the CCD camera, in the given configuration. A sample–camera distance of 4.45 cm was achieved by removing the sample scanning stages. In order to have a scanning microscopy image, the optical stage was raster scanned while the sample was kept stationary. This configuration resulted in a reconstructed pixel size of Δx = 5.1 nm at 852.9 eV (see Eq.(2.4).

Cu-Ni core-shell nanoparticles were imaged at 852.9 eV corresponding to the Ni-L_3 edge. The reconstructed amplitude image is shown in Figure 3.13a. The single crystalline Ni shells make very well defined edges, suitable for the knife-edge resolution estimation. The intensity variation on one of the sharp Ni edge is measured in a line scan integrated to 5 pixels width (orange rectangle in Figure 3.13a), and shown in Figure 3.13b.

A detailed ptychographic analysis of Cu-Ni core-shell nanoparticles investigated using IBL-P4 can be found in the dissertation of Iuliia Bykova.[53]

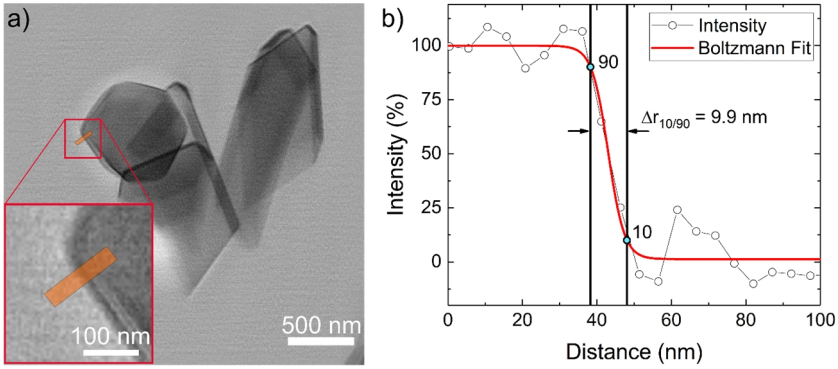

Figure 3.13 a) Ptychographic imaging of Cu-Ni core-shell particles using IBL-P4.[§§§] Energy is 852.9 eV. Camera distance is 4.45 cm. 35x35 scanning points with a step size of 80 nm. Effective pixel size is 5.1 nm. Scale bar is 500 nm. b) Knife-edge intensity profile of the orange rectangle of a). The distance for the intensity variation between 10% to 90% is calculated from a Boltzmann fit to be 9.9 nm.

[§§§] The core-shell nanoparticles were fabricated by the Central Scientific Facility (CSF) (MPI-IS Stuttgart). The ptychographic imaging was done by Iuliia Bykova and Dr. Markus Weigand.

Simulations show that when a focal spot with a perfect Airy distribution is scanned across a perfectly sharp edge, then the distance between the points where the intensity is 10% and 90% is roughly equivalent to the Rayleigh resolution.[18] This distance was measured from the intensity profile to be 9.9 nm (see Figure 3.13b). It would be safe to argue that to acquire an image similar to Figure 3.13a, an FZP with an outermost zone width of ($\Delta r_{10/90} \approx \Delta r_{Rayl.} \approx 1.22\ \Delta r$) 8.1 nm with a perfect airy focal spot would be required.

The far-field diffraction pattern of a random scan point of the ptychographic reconstruction of the SS test sample in Figure 3.14 is shown in Figure 3.14. Owing to the larger and thicker beamstop, the zero-order intensity in the far-field diffraction pattern is reduced compared to previous generation FZPs. The zero-order intensity on the CCD (center pixel) is measured to be 253 counts vs. 1593 in the first order. The inset figure shows the zero-order of the sample in higher magnification.

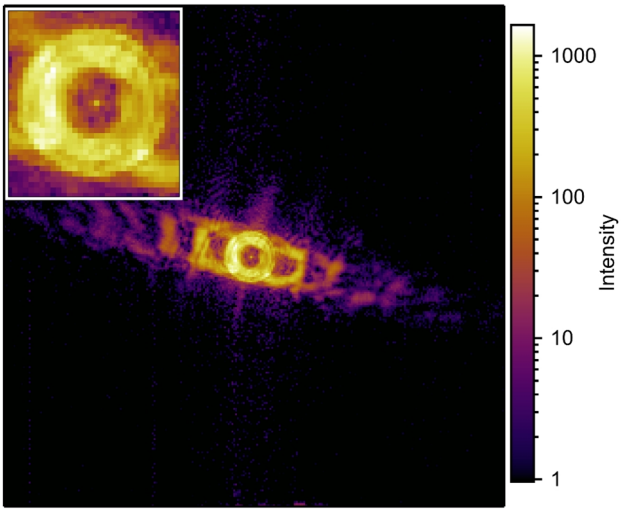

Figure 3.14 Far-field diffraction pattern of a random scan point captured with the CCD at 780 eV.

IBL-P4

IBL-P4 has the same diameter and outermost zone width as the IPL-P3. However, it has a much smaller beamstop, hence does not suffer from the spill-over Pt^+ deposition. It was delivered to the MAXYMUS beamline together with IBL-P3, in the case, the IBL-P3 would not work owing to the excess spill over deposition.

For its fabrication, a MP-E was used with an altered design file (see Table 3.8) to achieve a roughly constant L:S ratio of ~2:1. A 100 pA beam current, 30 keV beam voltage, 240 µs beam dwell time, 12 nm step size, giving an area dose of 16667 $\mu C/m^2$ in a single pass, optimized for a thickness of 325 nm and an aspect ratio of 3.25 (see Table 3.2). The patterning time was 51 minutes, and no drift correction was performed.

Table 3.8 The selected pattern zone widths for IBL-P4.

	Inner Zones	Middle Zones			Outer Zones
Selected Pattern Width (nm)	75	60	50	40	35
Number of Zones	7	16	40	22	27

A Pt beamstop of 47 µm diameter was deposited using FIBID. The Pt deposition started with the 3 steps of Table 3.3 until the beamstop is 20 µm in diameter and continued with depositing annuli instead of disks until the beamstop diameter reached 47 µm.

Figure 3.15a shows SEM images of the IBL-P3 before (left) and after (right) beamstop deposition. Higher magnification SEM images in Figure 3.15b and Figure 3.15c show the excellent quality of the outer and inner zones in higher detail, respectively.

This FZP has not been used up to now and is in stock for upcoming ptychographic studies at MAXYMUS. Therefore, the ptychographic reconstruction of the probe function and the DE measurements has not been determined yet.

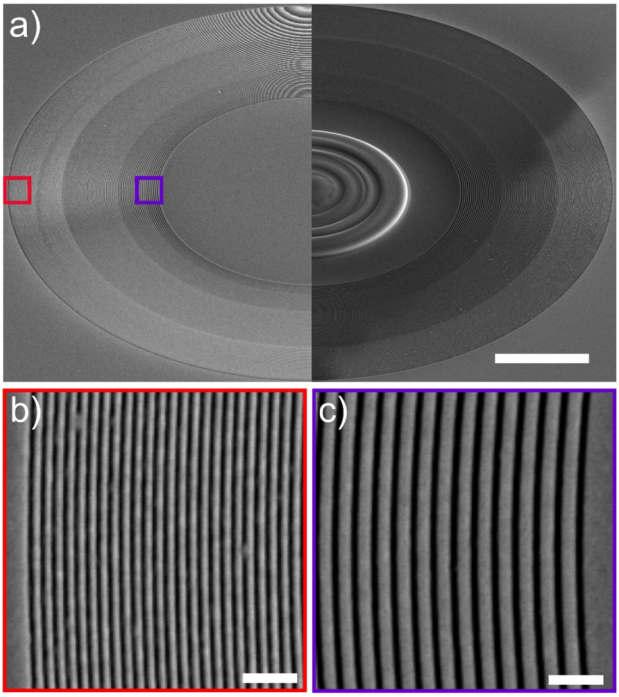

Figure 3.15 SEM images of IBL-P3. a) Low magnification image showing left half and right half of the FZP before and after beamstop deposition respectively. Scale bar is 20 µm. b) High magnification image showing the outermost zones from the red rectangle in the overall image. Scale bar is 1 µm. c) High magnification image showing the inner-most zones from the purple rectangle in the overall image. Scale bar is 1 µm.

IBL-P5

The spillover Pt deposition over the zone of IBL-P3 led to the development of a new beamstop fabrication technique.[****] Hereby, before IBL patterning, a cylindrical beamstop of 40 µm height and 67 µm in diameter was made by direct laser write (DLW). The fabrication steps are depicted in Figure 3.16. IBL-P5 was delivered to the MAXYMUS beamline on August 2017.

[****] The DLW beamstop development was co-coordinated by Margarita Baluktsian. The DLW beamstops are also used in the doped etched type FZPs developed in our department.

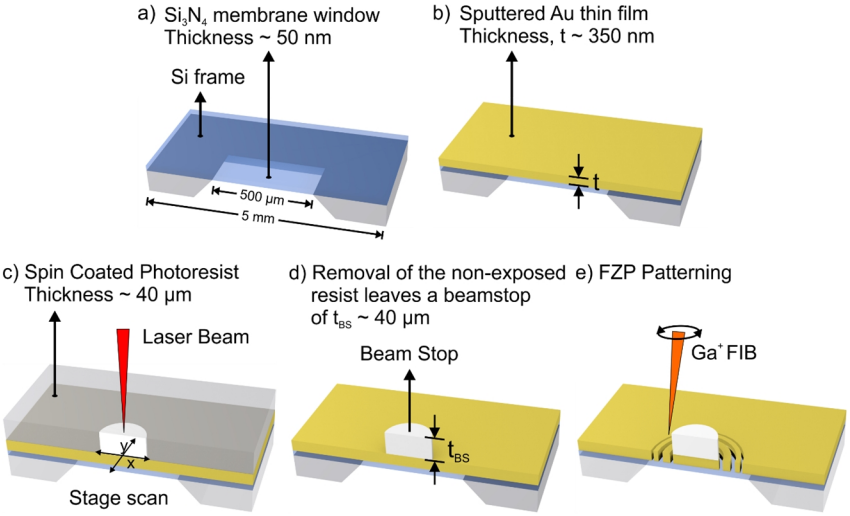

Figure 3.16 Fabrication steps of IBL-P5. A 50 nm Si_3N_4 membrane (a) is deposited with Au thin film of thickness ~350 nm (b). A direct laser write (DLW) beamstop is made by first spin-coating a curable photoresist of thickness ~40 µm and patterning using a UV laser beam (c). The non-exposed areas are developed in a solution to reveal the beamstop with ~40 µm thickness and 67 µm diameter (d). The zones of the FZP are then patterned using the Ga^+ FIB (e).

For the fabrication of the zones, FP-E strategy was used. A 300 pA beam current, 30 keV beam voltage, 100 µs beam dwell time, 20 nm step size, and 2 loops gave an area dose of 15000 µC/m^2, optimized to achieve a thickness of 350 nm and an aspect ratio of 3.5. The use of high beam current made the patterning process faster with a patterning time of only 35 minutes. Owing to the improved patterning speed, no drift correction was necessary. However, due to redeposition effects, the L:S was ~1 for inner zones and ~2 for the outer zones. Figure 3.17 shows SEM images of the overall as well as the inner and outer zones of the IBL-P5.

Thanks to the huge beamstop with a diameter of 67 µm and ~40 µm thickness, the zero-order illumination was completely suppressed in the ptychographic experiments. The suppression of the zero-order is seen in the far-field diffraction pattern of a random scan point captured with the CCD at 600 eV using IBL-P5 as the focusing optic and SS test sample in Figure 3.18.

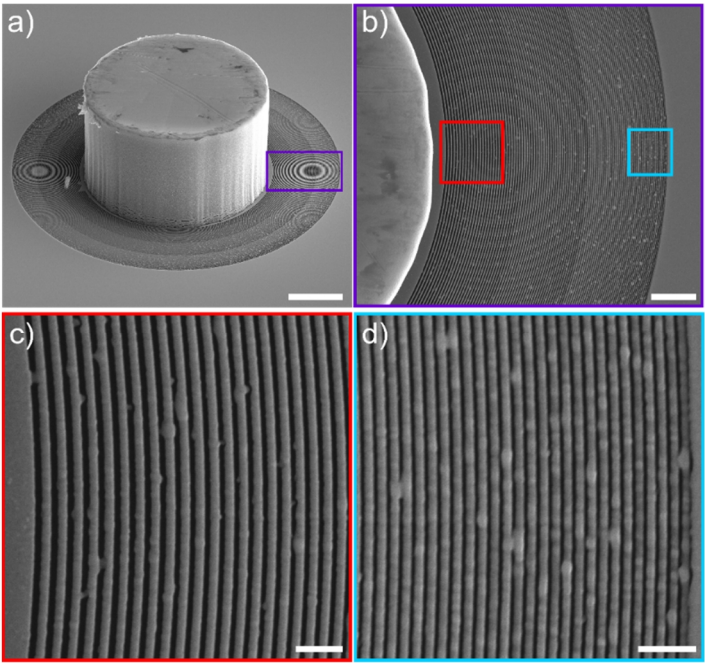

Figure 3.17 SEM images of IBL-P5. a) Low magnification image showing the whole FZP and direct laser written beamstop. Scale bar is 20 µm. b) Higher magnification image showing the right part of the FZP denoted with the purple rectangle in the overall image. Scale bar is 5 µm. c) High magnification image showing the innermost zones from the red rectangle region of (b). Scale bar is 1 µm d) High magnification image showing the outermost zones from blue rectangle region (b). Scale bar is 1 µm.

The effectiveness of the DLW beamstop is also visible in the efficiency measurements at higher photon energies. The pinhole scan at 1100 eV shows that 98.7% of the incoming intensity is absorbed by the DLW beamstop. The pinhole scan at 1100 eV is shown in Figure 3.19 with the first-order intensity, the suppressed zero-order intensity through the beamstop, the zero-order intensity through the FZP zones, the incident illumination I_0, and the dark counts labeled.

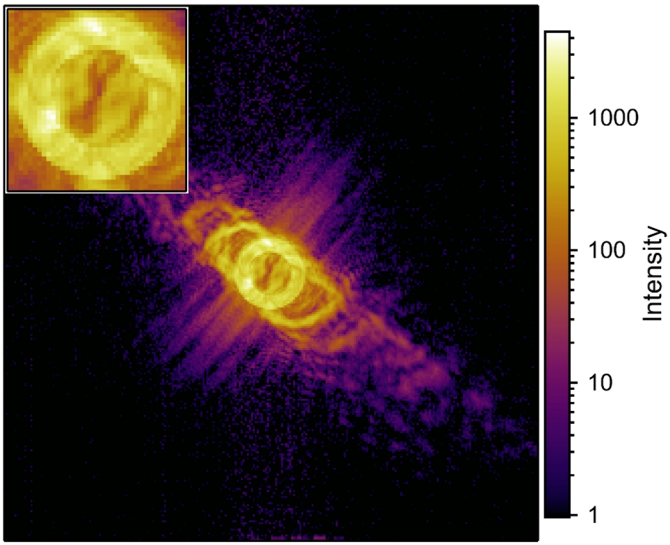

Figure 3.18 Far-field diffraction pattern of a random scan point captured with the CCD at 600 eV.

Thanks to the newly developed DLW beamstop, the spillover deposition was eliminated, and IBL-P5 has reached a diffraction efficiency roughly an order of magnitude greater than IBL-P4. The diffraction efficiency of IBL-P5 at various energies is listed in Table 3.9

Table 3.9 Efficiency measurement for IBL-P5.

Energy (eV)	Efficiency (%)
500	2.02
800	5.56
1100	4.85

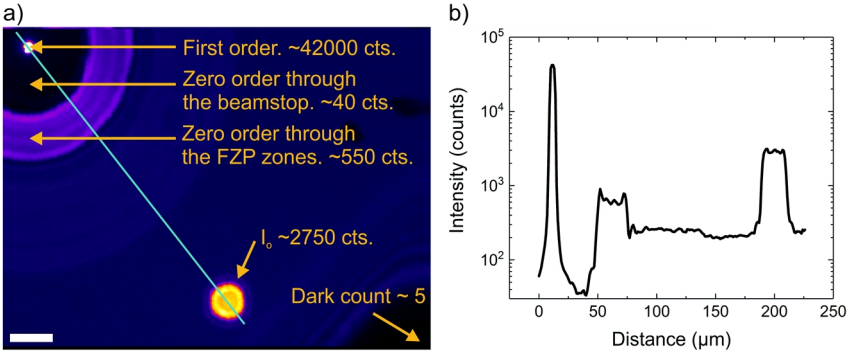

Figure 3.19 a) A pinhole of diameter 4.4 μm is scanned, and the transmitted light is collected by an APD. The great suppression of the zero-order intensity by the beamstop is clearly seen. The ratio of Io/ Zero-order through the beamstop shows 98.7 % absorption of the incoming intensity. Energy is 1100 eV. Scale bar is 25 μm. b) Intensity profile of the green line of a).

Ptychographic imaging tests were done to reconstruct the phase and amplitude images of the SS test sample as well as to reveal the intensity distribution at the focal spot[††††]. The innermost ring of the SS test sample with 30 nm lines and spaces is clearly resolved with a reconstructed pixel size of 14.8 nm (see Figure 3.20a and b). The simultaneously reconstructed illumination function at the focal plane and in the propagation direction is shown in see Figure 3.20c and d respectively. The first null was measured to be at 118.5 nm, larger than the theoretically expected value of 96.5 nm. The reason for the discrepancy is not understood.

[††††] The Ptychography experiments of IBL-P5 is conducted by Dr. Kahraman Keskinbora.

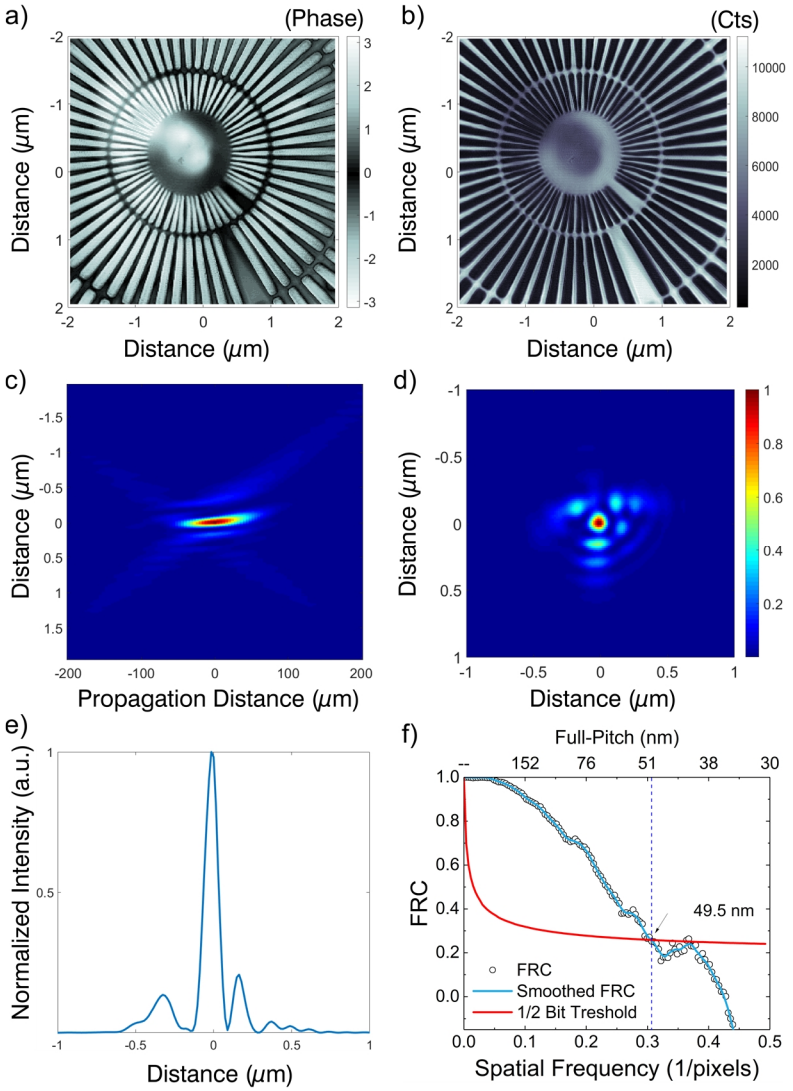

Figure 3.20 a) Reconstructed phase and b) reconstructed magnitude of the SS test sample. Energy is 600 eV. Camera distance is 9.1 cm. Dwell time 120 ms. Effective pixel size is 14.8 nm c) YZ-slice of the normalized magnitude of the wavefield propagated from -200 till 200 μm. d) Reconstruction of the illumination function at the focal plane. e) Measured focal spot intensity distribution. f) FRC calculated from two SS images similar to a). g) Simulated focal spot intensity distribution for an FZP with no central obstruction, 60 μm central obstruction, and 95 μm central obstruction.

IBL-D1

IBL-D1 was designed to serve at the MAXYMUS in direct imaging and spectroscopy experiments, especially to test for further development of direct imaging with high resolution in higher diffraction orders. The relatively efficient higher diffraction orders enable high resolutions without the need for changing to another optic, saving invaluable beam-time and making the FZP highly practical for the users. This can be, for example, beneficial if the scientific goal needs, e.g., spectroscopic information on a lower resolution and in parallel high resolution when the, e.g. optimum energy for the element-specific or magnetic contrast is found.

This FZP has an outermost zone width of Δr = 50 nm and an expected Rayleigh resolution of 61 nm (full-pitch) in its first diffraction order. In its fabrication a SP-E strategy with a constant 10 nm step size was used, leading to a L:S of about 2.3:1 in the outer zones and about 9:1 in the inner zones. A 50 pA beam current, 30 keV beam voltage, 470 µs beam dwell time, and 110 number of passes gave a linear dosage of 258.5 µC/m, optimized to achieve a thickness of 275 nm and an aspect ratio of 5.5. To account for any stage drifts and beam shifts, an image recognition based drift correction was performed after every pass (a total of 108 times). A Pt beamstop was deposited using FIBID in 3 steps with the parameters listed in Table 3.3.

It is the L:S being different than unity, that makes 2nd order focusing more efficient than usual. The diffraction efficiencies of the innermost and outermost zones of the FZP is calculated using CWT for the first 3 diffraction orders for 1100 eV X-ray energy and compared to the DE of the standard L:S of unity in the Table 3.10.

Table 3.10 Local diffraction efficiency calculations using CWT for the IBL-D1. The calculations were done considering an X-ray energy of 1100 eV, a zone thickness of t = 275 nm. Zone roughness and interdiffusion were neglected. The diffraction efficiency of a standard L:S of 1 is calculated and added to the table shown for comparison.

	1st Order DE (%)	2nd Order DE (%)	3rd Order DE (%)
Innermost zone (L:S = 9)	1.783	1.595	1.320
Outermost zone (L:S = 2.3)	11.47	3.797	0.224
Regular FZP (L:S = 1)	17.034	0.101	1.912

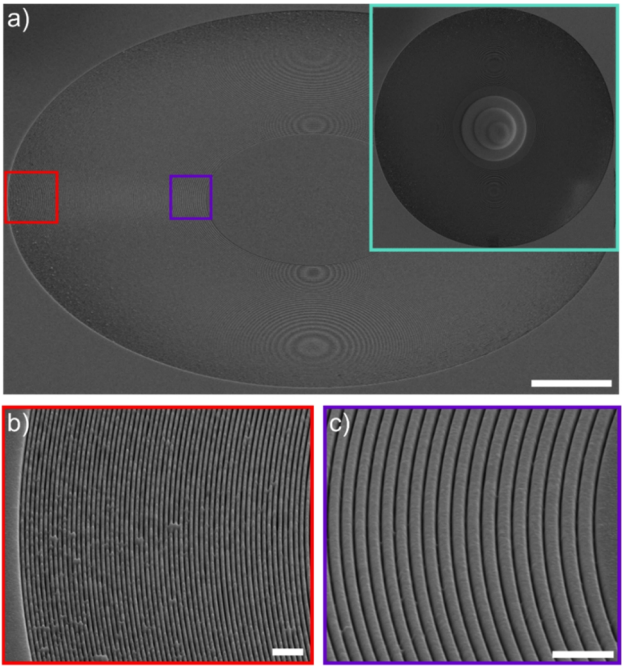

Figure 3.21 SEM images of IBL-D1 a) Low magnification image showing the whole FZP. Scale bar is 10 µm. Inset figure denoted with blue square shows the FZP after beamstop deposition. b) High magnification image showing the outermost zones from the red rectangle in the overall image. The L:S is about 1:3. Scale bar is 1 µm. c) High magnification image showing the inner-most zones from the purple rectangle in the overall image. The L:S is about 1:9. Scale bar is 1 µm.

Figure 3.21a shows SEM images of the IBL-D1 before and after beamstop deposition (inset image). Higher magnification SEM images confirm the high quality of the inner and outer zones alike (Figure 3.21b and Figure 3.21c).

The diffraction efficiency of IBL-D1 was tested at the first four diffraction orders for 800, 900, 1000, 1100, and 1200 eV X-rays and listed in Table 3.11. The first order efficiencies were greater than 2% at each tested X-ray energy with a maximum of 2.928% at 1200 eV. The measured DE at the first-diffraction-order is between the calculated diffraction efficiencies at 1100 eV, which is 1.783% and 11.47% for outermost and innermost zones respectively. The 2nd order diffraction efficiencies reached roughly 0.4%, much lower than the theoretically calculated values. Nevertheless, a measured diffraction efficiency of 0.4 % is on par with the first-order diffraction efficiencies of high-resolution zone plates. The third- and fourth-order focuses exhibit roughly 0.08 and 0.02% diffraction efficiencies respectively.

Table 3.11 The measured DE of IBL-D1 at the first four diffraction orders for different energies.

Energy (eV)	1st Order (%)	2nd Order (%)	3rd Order (%)	4th Order (%)
800	2.178	0.374	0.078	0.020
900	2.576	0.426	0.083	0.019
1000	2.654	0.424	0.081	0.020
1100	2.904	0.435	0.071	NA
1200	2.928	0.409	0.076	NA

Direct imaging experiments using the SS as a test object was done for the first four diffraction orders (see Figure 3.22). As expected, the signal to noise ratio was the best for the first diffraction order and reduced as the diffraction order increased, owing to the reduced efficiencies at higher diffraction orders. The smallest 30 nm features of the SS test sample were barely resolved in the first diffraction order. The improvement of the resolution at the second diffraction order is clearly visible in the STXM images of Figure 3.22c-d. The SS images obtained at the third and fourth diffraction orders do not show any improvement over the second order for the used test sample.

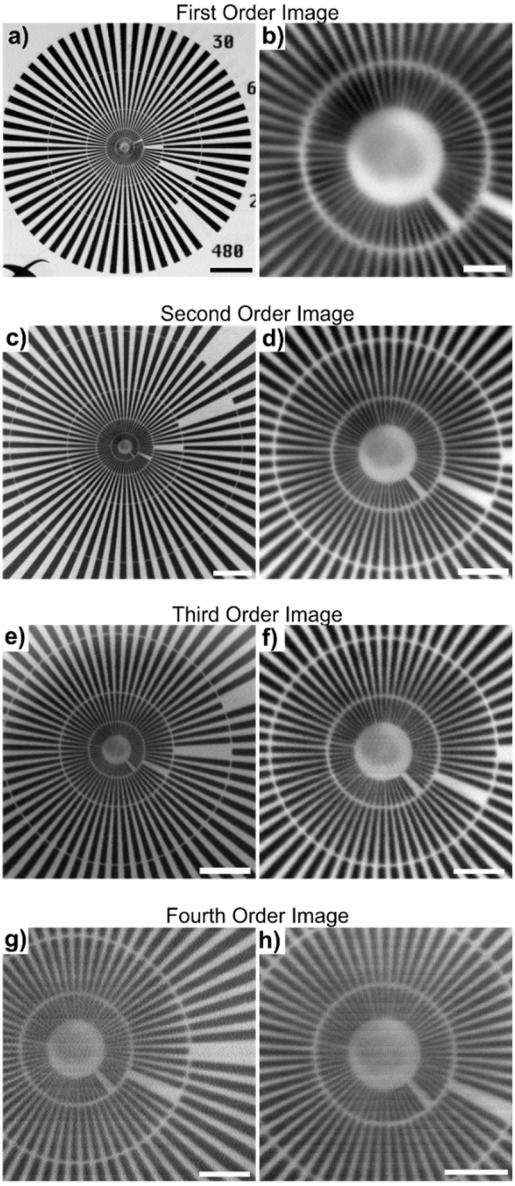

Figure 3.22 Direct imaging results of IBL-D1 using SS as a sample at 1st, 2nd, 3rd and 4th order focus. Images on the right side are higher resolution images. a) Energy is 932 eV. Dwell time is 5 ms, Step size is 63 nm. Scale bar is 5 µm. b) Energy is 100 eV. Dwell time is 3ms. Step size is 10 nm. Scale bar is 500 nm c) Energy is 800 eV. Dwell time is 0.227 ms. Step size is 20 nm. scale bar is 3 µm. d) Energy is 1000 eV. Dwell time is 3 ms, Step size is 12.5 nm. Scale bar is 1 µm. e) Energy is 1000 eV. Dwell time is 3 ms, Step size is 25 nm. Scale bar is 2 µm. f) Energy is 1000 eV. Dwell time is 3 ms, Step size is 10 nm. Scale bar is 1 µm g) Energy is 1000 eV. Dwell time is 5 ms, Step size is 10 nm. Scale bar is 1 µm. h) Energy is 1000 eV. Dwell time is 10 ms, Step size is 8 nm. Scale bar is 1 µm.

Direct imaging experiments of the SS at the 4th diffraction order prove that a diffraction efficiency of as low as 0.02% is sufficient for imaging experiments with a high contrast sample.

To measure the ultimate resolution of the IBL-D1, imaging experiments continued with the BAM-L200 sample which has much smaller features Figure 3.23 shows direct imaging experiments using the IBL-D1 as the focusing optic and BAM-L200 as the sample. Figure 3.23a-b shows the STXM image of the BAM-L200 sample using the first order focus, and Figure 3.23c shows imaging at the second-order focus. The 67.5 nm full period structure (P7) was resolved in Figure 3.23a. The integrated intensity and image contrast of figures a,b and c are depicted in d,e, and f respectively. Figure 3.23d shows the Michelson contrast, which is calculated from the integrated intensity (of the yellow rectangle of Figure 3.23a), to decrease as the frequency of the structures increase. Figure 3.23b shows 57 nm full period structure (P10) was resolved in the first diffraction order. Corresponding integrated intensity and Michelson contrast is shown in Figure 3.23e.

Figure 3.23c,e shows imaging experiments at the second diffraction order. According to Figure 3.23e, 48.5 nm full period structure (P8) was resolved cut-off with a very low Michelson image contrast.

Owing to a combination of low photon count in the focus and the lower contrast nature of the BAM-L200 sample, imaging was not possible at the 3rd and 4th diffraction orders. This proves the importance of the diffraction efficiency of the used optic in real-life scenarios. Most of the time, ultra-high-resolution FZPs are tested using only very high contrast samples such as the SS as a test sample, which fails to reflect the real-life performance of the FZPs.

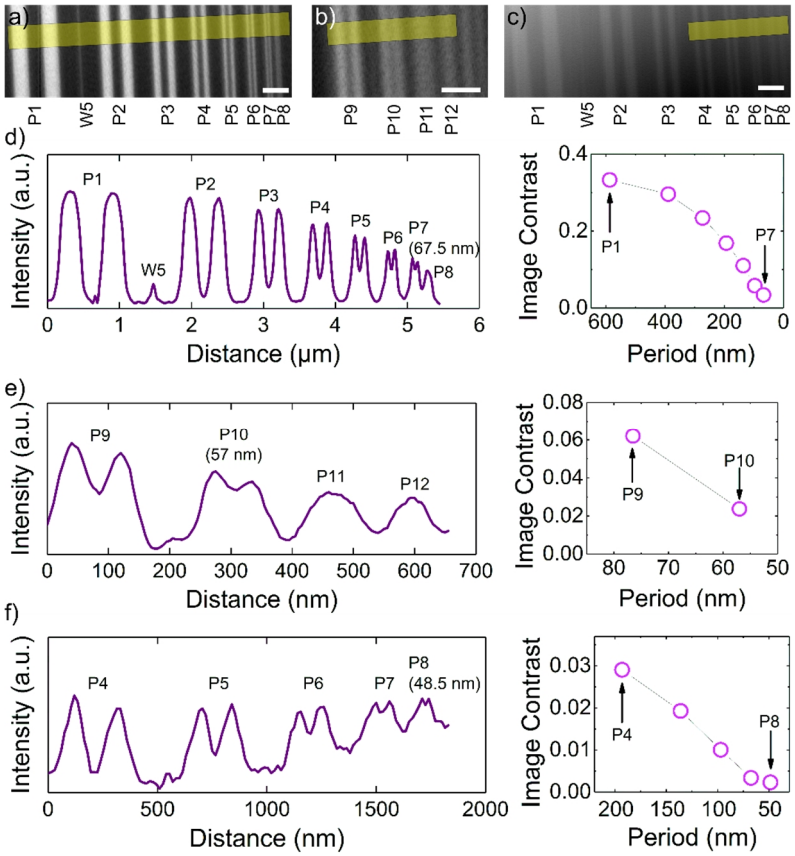

Figure 3.23 Direct imaging experiment using IBL-D1 as focusing optic and BAM-L200 test sample. a) STXM image of section D1 of the BAM-L200 sample using first-order focus. Photon energy is 1200 eV. Step size is 15 nm with 2 ms dwell time. Scale bar is 500 nm. b) STXM image of section D4 of the BAM-L200 sample using first-order focus. Photon energy is 1200 eV. Step size is 5 nm with 2 ms dwell time. Scale bar is 200 nm. c) STXM image of section D1 of the BAM-L200 sample using second-order focus. Photon energy is 1200 eV. Step size is 15 nm with 10 ms dwell time. Scale bar is 500 nm. d), e), and f) are intensity profiles and corresponding Michelson image contrasts acquired from the yellow area of a), b) and c) respectively. The image contrast using the second-order focus (f) is about an order of magnitude smaller than that of first-order (d).

3.5. Summary and Conclusions

Ptychography benefits strongly from the efficient use of the coherent flux ensured by employing an FZP. In comparison, when using a pinhole, >95 % of the flux is wasted. Moreover, the FZP-OSA pair acts as a monochromator and eliminates high order light coming from the undulator. This side benefit of the FZP makes the reconstruction much more straightforward. Enhanced flux through an FZP also increases the signal-to-noise ratio rendering the high-q signals recoverable. Having a divergent beam on the camera also improves the achievable q-space coordinates, improving the resolution.

In the process of incorporation of a ptychography experiment setup to the UE46-PGM2 beamline for MAXYMUS, we took advantage of our IBL expertise to deliver high performing zone plates in cooperation and discussion with the beamline scientists Dr. Markus Weigand and Dr. Iuliia Bykova.[53] The IBL-FZPs I delivered enabled ptychographic reconstructed imaging resolution down to 4.9 nm (half-pitch, knife-edge scan), and a maximum diffraction efficiency of 5.54 %.

The progressive improvement in lens properties such as larger diameters, optimized focal lengths, larger- and highly absorbing beamstops all contributed to the success of the project. Now, self-made IBL-FZPs are routinely utilized at MAXYMUS for ptychography experiments.

A main significant improvement of the present work compared to previous work from our group regarding IBL-FZP development (and in general to the literature) was the fabrication of larger diameter FZPs by using rapid prototyping IBL strategies I developed. Formerly, high-resolution FZPs could only be realized via IBL if the diameters were kept in the order of ~50 µm. The ptychography FZPs described in this work needed to have up to 120 µm diameters for the optimized utilization of coherent flux while complying with the focal length and spot size requirements leading to 5.8 times larger surface area compared to previous work. The large surface area ensures that the light collection capability is significantly higher than the previous work on IBL-FZPs.[58] However, this also means that the area to be machined using the IBL is also ~6 times larger.

Naturally, the low currents optimized for fabricating high-resolution IBL-FZPs[64] cannot be utilized for large area ptychographic FZPs, because of stage and beam drifts owing to long processing times.

The optimization of the zone plate and process parameters with high ion beam currents described in this chapter lead to the capability to machine large area FZPs in processes significantly shorter (as low as 31 minutes) than that of first successful imaging IBL-FZPs (~15 hours).[65,66]

By improving the beamstop fabrication method, our group also made significant strides towards efficient focusing optics optimized for ptychography at MAXYMUS.

Besides the technical improvements and the contributions to the science of the IBL, the work presented in this chapter has some economic implications for research groups working on X-ray microscopy and coherent imaging. The price of a commercial EBL-FZP that has similar parameters to the optics described in this chapter (100-120 µm diameter and 80 – 120 nm Δr) is in the order of a 10.000 $ in 2019 dollar value. Moreover, these commercial optics usually have 3-6 months of delivery time owing to the low yields of e-beam lithography processes used to fabricate the optics. This hinders the introduction of on-demand optics with tailored properties to the beamline with a rapid process cycle. The EBL has many process steps that accumulate fabrication errors and increase the chance of process failures. IBL, on the other hand, is essentially a single step nanofabrication technique. This aspect of IBL significantly improves the process yield and hence can drive the cost of a single device down significantly.

With the emergence of laboratory sources working at various wavelengths from EUV to hard X-rays, I expect the X-ray microscopy will not only be limited to the large scale scientific facilities but will be an integral part of research laboratories around the world. Some of these X-ray imaging and diffraction instruments can surely benefit from the nanofabrication capabilities shown in this chapter. Rather than being dependent on the commercial FZPs, laboratories who have access to FIB/SEMs, which is a reasonably

widespread instrument nowadays, can produce and experiment with own optics without worrying about the related cost of zone plates. This strategy was successfully followed when introducing the ptychography experiment to the MAXYMUS beamline.

4. Multilayer FZPs: Design, Fabrication, and Characterization

The work presented in this chapter has been partly published in:
Sanli, Umut Tunca, et al. "3D Nanofabrication of High-Resolution Multilayer Fresnel Zone Plates." *Advanced Science* (2018), 5(9), 1800346. The copyright for the article is held by the authors, and this is an open-access article under the terms of the Creative Commons Attribution Non-Commercial License. The manuscript text is written entirely by Umut T. Sanli.

The following persons contributed to the work presented in this chapter: The tilted micropillar arrays were fabricated by Dr. Chengge Jiao. The coupled-wave theory simulations (CWT) were done using a software provided by Prof. Dr. Gerd Schneider. The MATLAB codes for thin grating approximation used in diffraction efficiency (DE) simulations were developed by Dr. Nicolas Teeny and Dr. Kahraman Keskinbora. The HRTEM analysis (including EDX and EELS) were done by the Stuttgart Center for Electron Microscopy. XRR measurements were conducted by Marietta Dudek. XPS measurements were conducted by Michaela Wieland. WDX analysis was done by Dr. Julia Deuschle and Siglinde Haug.

4.1. Introduction

The recent advances in the lithography techniques indicate the possibility of making FZPs with even smaller outermost zone widths. For example, the patterning of a sub-5 nm single lines, and periods of 20 nm were recently shown via a He^+ ion beam lithography.[67] In the e-beam lithography front, the use of aberration correction allowed for patterning sub-5 nm structures.[68] Although, the recent patterning achievements are impressive in terms of nano-engineering capabilities, these achievements currently have little direct implications to the X-ray optics field. There are two reasons behind. First, the aspect ratios of those very narrow lines and spaces are very limited. Therefore, the fabricated optics do not currently reach the necessary optical thickness to focus X-rays

efficiently. Second, for outermost zone widths below ~50 nm and particularly for outermost zone widths below ~10 nm the diffraction behavior of the FZP is dominated by Bragg diffraction (see Figure 1.14). In this regime, the zones of the FZP need to be tilted to focus X-rays efficiently.

Typical diffraction efficiencies (DE) for standard commercial zone plates at soft X-rays are about 5 % determined at 700 eV from a commercial FZP of outermost zone width 18 nm which is used at the MAXYMUS beamline. However, the DEs rapidly decrease toward higher-energy X-rays.

For sophisticated FZPs with ultra-high resolutions, the efficiencies are generally below 1 %. As a consequence, other types of optics such as Kirkpatrick-Baez mirrors (KBM),[20,69] compound refractive lenses (CRL)[22,70,71] and multilayer Laue lenses (MLL)[72-75] are mostly used at higher photon energies. An overview of the mentioned optics has been given in Chapter 1.4.

Nevertheless, FZPs are still highly desired X-ray optics owing to their versatility and robust performance. Therefore, great efforts are being made to develop FZPs for the high photon energy range.[76-82] Hence, there have been some recent exciting improvements in the fabrication of high aspect ratio FZPs via the use of advanced multi-step lithography based methods. One example is the vertical metal-assisted chemical etching (v-MACE),[81] where low aspect ratio FZP zones are patterned using e-beam lithography and then etched via v-MACE to increase the zone height leading to higher aspect ratios. Via the v-MACE an FZP of aspect ratio ~1:40 have been fabricated with an effective outermost zone width of 60 nm.[81] However, detailed characterization of the zones and X-ray imaging results have not been shown, making the optical performance of the fabricated optics unclear.

Another technique for fabricating high aspect ratio FZPs is the zone doubling technique[76,83,84] where polymeric structures fabricated using e-beam lithography are deposited with a high atomic number material such as Pt via atomic layer deposition (ALD) to pseudo-halve the effective zone width and create high aspect ratio zones with a high refractive index.[76] High-aspect ratio FZPs can also be achieved by stacking several lower

aspect ratio FZPs to mimic a high optical thickness.[77,82,85-89] The mentioned techniques are all impressive advancements to the X-ray imaging field. However, they are still far away for targeting the aspect ratios required to focus high energy radiation to nanometer resolutions.

To have a figure of merit of the required aspect ratios, let us select Au as the FZP material, which has a relatively high δ in the X-ray regime. CWT calculations for 10 keV X-rays for an FZP of Δr = 10 nm, with tilted zones made from Au, shows that the optimum thickness is 3667 nm, corresponding to an aspect ratio of 367. The theoretical DE, as a function of thickness, for the selected Au FZP, is shown in Figure 4.1.

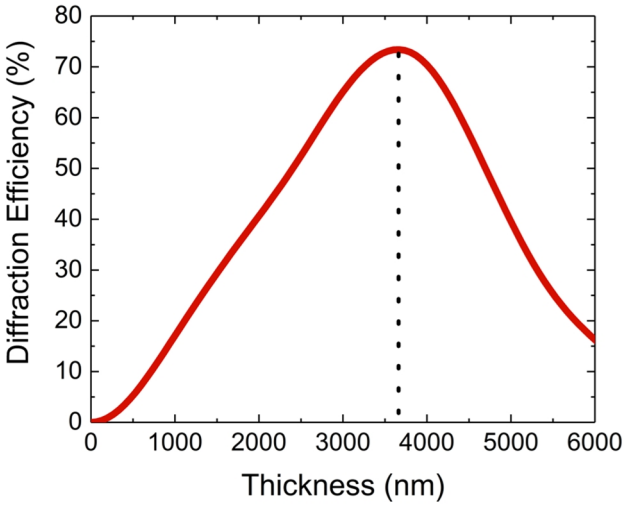

Figure 4.1: CWT calculation for a tilted binary FZP of Δr = 10 nm, made up from Au at 10 keV X-rays. An aspect ratio of 367 is needed to reach the optimum diffraction efficiency.

An attractive alternative for realizing the required high-aspect ratios, is to coat a cylindrical substrate of a well-defined, smooth surface with alternating layers of proper material combinations,[90] and subsequently slicing an FZP from the deposited substrate to the desired thickness which is known as “sputtered-sliced” or as denoted in this work

as "multilayer (ML)" FZPs.[91] Because the starting substrate can be very long (up to centimeters), and the thin film techniques allow for depositions in the nanometer scale, FZPs with virtually unlimited aspect ratios can be achieved using the sputter-sliced approach.

ML-FZPs offer a variety of advantages besides the virtually unlimited aspect ratios. As monolithic optics, they are easy to align compared to optics with multiple elements such as the in-situ stacked FZPs, MLLs, or KBMs. In addition, a single ML-FZP can deliver high performance over a wide X-ray energy range without realigning the optic, which is a direct advantage over the MLLs. Furthermore, ML-FZPs can be made out of chemically inert, high melting point ceramic materials that offer high mechanical strength and good resistance against bright X-ray pulses, which can benefit intense sources such as XFELs.

Since the first trials in the 1980s,[92,93] various groups have followed roughly the same approach where a metallic wire core is deposited using an omnidirectional deposition method such as sputtering or pulsed laser deposition while rotating the wire core to mimic a conformal deposition. Owing to a combination of fabrication related imperfections in the zones and sub-optimal imaging setups, demonstrated direct imaging resolutions have been much worse than the great potential suggested by indirect experiments.[94,95]

A recent method developed in our department for producing ML-FZPs is based on atomic layer deposition (ALD) of multilayers over optical quality glass fibers.[96] The ALD process allows atomic-scale precision in zone thickness and excellent conformality through its sequential, self-limiting surface reactions that lead to cycle based growth.[36] The superior conformality of ALD eliminates the need for rotating the glass fiber core and discards possible zone placement errors related to fiber rotation and directional deposition. A further advantage of ALD ML-FZPs over lithographic methods is the capability of coating a vast number of substrates conformally, such as centimeter long glass fibers or micro-pillar arrays. The optical thickness of each ML-FZP can be chosen freely, allowing the delivery of ML-FZPs optimized for a wide X-ray energy range, from a single deposition.

In this thesis, I use ALD to grow multilayers over optical fibers and focused ion beam (FIB) slicing to deliver ML-FZPs with high aspect ratios. In the following sections, I will discuss the quality of the thin film zones of the ML-FZPs using a variety of characterization techniques. Extensive synchrotron testing results will also be demonstrated. Finally, I will introduce a new fabrication concept for making ML-FZPs with precisely tilted zones for the first time. The implications of tilted FZPs (previously discussed in Chapter 1.5.2) will be presented following CWT. Also, the first direct imaging and DE results obtained by the titled ML-FZPs will be demonstrated.

State-of-the-art ML-FZPs

The performances of ML-FZPs have improved significantly in the last decade, owing to the improvements in thin film deposition and characterization techniques, advancements in the theoretical calculations, smoother core substrates, and imaging set-ups.

The performance of ML-FZPs can be assessed by three parameters. The first one is the active zone area. Currently, a major drawback of high-resolution ML-FZPs is their relatively small active area compared to lithographic FZPs. Although the drawback of having a small active area can be partly compensated using modern X-ray sources with much higher brilliance or by increasing dwell time in image scans, an FZP with a larger active area is still much desired for better quality images.

The active zone areas of the state-of-the-art ML-FZPs are compared in Figure 4.2. The graph is limited to ML-FZPs with outermost zone widths in the sub-micron scale. It should be noted that the Osaka Group have been developing quasi-kinoform type of ML-FZPs, aiming for highly efficient focusing of hard X-rays in the sub-micron scale, and have not targeted ultra-high resolutions so far.[97,98] The ML-FZPs from different research groups and different FZPs have an active zone area in the same order of magnitude, which is roughly about 10^3 μm^2, except for the Göttingen Group, which have much smaller active areas. The active zone areas of their FZPs have increased about two orders of magnitude in the last five years, with the focal spot size ≈5 nm.[99] However, an

imaging resolution of 5 nm has not been reported. Theoretical calculations predict that the reason for the mismatch between the direct imaging results and claimed focal spot size might be due to zone errors discussed in depth by Pratsch et al.[94]

In this chapter, the imaging performance denoted by Mark 1 and Mark 2 in the Figure 4.2 will be discussed. I fabricated and tested two more ML-FZPs which are denoted by A1 and A2 in the Figure 4.2. Even though A1 and A2 targeted higher resolutions and had smaller outermost zone widths, they have not surpassed the imaging resolution of the previously tested ML-FZP Mark 1 and Mark 2. More information about A1 and A2 can be found in the published proceeding articles (see ref.[100] for A1 and ref.[90] for A2).

The second parameter is the imaging resolution. In Figure 4.3, only ML-FZPs with direct imaging resolutions ≤ 50 nm in half-pitch are considered. A record imaging resolution of 15 nm is achieved, which will be discussed in detail in this chapter. The other notable ML-FZPs are fabricated by the Hyogo and Göttingen Group achieving 50 nm and 30 nm resolutions respectively.[101,102]

The third important parameter is the DE of the ML-FZPs. Unfortunately, there is no standard method for measuring the DE of an FZP. Furthermore, in the literature, the diffraction efficiencies are predominantly calculated using the thin grating approximation, and measured efficiencies are mostly not reported. For these reasons, a fair comparison of the diffraction efficiencies of different ML-FZPs is not possible.

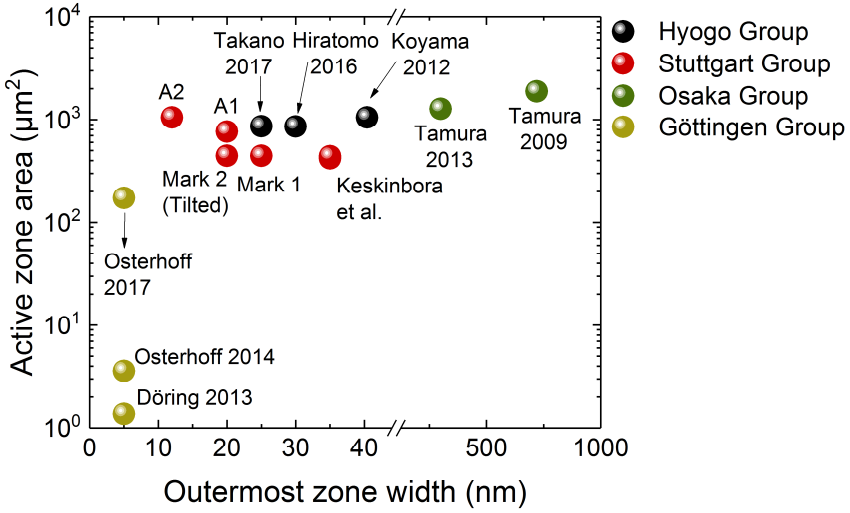

Figure 4.2: Comparison of active zone area and outermost zone widths of the state-of-the-art ML FZPs.

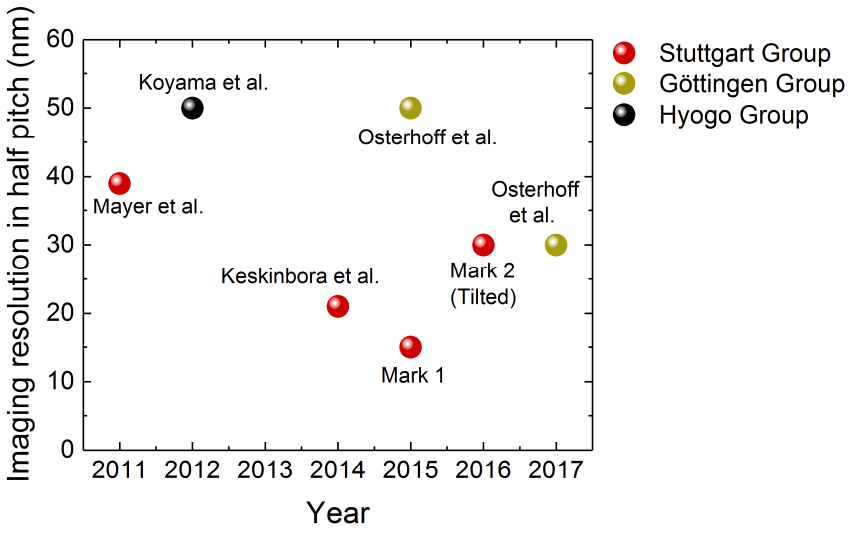

Figure 4.3: Comparison of the imaging resolution of the state-of-the-art ML-FZPs.

4.1.1. Materials Selection Methodology

For the selection of the materials of the multilayer zones of the ML-FZP, a strategy similar to that of Ashby is applied.[103] The materials selection strategy starts by translating the design requirements. The first step is defining the function of the device or component. Second, the constraints, which are absolute requirements, are defined to eliminate the materials that cannot do the job. Finally, the objectives are defined to be able to find the best materials for the desired function. The design requirements for ML-FZPs are listed in Table 4.1.

Table 4.1 The definition of design requirements in terms of function, constraints, and objectives.

Function	• Focus soft and hard X-rays to nanometer resolution with high DE.
Constraints	• The ALD precursor should be commercially available. • The precursors of the two layers should not etch each other. • The materials should have overlapping temperature windows. • The two materials should have similar thermal expansion coefficients to minimize stresses during cooling. • The precursor should be affordable for deposition thicknesses in the order of a few microns.
Objectives	• Maximize optical performance. - Maximize diffraction efficiency. - Maximize zone quality (low roughness, low interdiffusion). • Minimize fabrication time. - Fast ALD processes. • Maximize success chance. - Select ALD processes that are known to make high-quality thin films.

The design requirements for ML-FZPs are very complex with multiple constraints and conflicting objectives; therefore, the materials selection has to be done with compromises. Consequently, there is not a single correct solution to the materials selection problem. On the one hand, we want to maximize the theoretical DE. For very high-resolution ML-FZPs (towards the Bragg diffraction regime) with parallel zones, a material couple of a high-Z material and a low-Z material generally leads to a high theoretical DE.

Theoretical diffraction efficiencies of ML-FZPs consisting of material pairs available to ALD have been calculated to identify best material couples, and were previously published by Sanli *et al*.[90] However, as we have seen in Chapter 1.5.2 this generalization is not true for ML-FZPs with tilted zones. Therefore, the optimum FZP material changes by changing the outermost zone width and consequently, the design of the ML-FZP.

Furthermore, ALD of high Z metals like Pt and Ir are known to have higher surface roughness compared to ALD of oxide ceramics owing to the difficulties explained in Chapter 2.1. The surface roughness would, in turn, decrease the DE and the resolution of the ML-FZP. The effect of zone roughness on DE and on the resolution has been discussed in detail by Schneider[104] and Pratsch[94], respectively. On the other hand, we aim for faster, affordable depositions. Generally, the ALD of high-Z metals is relatively slow and expensive. For instance the Pt precursor, Trimethyl(methylcyclopentadienyl)platinum(IV), costs ≈€200/g, (vs. ≈€2/g for TMA) which may have been justified if the ML-FZPs were commercialized.

Refraction dilemma

Although ML-FZPs can be optimized both for soft and hard X-rays, they are expected to excel in the hard X-ray regime because they can reach extremely high aspect ratios, which are unavailable to lithographic techniques. Also, the preparation of ML-FZPs for hard X-rays is much easier than for soft X-rays because slicing thin FZPs is extremely challenging in the FIB considering the large apertures.[90]

However, the own-built (by the Department of Modern Magnetic Systems) soft X-ray microscope, MAXYMUS was chosen as the experimental set-up due to its access versatility and stability allowing for highly precise characterization of the focusing performance. Therefore, making FZPs using materials with similar refraction is beneficial owing to high optimum optical thicknesses which makes the FIB slicing easier.

4.1.2. Effect of Central Obstruction

The presence of the zero-order radiation in the focal plane induces background intensity and reduces the contrast of the final image. Therefore, it is generally preferred that the zero-order radiation from the central zones of the FZP is blocked using a beamstop. The radial intensity distribution of a centrally obstructed FZP is given by a modified version of Eq. (1.25):

$$I_1(\theta) = I_0 N^2 \left| \frac{2J_1(ka\theta)}{ka\theta} - a^2 \frac{2J_1(ka\theta)}{ka\theta} \right|^2 \quad (4.1)$$

where a^2 is the fraction of the area obstructed.

For a given FZP diameter as the beamstop diameter increases the following effects are observed: i) The central peak intensity in the focal plane decreases, ii) The amount of focused energy in the side lobes increases, iii) The central peak gets narrower, meaning a better resolution. The radial intensity distribution at the focus as a function of a is shown in Figure 4.4. The calculations are done for an FZP of outermost zone width Δr = 20 nm, and diameter, D = 38 µm.

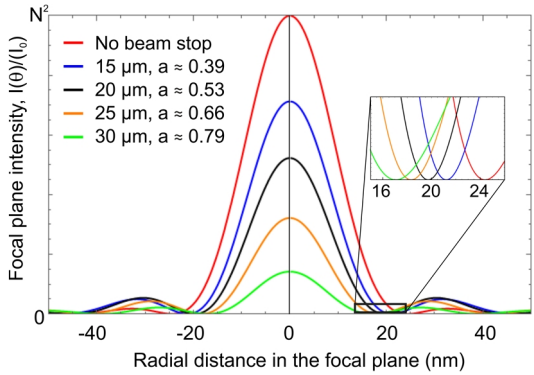

Figure 4.4 The first order focal plane intensity of FZP lenses with different beamstop diameters as a function of radial distance in the focal plane. Outermost zone width is 20 nm. N is the total number of zones in an unobstructed FZP.

4.1.3. Effect of Arbitrary Line-to-space Ratios

A binary FZP is composed of open and closed annuli, which can be approximated by a thin grating consisting of lines and spaces. In a ML-FZP, the lines and spaces correspond to the two materials of the FZP, where the lines define the material with higher refraction and spaces define the material with lower refraction. The line to space ratio (L:S) in a ML-FZP is defined as the ratio of the width of the more absorptive material (line) to the width of the less refractive material (space). It has been shown that the DE changes for different L:S.[105] CWT calculations show that the first-order DE of a rectangular ML-FZP generally decreases as the ratio of L:S differs from unity. Therefore, in rectangular ALD type ML-FZPs selecting a L:S different than 1:1 would not improve optical performance. The change in DE by changing L:S is depicted in Figure 4.5 for an Al_2O_3-SiO_2 FZP of outermost zone width Δr = 20 nm for 1000 eV.

In tilted FZPs, a L:S ratio different than 1:1 can be utilized to focus X-rays very efficiently to higher diffraction orders.[105] High efficient focusing in high diffraction orders is highly desired as the resolution scales down linearly with the diffraction order (see Eq. (1.28)).

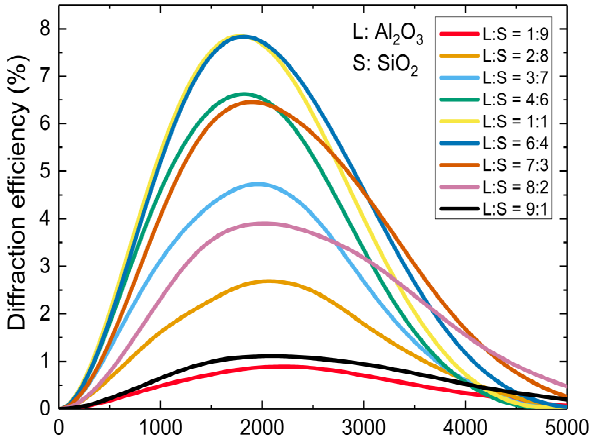

Figure 4.5: Diffraction efficiency as a function of line to space ratio. Energy = 1000 eV, Δr = 20 nm.

4.2. Design and Fabrication of ML-FZPs

Design

The materials selection strategy has been discussed at the beginning of the chapter. Al_2O_3-HfO_2 material couple is a great candidate which happens to satisfy all the constraints listed in Table 4.1. Furthermore, theoretical DE calculations using the thin grating approximation shows that ML-FZP made out of Al_2O_3-HfO_2 multilayers offer high diffraction efficiencies for both soft and hard X-rays (see Figure 4.6). Also, Al_2O_3 and HfO_2 are two of the most well defined ALD processes. Al_2O_3 is usually presented as a model ALD system[36], and ALD of HfO_2 has been used in commercial transistors as high - k dielectrics.[106] Al_2O_3 and HfO_2 are both oxide ceramics and their ALD thin films are expected to show low surface roughness. Another advantage of Al_2O_3 and HfO_2 is their high melting temperatures of 2072 and 2758 °C respectively, providing high chemical stability. For these reasons, Al_2O_3-HfO_2 material couple was selected as the zones of the ML-FZP.

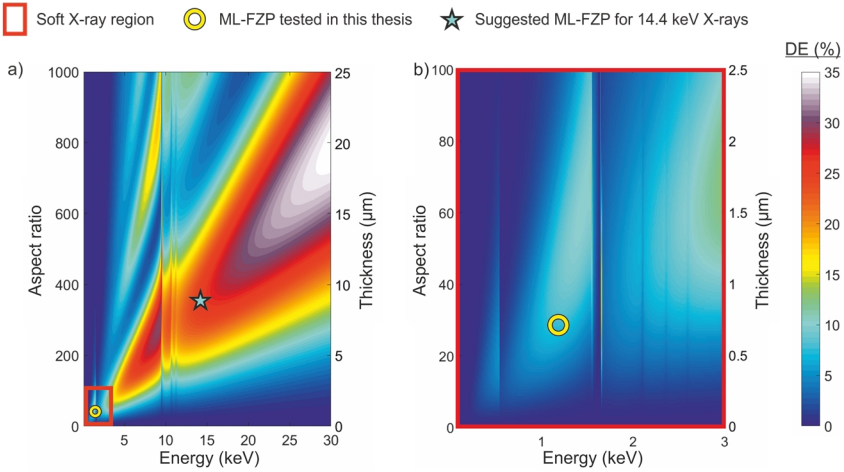

Figure 4.6 Diffraction efficiency maps of Al_2O_3–HfO_2 ML-FZP. Calculations were done according to thin grating approximation as a function of aspect ratio, optical thickness and X-ray energy a) DE

map from 100 eV to 30 keV. b) DE map of the region marked in red in (a). The corresponding numbers to color-coding represent the DE in percent. Figure adapted from Sanli *et al*.[33]

Fabrication

The Al_2O_3–HfO_2 multilayers were deposited via ALD at 290 °C on several optical quality glass fiber cores (Figure 4.7a,b), using the parameters listed in Table 4.2. Prior to deposition for the ML-FZP, the GPC of the Al_2O_3 and HfO_2 thin films were calibrated by test depositions on Si wafers via a spectroscopic ellipsometry and found to be 0.078 and 0.097 nm per cycle, respectively. A nonstandard 1:2 line (HfO_2) to space (Al_2O_3) ratio was used instead of the standard 1:1. This allowed for a faster deposition due to ~5 times shorter Al_2O_3 deposition cycle (see Table 4.2) in the expense of a reduced diffraction efficiency. The deposited glass fibers (Figure 4.7c) were sliced using a Ga^+ FIB as demonstrated schematically in Figure 4.7d. The ML-FZP was mounted on a Mo lift-out grid in the dual-beam instrument by using a micromanipulator. Prior to FIB slicing a protective layer of Pt was coated over the FZP by FIB induced deposition (FIBID) (Figure 4.7g). The ML-FZP was thinned down to an optical thickness of 700 nm via Ga^+ FIB, which is optimized for the soft X-ray range. An additional Pt beamstop layer of diameter d = 25 µm was deposited in the center of the FZP, also by focused ion beam induced deposition (FIBID) as illustrated in Figure 4.7f. The resulting ML-FZP has a diameter of d = 39.4 µm, outer-most zone width of Δr = 25 nm, inactive central obstruction of d_{co} = 31.4 µm with 4 µm of zone thickness, and an aspect ratio of 28. The scanning electron microscopy (SEM) images of the ML-FZP, prior to FIBID of Pt beamstop are shown in Figure 4.7g,h.

Table 4.2 The ALD process parameters used in the fabrication of Al_2O_3 - HfO_2 ML-FZP. The HfO_2 deposition cycle is much longer than Al_2O_3. The table is taken from Sanli *et al*.[33]

	Precursor	N_2 flow (sccm)	t_{Pulse} (ms)	t_{Purge} (ms)	Pressure (Pa)
Al_2O_3	TMA	80	20	1980	6.3
	H_2O	80	20	1980	
HfO_2	TDMAHf	40	40	15000	10.7
	H_2O	40	20	10000	

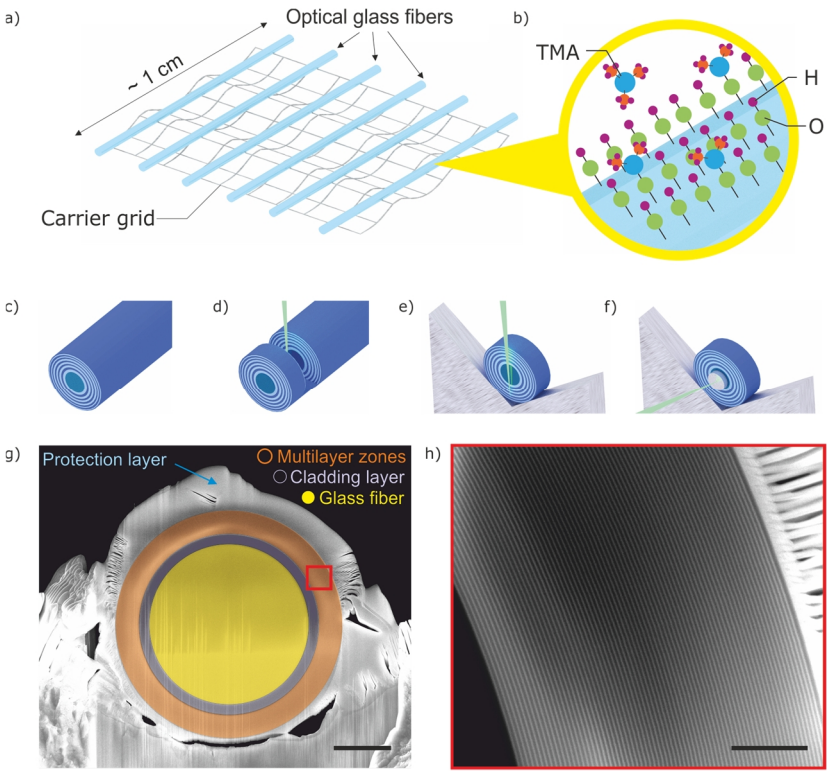

Figure 4.7 Fabrication stages of ML-FZP. a) Numerous glass fibers are mounted on a grid. b) Multilayer zones are deposited via ALD. Here, the deposition of the first Al_2O_3 layer is depicted by a pulse of trimethylaluminum (TMA) on an OH activated surface. A long deposited fiber c) is sliced d) and mounted on a Mo lift-out grid e) in the dual-beam instrument. f) A beam stopping Pt layer is deposited via ion beam induced deposition in the FIB. g) Scanning electron microscopy (SEM) image of the ML-FZP mounted on a Mo lift-out grid. Scale bar is 10 µm. h) SEM image of the multilayer zones defined with the red square of (g). Scale bar is 1 µm. The figure is adapted from Sanli *et al*.[33]

4.3. Results and Discussion of ML-FZPs

Characterization of the FZP zones

One concern in the X-ray optics community is that sputtered-sliced FZPs in general, tend to have zones with high roughness and low circularity, which has been shown to be

detrimental to the imaging capabilities.[94] To investigate the zone quality in the optical axis, a rectangular lamella was lifted out in the FIB from the deposited glass-fiber as depicted in Figure 4.8a. This sample was thinned down to about 250 nm for SEM analysis in the transmission mode (STEM), and below 100 nm for high-resolution transmission electron microscopy (HRTEM) analysis (see Appendix F). High-angle annular dark-field images (HAADF) of the zones in the STEM mode of an SEM is shown in Figure 4.8b,c. The multilayer zones keep their linearity and constitute very high structural quality even through an extended sample of 12.6 µm (Figure 4.8b) reaching an extremely high aspect ratio of above 500. The zones can be seen in higher magnification in Figure 4.8c–f. The HRTEM of the interface region shows a high mass-thickness contrast (Figure 4.8f). Fast Fourier transforms (FFT) in Figure 4.8f prove the multilayers to be amorphous. A line profile of the interface region of Figure 4.8f shows an interface sharpness on a molecular level (measured to be 0.84 nm), with a full width at half maximum (FWHM) of its first derivative being 0.33 nm at the interface transition (Figure 4.8g). The energy-dispersive X-ray spectroscopy (EDX) elemental mapping of Figure 4.8e demonstrates well-defined, high-quality zones with sharp structural and abrupt chemical interfaces. The electron energy-loss spectroscopy (EELS) map in Figure 4.8h presents the integrated Al-K and Hf-$M_{4,5}$ edge intensities confirming the interfaces of Al_2O_3 and HfO_2 to be chemically abrupt. This is attributed to the chemically stable nature of the amorphous ceramic films deposited via ALD, lacking fast diffusion paths such as grain boundaries. It has been shown that amorphous films, if dense enough, are better diffusion barriers due to lack of grain boundaries.[107-110] The chemical compositions of the thin films were estimated to be 38 at% Al to 62 at% O for alumina films and 34 at% Hf to 66 at% O for hafnia films by wavelength-dispersive X-ray spectroscopy (WDX). Chemical compositions were further confirmed to be Al_2O_3 and HfO_2 by EDX (Figure 4.8e), EELS (Figure 4.8h), and X-ray photoelectron spectroscopy (XPS) (Figure 4.9) analysis. The details of the methods used are given in Appendix E.

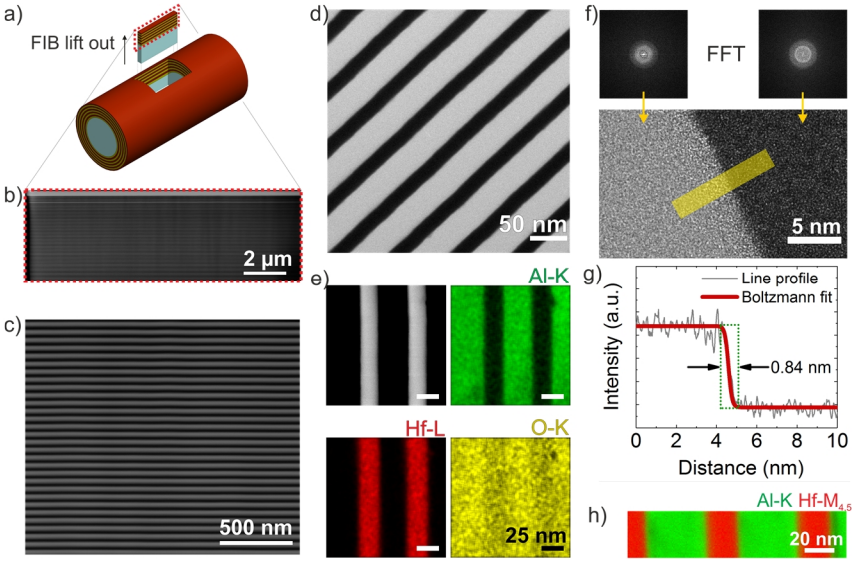

Figure 4.8 Characterization of multilayer zones along the optical axis. a) Illustration showing the location and orientation of the imaged sample. A rectangular prism is lifted out from the deposited fiber by using FIB. b) HAADF image of the lifted out lamella captured using STEM mode in dual beam instrument. The aspect ratio of the structure is larger than 500. c) Higher magnification image of the same lamella shows linear high-aspect-ratio multilayer zones. d) STEM bright-field image of the zones. e) STEM HAADF image and EDX maps of Al-K, Hf-L, and O-K. Scale bars are identical. f) HRTEM image of the Al_2O_3-HfO_2 interface and FFT confirming fully amorphous zones. g) Intensity line profile of the yellow region of the HRTEM image confirming molecularly sharp interface well below 1 nm. FWHM of the first derivative to the fitted curve is 0.33 nm. h) STEM EELS map of Al-K and Hf-$M_{4,5}$. Multiple linear least square fitting was used to subtract the background. The micrographs presented in d),e),f) and h) were acquired by Stuttgart Center for Electron Microscopy. The figure is adapted from Sanli *et al*.[33]

The XPS analysis shows very low (<1.5 at%) C for both Al_2O_3 and HfO_2 thin films. Volumetric mass densities of the thin films were estimated from electron density obtained by X-ray reflectometry (XRR) analysis and determined to be $\rho = 3.0$ g/cm^3 and $\rho = 8.9$ g/cm^3 for Al_2O_3 and HfO_2 thin films, respectively.

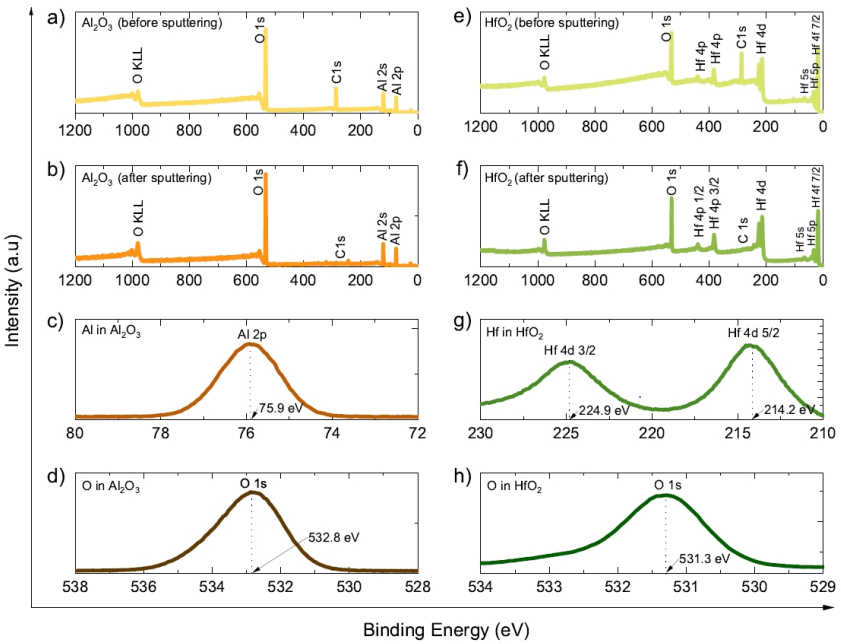

Figure 4.9 XPS spectra of Al_2O_3 and HfO_2 thin films fabricated via ALD on c-Si Wafer. a) Overall spectral graph of Al_2O_3 before Ar^+ sputtering. b) Overall spectral graph of Al_2O_3 after Ar^+ sputtering to eliminate surface contaminants. The C peak is not visible. c) Al-2p peak of the Al_2O_3 spectra. d) O-1s peak of the Al_2O_3 spectra. e) Overall spectral graph of HfO_2 before Ar^+ sputtering. f) Overall spectral graph of HfO_2 after Ar^+ sputtering to eliminate surface contaminants. The C peak is not visible. g) Hf-4d peak of HfO_2 spectra. h) O-1s peak of the HfO_2 spectra. XPS experiments were done by Michaela Wieland. The figure is adapted from Sanli *et al.*[33]

The effect of zone pattern inaccuracies

Inaccuracies in the zone pattern may reduce the resolution and DE of the FZP and cause aberrations. The effect of eccentricity, nonconcentric zones, radial displacement of the zones and zone roughness have been discussed elsewhere.[94,111] The ALD ML-FZPs with glass fiber cores are expected to have concentric zones (concentricity: $\gamma < 1.2\Delta r$) by the nature of the fabrication method. The eccentricity ($\Delta R/R$) was estimated to be 0.0032 and within the tolerance values[111] (eccentricity: $\Delta R/R < 0.35N^{-1}$) according to the meas-

urements from the SEM image of Figure 4.7g. Therefore, astigmatism or coma aberrations are not expected. However, if the deposition thicknesses are not strictly controlled, the stochastic nature of the bottom-up fabrication approach[112] may result in systematic or random radial displacement of the zones,[94] and induce spherical aberrations. The tolerable radial displacement of the outermost zone has been calculated to be within two outermost zone widths.[111] Considering an exact core diameter of 30 µm, the measured radial displacement of the outermost zone is 9 nm and well within the tolerable values (<2Δr). However, detailed characterizations of the glass fiber cores show that the diameter of different glass fibers varies between 30 and 31.5 µm. The zone plate demonstrated here has a measured core diameter of 31.4 µm. However, the multilayer design was made for an FZP core of 30 µm. This causes a systematic radial displacement of the zones by 700 nm. If the zone thicknesses are accurate, the systematic shift of the zones arising from non-exact diameter of the inactive core is expected to slightly modify the distribution of the field intensity of the focusing ring.[113,114] This effect was simulated using Fourier beam propagation method, confirming a negligible alteration in the focal plane intensity distribution (see Figure 4.10).

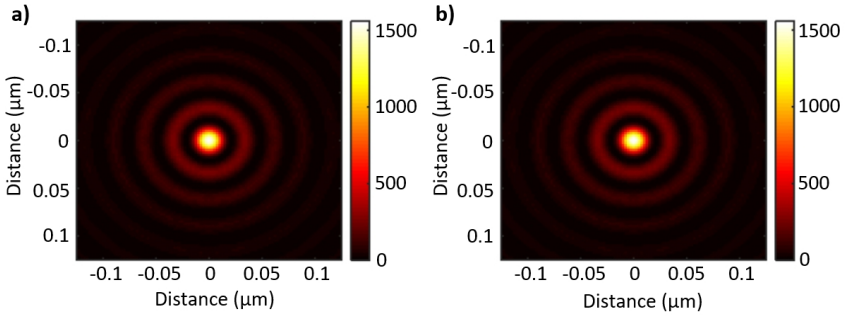

Figure 4.10 Fourier beam propagation simulations for an FZP with 30 µm beamstop diameter and perfect zone positions a) and for an FZP with 31.4 µm Beamstop diameter and 700 nm systematically shifted zones b). The change in the intensity is trivial. Simulation was done by Dr. Kahraman Keskinbora. Figure adapted from Sanli *et al.*[33]

STXM results and discussion

The DE and resolving capability of the ML-FZP were tested at the MAXYMUS beamline. ML-FZP was aligned in pitch and yaw using an in-house constructed tilt stage until a full 1st order diffraction ring was achieved. Figure 4.11a shows the image of the diffraction ring after tilt-alignment. A pinhole scan shows the incident illumination, the zero-order, and the 1st order intensity (Figure 4.11b). The diffraction efficiencies are also measured from such pinhole scans.

The features of the Siemens Star (SS) test sample was imaged, and the innermost 30 nm structures were resolved at 1198 eV photon energy as shown in Figure 4.11c. To check the ultimate imaging resolution, the BAM-L200 was imaged as presented in Figure 4.11d,e. The 30 nm full period structure (P12), corresponding to a 15 nm half-pitch, was resolved (cut-off) in Figure 4.11e. As of January 2019, this is the highest imaging resolution obtained by using a circular ML-FZP to the best of my knowledge.

It has been discussed in Chapter 4.1.2 that the presence of a central obstruction causes the intensity in the focal spot to shift to side lobes. This has two further effects for high-resolution FZPs. It causes a halo effect around the imaged structures, and the modulation transfer function increases at high frequencies just before the cut-off resolution.[94] These effects can be seen in Figure 4.11d and e, respectively. The effects arising from large central obstruction would be significantly reduced by increasing the deposition thickness.[94] The DE measurements were conducted via scanning a pinhole over the FZP (Figure 4.11b) at various X-ray energies. The measured diffraction efficiencies were found to be lower than ideal. A comparison between the measured and theoretically calculated values is shown in Table 4.3. The less than ideal DE can be attributed to several independent sources: i) a slight imperfection in the zone positions, ii) parasitic deposition of a platinum–gallium–carbon (Pt–Ga–C) layer over the zones during deposition of the beamstop via FIBI, iii) possible thickness variation of the ML-FZP in the optical axis, and iv) curtaining effects during FIB slicing and polishing.

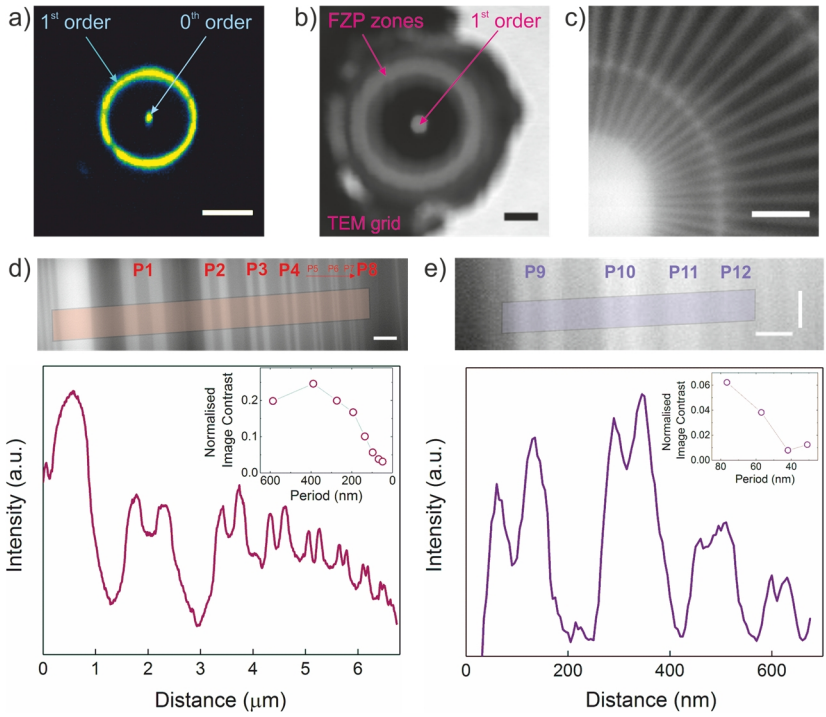

Figure 4.11 Synchrotron experiments at MAXYMUS. a) Charge-coupled device (CCD) image of a scintillator screen showing the 1st order diffraction ring. For this image, an order selecting aperture was placed between the FZP and CCD. The scintillator screen was placed further away from the focal point, and the image on the screen was magnified onto the CCD detector. The ML-FZP tilt was corrected via a tilt stage until a circular first order focus ring was obtained. The presence of the zero-order hints a misalignment of the OSA. The scale bar is 250 nm^{-1}. b) Pinhole scan over the FZP to measure the diffraction efficiency. The transmitted light is collected by an avalanche photodiode (APD). Dwell time 2 ms. Step size 500 nm × 500 nm. Photon energy is 1400 eV. Scale bar is 10 µm. c) STXM image of the SS test pattern. The 30 nm features of the innermost ring are resolved. Dwell time 10 ms. Photon energy is 1198 eV. Step size 10 × 10 nm. Scale bar is 500 nm. d) STXM image of P1 to P8 of the BAM-L200 test structure (top) and its integrated intensity profile and normalized Michelson image contrast (bottom graph). All features P1 (587 nm)-P8 (48.5 nm) are resolved. Dwell time 10 ms. Step size 10 × 10 nm. Photon energy is 1200 eV. Scale bar is 500 nm. e) STXM image of the P9 (76.5 nm) to P12 (30 nm) of the BAM-L200 test structure (top) and its integrated (15 pixels wide) intensity profile and normalized Michelson image contrast (bottom graph). 30 nm full period structure (P12) is resolved corresponding to 15 nm half-pitch cut-off resolution. Dwell time 30 ms. Step size 4 × 5 nm. Photon energy is 1296 eV. Scale bars correspond to horizontal 100 nm and vertical 120 nm. The figure is adapted from Sanli *et al*.[33]

Table 4.3 Comparison of measured, expected, and ideal diffraction efficiencies at various X-ray energies. The calculations are done using CWT. The ideal DE is the DE for an FZP of ideal design and neglects any Pt–Ga–C spill-over deposition during beamstop deposition. The X-ray absorptive effect of spill-over Pt–Ga–C deposition of thickness 115 nm on FZP zones is included for expected DE values. The theoretical efficiencies increase after the absorption edge. The table is adapted from Sanli *et al*.[33]

Energy (keV)	Measured DE (%)	Expected DE (%)	Ideal DE (%)
1.4	1.5	2.8	7.4
1.5	1.9	2.4	7.1
1.6‡‡‡‡	0.2	0.7	1.9
9.0	Not measured	26.4	26.9
14.4	Not measured	31.0	31.6

The thickness of parasitic Pt–Ga–C layer on the zones was estimated in a separate study to be 115 nm (see Appendix B). In Table 4.3, the effect of parasitic Pt–Ga–C deposition on diffraction efficiency is included in a separate column named as "expected DE". The atomic percentages of Pt, Ga, and C of FIBID were taken from the values stated in the literature.[115] The density of the Pt–Ga–C was estimated to be 12.34 g/cm^3 from the weighted mean mass density of the elements. The CWT calculations were done for the outermost period locally. Interdiffusion and roughness were neglected in accordance with the HRTEM, TEM-EDX, and EELS results. For the calculation, the following parameters were considered: Outermost zone width Δr = 25 nm, densities of ρ = 8.9 g/cm^3 and ρ = 3.0 g/cm^3 and line to space ratio of 1:2 for HfO_2 and Al_2O_3 thin films, respectively. To be able to compare measured and expected diffraction efficiencies a constant optical thickness of 700 nm was considered for the calculation of expected diffraction efficiencies in the soft X-ray range. The expected performance of the optic in hard X-rays is included in Table 4.3 for 9.0 and 14.4 keV X-rays. Ideal optical thicknesses were considered for calculating the diffraction efficiencies at the same energies.

‡‡‡‡ The sudden decrease in the diffraction efficiency at 1.6 keV is related to the Al-K edge.

4.4. Tilted Multilayer FZPs

FZPs with zones that are parallel to the optical axis come with extreme penalties to the diffraction efficiencies at small Δr due to volume diffraction effects (see Chapter 1.5).[28,32,116] The decrease in diffraction efficiency as a function of Δr for an Al_2O_3-SiO_2 ML-FZP at its optimum optical thickness is calculated by CWT and is depicted in Figure 4.12 This phenomenon negates one of the main advantages of fabricating FZPs via thin film deposition techniques, namely the possibility to deposit extremely fine outermost zones for high-resolution optics. Consequently, the achieved imaging resolutions via conventional XRM using FZPs have converged to about 7 nm in half-pitch.

In this section FZPs having tilted zones for surpassing this limit will be discussed, theoretical calculations will be presented, and a new fabrication strategy will be demonstrated that enables ML-FZP with precisely tilted zones. Finally, direct imaging experiments at a scanning transmission microscope using the tilted ML-FZPs will be presented and discussed.

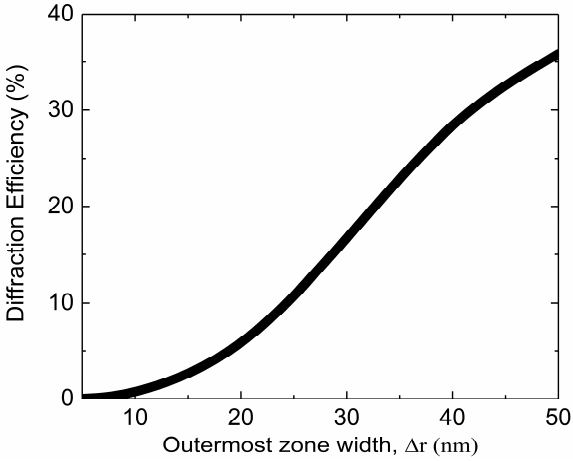

Figure 4.12 The decrease in diffraction efficiency for small Δr. The diffraction efficiency is calculated by CWT for an Al_2O_3-SiO_2 ML-FZP at the optimum optical thickness with parallel zones for 14.4 keV X-rays. The diffraction efficiency decreases significantly for smaller outermost zone widths.

4.4.1. Design, Fabrication, and Characterization

The nanofabrication of high quality three dimensional and tilted or wedged zone plates are extremely difficult, which leads to various strategies for approximations. Proposed strategies are stacking of binary FZPs to create tilted zones,[88] making tilted multilayer Laue lens pairs,[72-74,117,118] and multilayer zone plates deposited on drawn tapered fibers.[99,119] Stacking FZPs for creating tilted zones is interesting but requires several subsequent lithography steps. Tilted MLLs have recently drawn immense interest but having monolithic optics is more desirable as it decreases the complexity of the imaging setup. Depositing on drawn fibers often raises questions about the accuracy of the tilt angle, diameter, and roundness of the core, which is troublesome to identify. Here, a new fabrication concept is proposed and demonstrated, based on the improvements in the focused ion beam technology, resolving the issues mentioned above.

Overview

The fabrication of tilted ML-FZPs is accomplished in three steps (see Figure 4.13). First, a FIB is used to micro-fabricate tapered pillars with controlled slanting angles on single crystalline substrates. Then multilayer zones of the FZP are deposited on the substrate using ALD. Finally, a tilted ML-FZP is cut from the deposit using the FIB lift-out method.

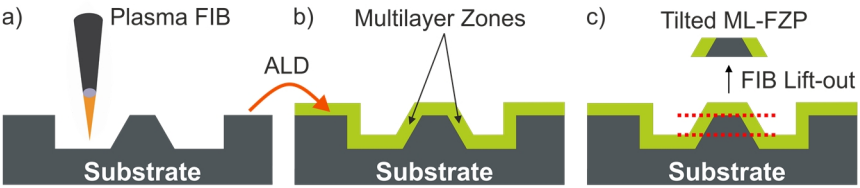

Figure 4.13 The fabrication steps of tilted ML-FZPs is illustrated. a) A tapered micropillar is fabricated by Plasma FIB milling. b) Multilayer zones of the FZP are deposited on the micropillars using ALD. c) Tilted ML-FZPs can be cut from the deposited pillars using a FIB. The figure is adapted from Sanli *et al*.[33]

Design of the ML-FZPs

The zones of the ML-FZP are selected to be Al_2O_3-SiO_2. There are several reasons for choosing the Al_2O_3-SiO_2 material couple. First, high-quality ALD of Al_2O_3-SiO_2 multilayers were achieved, with low roughness with a relatively high deposition rate. The deposition rate is critical as the intended deposition thickness is 4 µm, a huge thickness regarding ALD. Second, Al_2O_3 and SiO_2 have relatively small absorption combined with a similar phase shift. Therefore, the optimum FZP thickness is reasonably high for soft X-ray focusing. The FIB lift-out of very thin ML-FZPs is extremely challenging and not desired.[90] Moreover, the theoretical diffraction efficiencies are very high, especially in the hard X-ray regime.

The change in diffraction efficiency for parallel and tilted zones as a function of outermost zone width, Δr is shown in Figure 4.14a for 1 keV X-rays, and Figure 4.14c for 14.4 keV X-rays.

The diffraction efficiencies at different tilt angles for a selected ML-FZP of 20 nm outermost zone width is shown in Figure 4.14b for 1 keV X-rays and Figure 4.14d for 14.4 keV X-rays. The calculations show that although the diffraction efficiencies reach a maximum for the Bragg angle, significant diffraction efficiency gains are possible with a non-perfect tilting angle. This is important because, with the suggested fabrication method, it is not possible to bring each zone to the local Bragg angle as it changes slightly for every zone as each has a slightly different thickness.

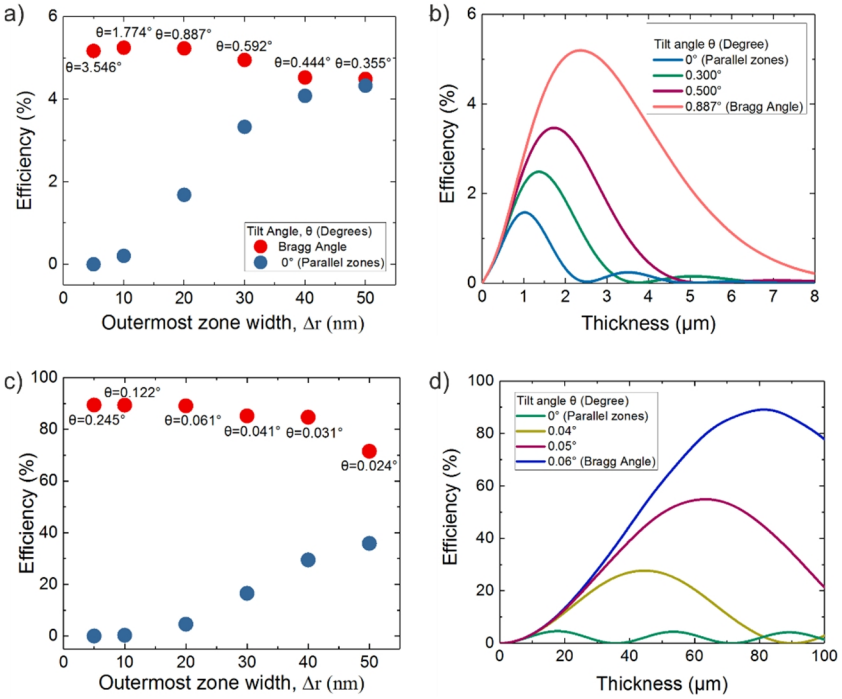

Figure 4.14 a) Calculated diffraction efficiencies of ML-FZPs at their optimum optical thickness having parallel and tilted zones as a function of outermost zone width, Δr for 1 keV X-rays. The efficiencies are calculated according to RCWT locally (considering only the outermost period and not integrated to the FZP area). b) The calculated diffraction efficiency of an Al_2O_3-SiO_2 ML-FZP of Δr = 20 nm for 1 keV X-rays as a function of the tilt angle, θ. The efficiencies are calculated according to RCWT locally (considering only the outermost period and not integrated to the FZP area). c) Calculated diffraction efficiencies of ML-FZPs at their optimum optical thickness having parallel and tilted zones as a function of outermost zone width, Δr for 14.4 keV X-rays. The efficiencies are calculated according to RCWT. d) The calculated diffraction efficiency of an Al_2O_3-SiO_2 ML-FZP of Δr = 20 nm for 14.4 keV X-rays as a function of the tilt angle, θ. The efficiencies are calculated according to RCWT. The figure is adapted from Sanli *et al.*[33]

4.4.2. Tapered Micropillar Fabrication

The first optimization for tapered micropillars was done using the in-house Ga^+ FIB instrument (see Figure 4.15). To fabricate micro-pillars, annuli with varying inner and outer diameters were selected as patterning area. It has been found out that single-pass

patterning strategy delivers a deep micro-pillar but owing to resputtering effects, the required quality was not reached (see Figure 4.15a). A multi-pass strategy with varying inner and outer diameters delivered high quality tapered micro-pillars (see Figure 4.15b). A pillar was patterned on the edge of a Si wafer for easier lift-out and easier SEM imaging for quality control (see Figure 4.15c). Finally, the fabrication time was improved four-fold by using an Au (111) substrate (Figure 4.15d).

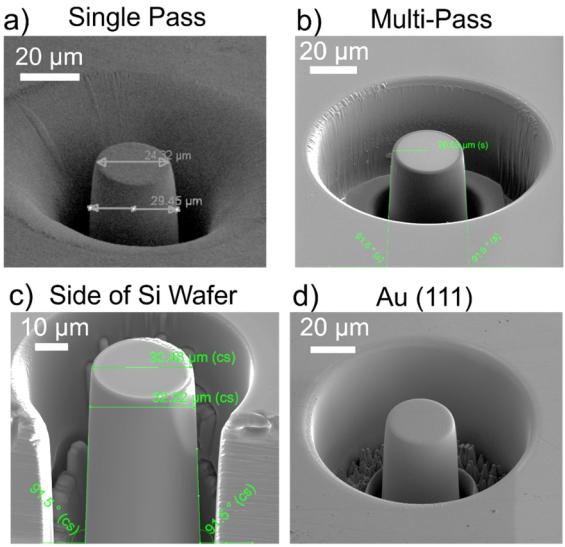

Figure 4.15 SEM images showing the progress of the in-house made tapered FIB pillars. a) Pillar milled using a single pass strategy resulted in sub-optimum quality. b) High-quality pillar fabricated on c-Si using a multi-pass strategy. c) A pillar was fabricated using multi-pass strategy on the edge of a Si wafer, reducing the fabrication time and making the lift-out easier. Moreover, giving an easy imaging angle. d) Micropillar fabricated on Au(111) requiring 4 times less patterning time due to higher sputter yield.

Twenty-six optimization trials were made using a different number of passes and different area selections. The highest quality was achieved using a 4 step milling with the following parameters listed in Table 4.4. Owing to the large milling volumes, the

fabrication of a single micropillar took approximately 24 hours on Si wafer and approximately 6 hours on Au (111) substrate.

Table 4.4 Ga^+ Ion beam patterning parameters delivering high quality tapered micro-pillars.

	Step 1	Step 2	Step 3	Step 4
Beam Current		20 nA (Maximum)		
Accelerating Voltage		30 keV (Maximum)		
Outer Diameter of the Annulus	70 µm	50 µm	43 µm	43 µm
Inner Diameter of the Annulus	37 µm	36 µm	35 µm	35 µm
Depth	30 µm	7 µm	5 µm	5 µm

Fabrication of Pillars using Plasma FIB

To improve the fabrication speed and to have a large array of pillars with varying properties, tapered micropillars were fabricated from single crystalline substrates of Si(100) and Au(111) (purity 99.999% from MaTecK Material-Technologie and Kristalle GmbH) by using a ThermoScientific Helios Plasma FIB[§§§§]. iFast recipes were created for controlling the pillar milling processes automatically. To fabricate pillars with reasonable throughput, a high PFIB beam current of 1.3 µA is selected for the rough milling step. To achieve a lower taper angle of the pillars, multiple concentric angular milling ring patterns were generated by iFast recipe with outer and inner diameters dynamically reducing in a pre-defined step size during the pillar fabrication. Dynamic reducing of the milling reduces the necessary milling time and minimizes the re-sputtering effects and ensures a smooth sidewall. An example of the area selection in dynamic reducing of the milling is shown in Figure 4.16.

Different PFIB parameters are used to fabricate pillars with different tilt angles. Four pillars having tilt angles of 9°, 5°, 1°, and 0.8° are fabricated on Si(100) (see Figure 4.17a-d). Furthermore, two arrays of each having 25 micropillars with tilt angles of 1° and 0.8° are fabricated (see Figure 4.17e,f).

[§§§§] The PFIB micropillars were fabricated by Dr. Chengge Jiao.

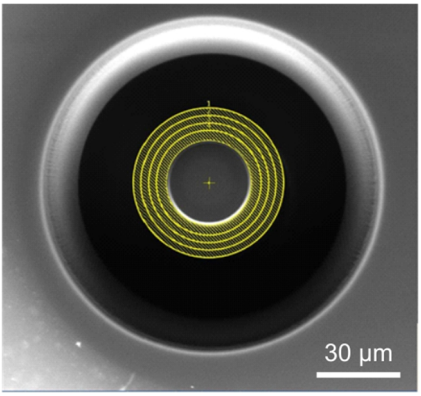

Figure 4.16. Dynamic reducing of milling diameter. Four ring-shaped areas are selected with different inner and outer diameters. The redeposited material is removed by a subsequent milling step. Courtesy of Dr. Chengge Jiao.

The standard deviation in the tilt angle for a 5 × 5 array is measured to be less than 0.1°. A secondary optimization is performed on Au (111) pillars. the use of Au (111) as the substrate has several advantages. First, the ion beam sputter yield of Au (111) is about four times higher than that of Si (100). This makes the fabrication of pillars effectively four times faster. Moreover, using Au as the central obstruction makes the need for depositing a beamstop using FIBID obsolete, hence avoids the complications related to parasitic Pt deposition which was discussed in the first part of this chapter.

An array of 0.8° tilted micropillars on Au (111) is shown in Figure 4.18a. A higher magnification image depicted in Figure 4.18b proves the quality of individual micropillars. Pillar fabrication parameters for Si (100) and Au (111) substrates are summarized in Table 4.5.

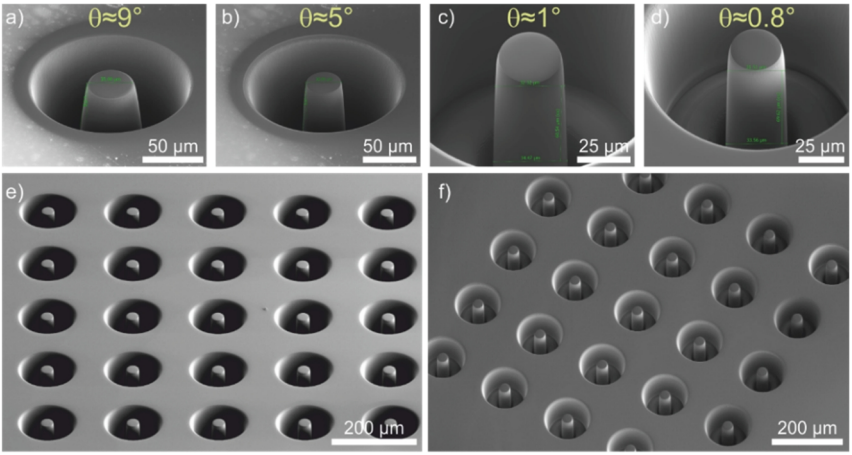

Figure 4.17: SEM (secondary electron) images of tilted micropillars fabricated on Si (100) substrate via PFIB with various tilt angles. a) θ ≈ 9°, b) θ ≈ 5°, c) θ ≈ 1°, d) θ ≈ 0.8°, e) an array of θ ≈ 1°, tapered micropillars, f) an array of θ ≈ 0.8°, tapered micropillars. The structures are prepared by Dr. Chengge Jiao. The figure is taken from Sanli *et al*.[33]

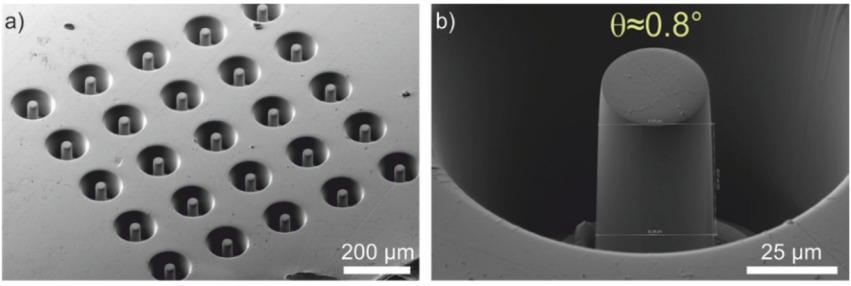

Figure 4.18 SEM (secondary electron) images of tilted micropillars fabricated on Au (111) substrate via PFIB with a tilt angle of θ ≈ 0.8°. a) an overview image of the array of micropillars, b) a higher magnification SEM image confirming the quality of the fabricated micropillars. The structures are prepared by Dr. Chengge Jiao. The figure is adapted from Sanli *et al*.[33]

Table 4.5 Pillar fabrication parameters for Si (100) and Au (111) substrates for various tilt angles. In the marked steps, the diameter of the milling area was reduced dynamically with a defined step size. The parameters are provided by Dr. Chengge Jiao. The table is adapted from Sanli *et al*.[33]

	Step 1	Step 2	Step 3	Tilt Angle	Time (min)
Si (100)	1.3 µA	n/a	n/a	9°	32
Si (100)	1.3 µA	480 nA	n/a	5°	38
Si (100)	1.3 µA	59 nA*, 6 µm step-size for outer ring reducing	n/a	1°	50
Si (100)	1.3 µA	59 nA*, 2 µm step-size for outer ring reducing	n/a	0.85°	60
Au (111)	1.3 µA	180 nA*, 2 µm step-size for outer ring reducing. 85% beam overlap.	n/a	1°	20
Au (111)	1.3 µA	59 nA*, 2 µm step-size for outer ring reducing. 90% beam overlap.	15 nA*, 1.5 µm step-size for outer ring reducing	0.8°	29

ALD and FIB Liftout

Micropillar arrays fabricated on Au (111) orientation was used as the core during the FZP fabrication. An Alumina/Silica multilayer structure following the FZP law with an outermost zone width of 20 nm was deposited using ALD with the parameters listed in Table 4.6. In Figure 4.19, the plan-view lift-out process of the ML-FZP with tilted zones is depicted. The tilted ML-FZP is transferred on a TEM sample holder as described before and flipped 90° prior to the final polishing step. After the final polishing, the ML-FZP with tilted zones is shown ready for use (Figure 4.19d).

Table 4.6 List of ALD parameters for Al_2O_3-SiO_2 zones for the tilted ML-FZP fabrication. The table is adapted from Sanli *et al*.[33]

	Precursor	N_2 flow (sccm)	t_{Pulse} (ms)	t_{Purge} (ms)	Pressure (Pa)
Al_2O_3	TMA	80	20	1980	6.3
	H_2O	80	20	1980	
SiO_2	BDEAS	40	140	1860	20
	O_2 plasma	200	1000	1000	

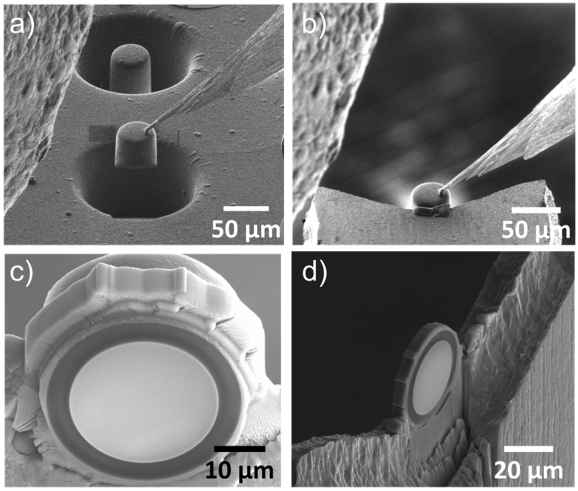

Figure 4.19 a) The deposited tapered pillar is cut using FIB and lifted our using the microneedle. b) the pillar is mounted on the TEM lift-out grid. c) the slice is secured on the TEM grid using Pt^+ deposition. d) The slice is thinned down to the optimum thickness and is ready for use. The figure is adapted from Sanli *et al*.[33]

4.4.3. Results and Discussion of Tilted ML-FZPs

The performance of a tilted ML-FZP was also tested at the MAXYMUS beamline. The measured diffraction efficiency of the tilted ML-FZP achieved 11 % of the theoretically expected value in an X-ray energy range between 800–1450 eV (Figure 4.20a), and it is in good qualitative agreement with the theory. The quantitative discrepancy of the diffraction efficiency may be attributed to errors in assumed thin-film densities. An overall

(Figure 4.20b) and close up (Figure 4.20c) image of the SS test sample shows that 30 nm structures were clearly resolved. This very first successful imaging experiments promise higher efficiencies and resolutions through process optimization in the near future.

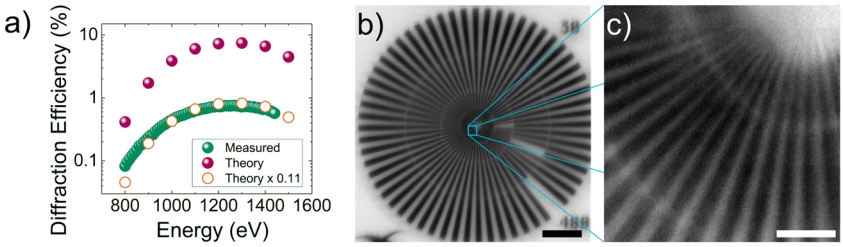

Figure 4.20 a) Measured (green spheres) vs. theoretical diffraction efficiencies (purple spheres and orange circles) for the tilted ML-FZPs. The theoretical calculations were done according to RCWT. The difference in the thickness of each period was taken into account (non-local, integrated). b) STXM image of the SS test sample. Energy is 1175 eV. Step size is 20 nm. Scale bar is 5 µm. c) STXM image of a quarter of the inner rings of the SS test sample. Energy is 1175 eV. Step size is 10 nm. Scale bar is 500 nm. The figure is adapted from Sanli *et al.*[33]

4.5. Summary and Conclusions

The resolution and efficiency of the X-ray optics are generally limited by the capabilities of the nanofabrication methods, where the most widely utilized nanofabrication method for diffractive X-ray optics is the e-beam lithography. The e-beam lithography processes are limited fundamentally by the scattering of electrons within the resins. Moving towards larger acceleration voltages (higher energy electrons) can improve the resolution down to sub 5 nm lines and spaces. However, because the FZPs have to be optically thick, the smallest outermost zone widths have been in the order of ten nanometers. This is due to the high aspect ratio requirements to induce the required phase shift within the lens.

An idea that was presented to go beyond the resolution and aspect ratio limitations of the lithographic processes was the so-called “sputtered-sliced” zone plates. Over the last 40 years since the inception of the idea, these optics did not show a significant

promise. In the meantime, atomic layer deposition and focused ion beam technologies have been maturing into the mainstream.

First-ever ALD-FZPs were developed in our department in collaboration with dedicated ALD groups leading to the demonstration of a half-pitch resolution of 40 nm.[96,120] Over time, the improvements and fine-tunings made in the nano-structuring and the characterization methods let us prove the real potential of such optics by resolving half-pitch structures down to 21 nm.[58,121] In 2014, when our group bought an ALD instrument for the first time, I was tasked with developing more efficient and higher resolution ML-FZPs.

Here, in Chapter 4, I show the optimization and development of several ALD thin film processes to be used as the zones of ML-FZPs. For the materials selection, coupled wave theory simulations of ML-FZPs with different material combinations were done. Then, I performed in-situ and ex-situ ellipsometry measurements to optimize the homogeneity and growth per cycle of the thin-films, which were used to calculate the number of cycles for depositing each ML-FZP layer following the zone plate law. The deposition process, which often takes a week is the most critical part of the whole process. The slicing process at the FIB was also optimized and finally using the fabricated FZPs a 15 nm half-pitch resolution was demonstrated, a significant improvement over competing fabrication methods, as well as our previous results.

A significant competitor to the ML-FZPs is the tilted Multilayer Laue Lenses (MLL) developed, simulated, deposited and assembled by several dedicated groups in Argonne and Brookhaven National Laboratories as well as Fraunhofer Institutes in Dresden. So far, the attempts to develop comparable circular ML-FZPs with tilted zones did not show promising imaging results. In this chapter, I also present a new method to fabricate ML-FZPs with precisely tilted zones by using FIB machined tilted micro-pillars as substrates. I developed the tilted micro-pillars for the first time using our in-house Ga^+ FIB. Then large scale micro-pillar arrays were developed in collaboration with FEI using a Xe^+ focused ion beam machine. The Au pillars serve as both substrate and beam-

stop, rendering the deposition of an extra beamstop obsolete. This removes a significant hurdle that has been hindering the ML-FZPs to achieve the efficiencies promised by CWT calculations. A first-ever imaging result has been shown using these optics paving the way for future developments in the field.

5. 3D Printed Kinoform FZPs

The work presented in this chapter has been partly published in
Sanli, Umut T., *et al*. "3D Nanoprinted Plastic kinoform X-Ray Optics." *Advanced Materials* 30.36 (2018): 1802503. The copyright for the article is held by the authors, and this is an open-access article under the terms of the Creative Commons Attribution Non-Commercial License. The manuscript text is written by Umut T. Sanli.

The 2PP structures were fabricated together with and under the supervision of Dr. Hakan Ceylan. Ptychography experiments were done by Dr. Kahraman Keskinbora. The MATLAB code for STL file generation is provided by Dr. Kahraman Keskinbora. The MATLAB code for diffraction efficiency calculations using thin grating approximation was developed by Dr. Nicolas Teeny and Dr. Kahraman Keskinbora.

5.1. Introduction

In the present chapter, 3D direct laser writing for realizing ultra-high diffraction efficiency (DE) kinoform type plastic zone plates with medium resolution will be presented, which are of great interest particularly for ptychographic imaging experiments or at the relatively lower brilliance laboratory-scale X-ray sources. It will be experimentally shown that using an efficient kinoform type optic with a micron size focus and using ptychography, very high resolutions can be achieved, with high image scanning speeds.

It has been discussed in Chapter 1.5.1 that the kinoform lenses have theoretical diffraction efficiencies of up to 100 %. Owing to the high efficiencies, the kinoform type zone plates have been much desired as X-ray optics. However, due to challenges in the nano-fabrication of optically smooth continuous surface profiles, kinoform FZPs have been largely unavailable. Instead, staircase approximations have been developed.[86,122-124] Only, very recently a gray-scale ion beam lithography was used to realize kinoform zone plates without approximations.[125] However, the kinoforms fabricated using gray-scale IBL technique cannot achieve high aspect ratios, due to redeposition effects.

The performance of some of the notable kinoform approximations and the grayscale IBL kinoform are compared in Table 5.1.

Table 5.1 A comparison of the outermost period, achieved focus size, expected FWHM, and efficiency of the present work with approximated kinoform structures from the literature.

Work	Optic type	Achieved focus size FWHM	Outermost period	Efficiency
Di Fabrizio *et al.*[86] (1999)	Multi-level FZP – 4 steps	1.028 µm	2 µm	55% at 7 keV
Takeuchi *et al.*[124] (2012)	Multi-level FZP – 3 steps	0.630 µm	1.2 µm	39% at 9.85 keV 33% at 16 keV
Mohacsi *et al.*[85](2014)	Multilevel and Stacked FZP. 6 level	200 nm	400 nm	53.7 % at 6.5 keV (68.5% of Theoric. DE.)
Keskinbora *et al.*[125] (2015)	True parabolic kinoform	60 half-pitch imaging resolution	200 nm	3 % at 1200 eV (17% of Theoric. DE.)
Keskinbora *et al.*[125] (2015)	True parabolic kinoform	NA	800 nm	4.7 % at 1100 eV (89 % of Theoric. DE.)
Mohacsi *et al.*[84](2016)	Zone doubled, Stacked on membrane, Double-sided	200 nm	400 nm	54.7 % at 6.2 keV (78 % of Theoric. DE.)
Present Work [30](2018)	True parabolic kinoform	FWHM = 488 nm 240 nm half-pitch image resolution	800 nm	20 % at 1200 eV (95 % of Theoric. DE.)

5.1.1. X-ray Optical Properties of Polymers used for 3D printing

One important material property for kinoform zone plates[126] as well as refractive lenses is the δ (refraction) to β (absorption) ratio, which is previously discussed in Chapter 1.2.1. The δ and β values for common X-ray optical materials are depicted and compared to the commercial photoresist used in this study, IPL-780 (Nanoscribe GmbH, Germany) in Figure 5.1. The IPL-780 has a δ to β ratio much higher than Au and very similar

to Diamond which is considered to be one of the best X-ray optical material, estimated from its chemical composition (see Appendix G for chemical composition estimation).

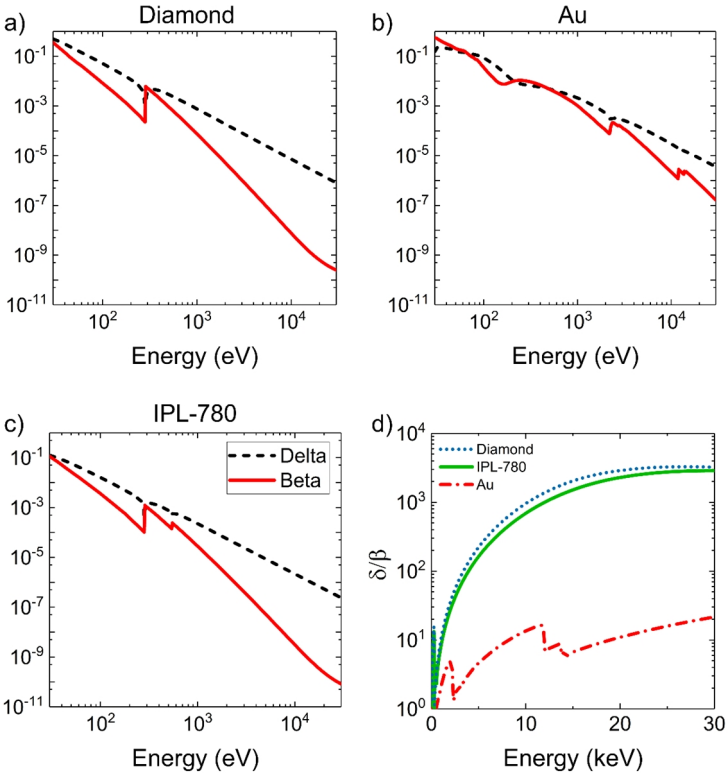

Figure 5.1 Delta and beta values for IPL-780 compared with common X-ray optical materials. a) for Diamond of density, d= 3.50 g/cm^3 b) for Au of density, d = 19.32 g/cm^3 c) for IPL-780 of density, d = 1.50 g/cm^3, d) comparison of δ/β ratios. Data are acquired from Henke et al.[12]

Another important material property is the microstructure. A homogeneous microstructure without inclusions or voids minimizes undesired scattering effects. In certain cases, particularly for stacked kinoforms and stacked nano-focusing lenses working in the hard X-ray regime, crystallinity is also not desired due to the Bragg diffraction.[127] Hence, an amorphous microstructure is the most desired (as also discussed in Chapter

4). X-ray diffraction (XRD) analysis confirmed that the microstructure of the 3D printed structures using IPL-780 is fully amorphous (see Figure 5.2).

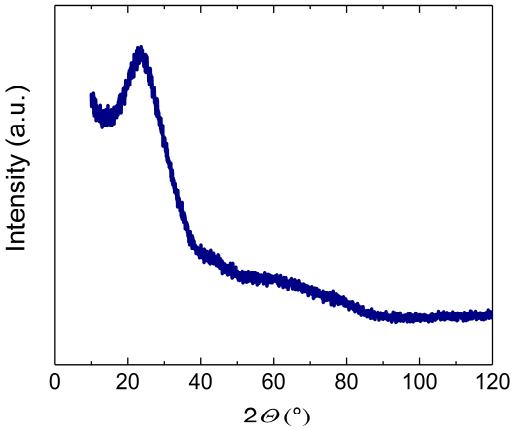

Figure 5.2 Grazing incidence XRD results of polymerized structures using IPL-780. The figure is adapted from Sanli *et al.*[30]

Moreover, the use of 3D printing allows X-ray optics to be fabricated in very short times, in the order of a minute, orders of magnitude faster than competing methods. 3D printing allows kinoform zone plates to be directly written on X-ray transparent surfaces, with extremely high yield. Compared to multi-step processes involving e-beam lithography and stacking to achieve staircase approximations, 3D printing offers an elegant solution to achieve true 3D kinoform profiles. With the proliferation of 3D commercially available nanoprinting instruments, the cost of high-efficiency FZPs will be reduced and much more available for the users of the synchrotron sources as well as in laboratory-scale sources. The ease of fabrication and cost-effectiveness would also benefit experiments in the emerging XFEL sources where the focusing optics have to be replaced after a few laser pulses due to the damages caused by the extremely high incident intensity.

Eq. 2.3 tells us that for the ultimate resolution in CDI techniques will be achieved by using the brightest source, combined with an optic with the highest resolution and

the highest DE. Although theoretically, using the highest resolution optic yields the highest ptychographic resolution in a dose-limited set-up, a high-resolution FZP is not practical in most of the ptychography experiments which are discussed in detail in Chapter 2.5. In addition to the discussion in Chapter 2.5, high-resolution FZPs are in general not as efficient as the low-resolution FZPs, which would reduce the flux in the focal plane. The NA of the optic should be selected for the desired resolution and field of view. A high DE, however, remains essential for achieving better reconstructions and higher resolutions.

Thanks to the superior X-ray optical properties of the IPL-780 photoresist, 3D printed kinoform lenses offer very high diffraction efficiencies. Theoretical DE of 3D printed kinoform lenses are calculated using the thin grating approximation as a function of X-ray energy and optical thickness and is depicted in Figure 5.3.

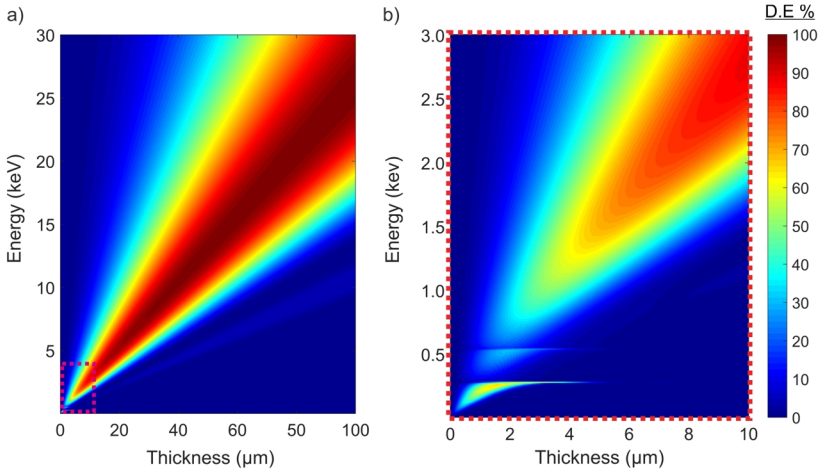

Figure 5.3 Theoretical DE of kinoform zone plates as a function of X-ray energy and optical thickness. a) for X-rays with energy up to 30 keV, b) for soft X-rays. The figure is adapted from Sanli *et al*.[30]

5.2. Design and Fabrication of Kinoform FZPs

In 2PP, computer-controlled trajectories, generated using computer-aided design (CAD), are used to polymerize a photosensitive material to the desired structure. The laser deflection is controlled using a galvo-mirror system which also allows a fast and precise printing. The structures are printed layer by layer by moving the stage in the Z-direction using a piezo stage for high accuracy. The printing scheme is illustrated in Figure 5.4.

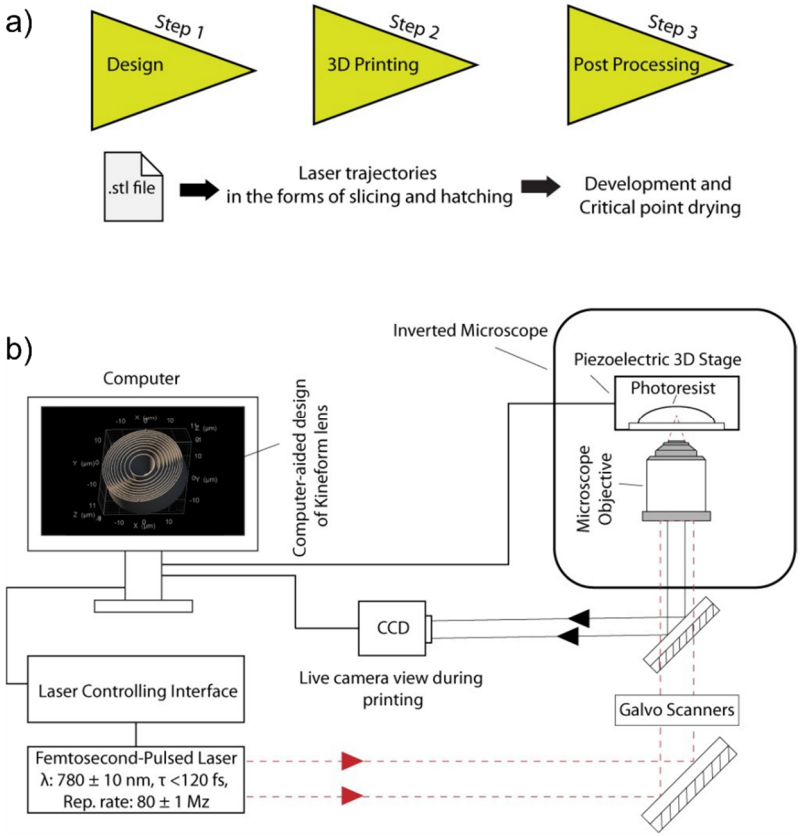

Figure 5.4 3D-printed plastic X-ray optics with two-photon polymerization using Photonic Professional GT (Nanoscribe GmbH). a) 3D printing procedure of the lenses consist of three main steps.

Computer-aided design file of the optics is converted to computer-controlled laser scanning trajectories in the form of hatches and slices. A post-development and critical point drying steps ensure the removal of non-polymerized photoresist and high-quality preservation of structural features of the lenses. b) Schematic illustration of the computer-controlled printing of the X-ray optics. The system contains a piezo stage mounted on an inverted microscope. Computer-controlled raster scanning is accomplished using Galvo scanners for hatching in the xy-plane. Slices in the z-axis are accomplished using the piezoelectric stage. In this configuration, Galvo scanners enable moving-beam-fixed-sample approach, and hence dramatically increases the printing speed on the order of tens of mm/s. The figure is taken from Sanli *et al*.[30]

5.2.1. Generation of the CAD file

The kinoform lenses were generated (by Dr. Kahraman Keskinbora) using the computing system Wolfram Mathematica (Wolfram Research Inc.). To be compatible with the commercial femtosecond two-photon laser lithography system (Photonic Professional GT, Nanoscribe GmbH, Germany) the computer-generated designs were exported in stereolithography (STL) file format. The STL files are sliced and hatched using the DeScribe 2.5 software of Nanoscribe GmbH and are converted to General Writing Language (GWL) scripts for feeding to the Photonic Professional GT instrument. The GWL file contains the laser trajectories and all the system parameters that will be used during the writing process. The hatched and sliced file is shown in the Figure below. Hatching and slicing distances are chosen as 100 nm for achieving high precision structures.

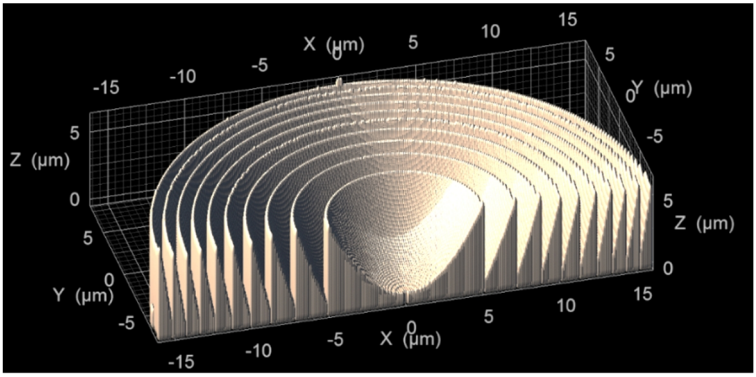

Figure 5.5 CAD file that is fed to the PPGT system.

5.2.2. Printing of the Kinoform Lenses

The kinoform lenses were printed on commercially available X-ray transparent Si_3N_4 membranes of thickness 100 nm, which are present on Si frames with dimensions 5 mm x 5 mm x 100 µm (Silson Ltd, England). A 100 µm frame thickness was selected to accommodate the short focal length of the objective optical element. An immersion oil of high refractive index was filled between the membrane and the glass substrate to match the refractive index of the substrate to retain high refraction and to minimize spherical aberration. About 3 µL of IP-L 780 photoresist (Nanoscribe GmbH, Germany) was placed on the membrane using an adjustable pipette dropper. Two-photon polymerization (2PP) of the kinoform design was done using the Photonic Professional GT instrument[*****]. Multiple lenses with varying laser power, scan speed, and contour are printed to optimize the printing parameters (see Table 5.2). The printed lenses were developed using propylene glycol monomethyl ether acetate (Merck KGaA, Germany) and isopropanol. After the development, the kinoform lenses were dried using super-critical-point drying to eliminate zone collapsing due to the capillary effect.

Table 5.2 Overview of the laser power and scan speed parameters used for 3D printing.

Optical thickness	Laser Power	Scan Speed (mm/s)	Contour Number	Dosage (µJ/µm)
2 µm	32 mW	26	3	1.23
2 µm	32 mW	25	3	1.28
2 µm	33 mW	25	3	1.32
2 µm	33 mW	23	3	1.43
4 µm	24 mW	15	2	1.60
4 µm	28 mW	15	2	1.87
4 µm	28 mW	15	2	1.87
6 µm	26 mW	15	2	1.73
6 µm	26 mW	15	2	1.73

Printing time for each lens was less than one minute, which is several orders of magnitude faster than alternative kinoform fabrication methods and other top-down

[*****] The 2PP of the structures were performed by Dr. Hakan Ceylan.

methods (detailed in Chapter 5.3.1). SEM images of the 3D-printed lenses exhibit precise replication of the design geometry (Figure 5.6 a,b). The kinoforms were designed to achieve a diameter of 32 µm and an outermost zone period of 800 nm (Δr = 400 nm) and optical thicknesses from 2 to 6 µm leading to aspect-ratios of up to 7.5. SEM images of a 5 µm thick kinoform zone plate are shown in Figure 5.6c and d.

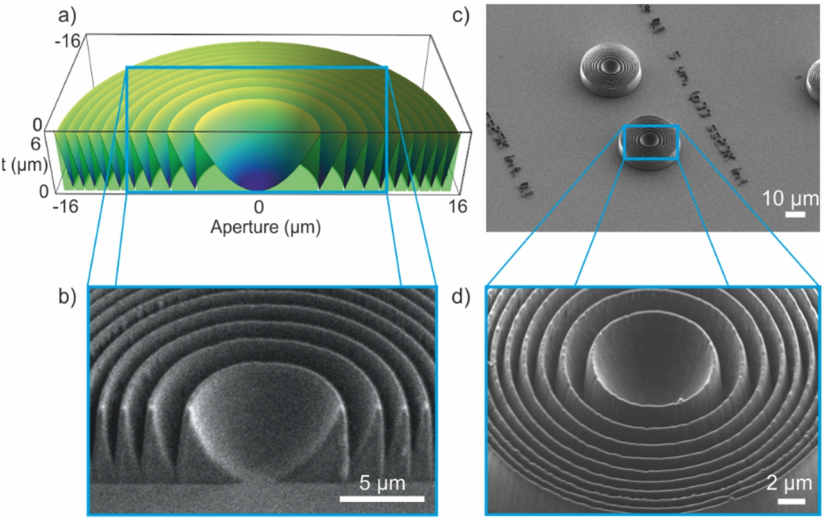

Figure 5.6 Comparison of the CAD file and final structure. a) The MATLAB generated CAD file of the kinoform lens hiding half of the structure to have a better illustration of the zone profile. b) An SEM image of a nano-printed half-kinoform lens shows the cross-section profile for comparison with the CAD. c) A low magnification SEM image showing two kinoform lenses printed next to each other on Si3N4 membrane using different parameters. d) A high magnification image of the area denoted with a blue rectangle in (c), showing excellent surface quality. Details of SEM imaging is given in Appendix G. Figure is adapted from Sanli *et al*.[30]

The effect of contours

To have a smoother surface finish, contour layers were added to the GWL file. The contour is an additional scan, scanning only the shell of the 3D file. The hatching distance, laser power, and laser speed of the contour were selected to be the same as the solid fill. The surface smoothing effect of applying a contour layer is shown in Figure 5.7.

The contour helps to achieve a smoother surface. However, the increase in the effective dose should be considered to avoid overdose.

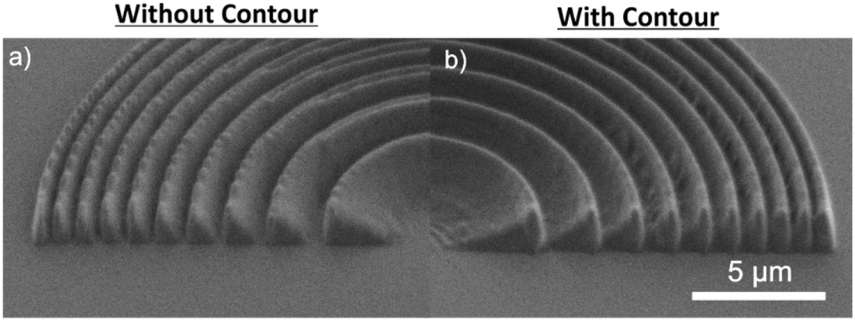

Figure 5.7 The effect of applying a contour layer to the GWL file. a) SEM image showing the cross-section of a half kinoform profile printed without contour and b) SEM image showing the cross-section of a half kinoform profile printed with contour. The roughness is lower when a contour layer is applied. However, the structures hint for overexposure of the structures.

5.3. Results and Discussion of 3D Printed Kinoform FZPs

The synchrotron tests were done at the MAXYMUS between 800–1800 eV using direct imaging and ptychography. Owing to the limited beamtime, direct imaging experiments were only done using two lenses with 2- and 4-µm optical thickness. A 240 nm half-pitch cut-off resolution was estimated *via* direct imaging of the BAM-L200 test sample using the 4-µm thick lens (see Figure 5.8a). The measured line profile (Figure 5.8b) was used to calculate the contrast transfer function (CTF) (Figure 5.8c), which is in agreement with the theoretical CTF of an unobstructed lens. The 2 µm thick kinoform lens was used to image the Siemens Star (SS), showing an astigmatism-free result (Figure 5.8d). Two sequential images with identical scanning parameters from the same region were captured and aligned to perform Fourier ring correlation (FRC) analysis (½ Bit threshold), which delivered a resolution of 558 nm (half-pitch of 279 nm, Figure 5.8e).

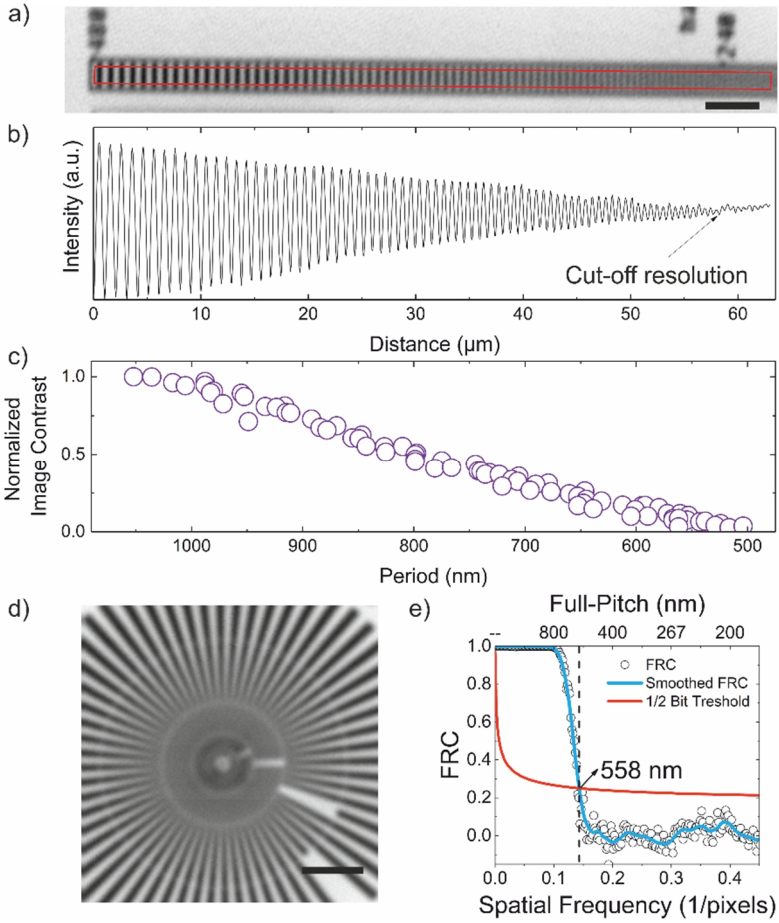

Figure 5.8 Results of the X-ray microscopy and focusing tests. a) STXM image of a linear test target recorded at 1200 eV in a line by line scan with a pixel dwell time of 2.8 ms and 80 nm step size, using a kinoform lens with 4 μm thickness and 800 nm outermost period (400 nm effective Δr). Scale bar 10 μm. The cutoff resolution is about 240 nm. b) The intensity profile of the linear test target integrated over 20 pixels, as outlined in the STXM image with the red rectangle. c) The graph shows the Michelson Contrast (I_{max}-I_{min}/I_{max}+I_{min}) normalized to the lowest frequency structures. CTF of the lens qualitatively resembles that of an ideal, unobstructed optic. d) An overview STXM image of the central portion of the SS test target, recorded using a 2 μm thick kinoform zone plate at 800 eV with a dwell time of 5 ms and 80 nm step size. Scale bar 5 μm. e) FRC calculated from two STXM images shows 558 nm full-pitch resolution. Details are given in Appendix G. Figure is adapted from Sanli *et al*.[30]

The amplitude and the phase images of the SS were reconstructed using ptychography (Figure 5.9a,b). The innermost 30 nm features of the SS were resolved using a reconstructed pixel size of 19 nm.

The reconstructed pixel size can potentially be reduced to < 5 nm by changing the camera distance, in this case, limited to 4 cm by the design of the experimental set-up (see Chapter 2.5 and Figure 2.16). However, as discussed in Chapter 2.5, this requires the removal of the piezo sample scanning stage, which induces other experimental limits such as the need for scanning the optic stage. For practical reasons and as the pixel size was more than enough[†††††] to reconstruct the probe function opted for the low-resolution ptychography setup.

The illumination function was reconstructed simultaneously, which is used to calculate the three-dimensional wavefield 1.8 mm along the optical axis (Figure 5.9c). The magnitude of the reconstructed probe at the object plane, which is defocused by 230 µm (Figure 5.9d), was propagated to the focal plane revealing an Airy pattern (Figure 5.9e), slightly larger than the expected pattern (Figure 5.9f). The results confirm that 3D printed kinoform zone plates can perform very well as focusing optics in ptychographic imaging.

Diffraction efficiencies of lenses with 2, 4 and 6 µm thicknesses were measured from 900 to 1800 eV (Figure 5.10a)using the pinhole scan method detailed in the Appendix A. A line profile of the intensity across the pinhole scan shows a clear suppression of the 0^{th} order, confirming the high quality of the optic (see Figure 5.10b). Measured efficiencies regularly exceeded 15 % in the full energy range peaking up to 20 % for a 2-µm thick kinoform at 1200 eV. The measured efficiency at 1500 eV corresponds to 95 % of the theoretical calculations at (Figure 5.10c). The deviation from the theoretical values at lower energies can be partly attributed to the high harmonic contributions from the undulator.

[†††††] According to the Shannon-Nyquist sampling theorem a pixel size of 200 would be enough to represent the probe function with an estimated 0-crossing of 1.22*400=488 nm. A pixel size of 20 nm represents a 10 times better image of the probe.

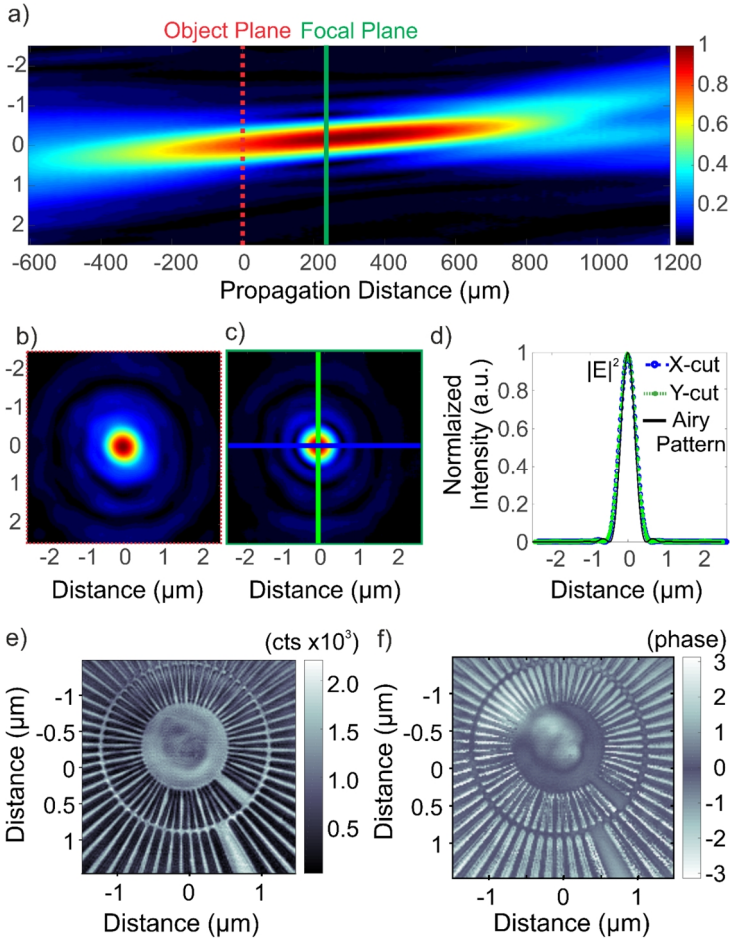

Figure 5.9 Results of the X-ray ptychography tests. a) YZ-slice of the normalized magnitude of the wavefield propagated from -600 till 1200 μm. Color-bar is valid for all density plots. b) Magnitude of the reconstructed illumination function at the object plane shows a defocused probe. c) Illumination function propagated to the focal plane. d) X- and Y-slices through the focal spot shows the Airy disc created by the kinoform lens. Slices in X- and Y-directions are shifted in to align with the perfect Airy disc. e) and f) the reconstructed magnitude of the SS test object obtained by ptychographic imaging and the corresponding reconstructed phase, respectively. Nominal period of the smallest features is 60 nm. Ptychographic imaging conducted by Dr. Keskinbora. The figure is adapted from Sanli *et al*.[30]

Another reason may be the increase of the volumetric mass density of the resin after cross-linking, which was not taken into account in the theoretical diffraction efficiency calculations. Multiple lenses were printed and tested using different laser parameters to study the effect of laser dose on DE. Four lenses with the same optical thickness (2 µm) were printed with a varying laser dose between 1.23 and 1.43 µJ µm^{-1} (see Table 5.2). The highest DE among 2-µm thick lenses was obtained for a laser dose of 1.28 µJ µm^{-1} (Figure 5.10a). It can be seen that the variation in the diffraction efficiency is reduced for lenses that were printed using the same laser parameters showing the reproducibility of the 3D printing technique.

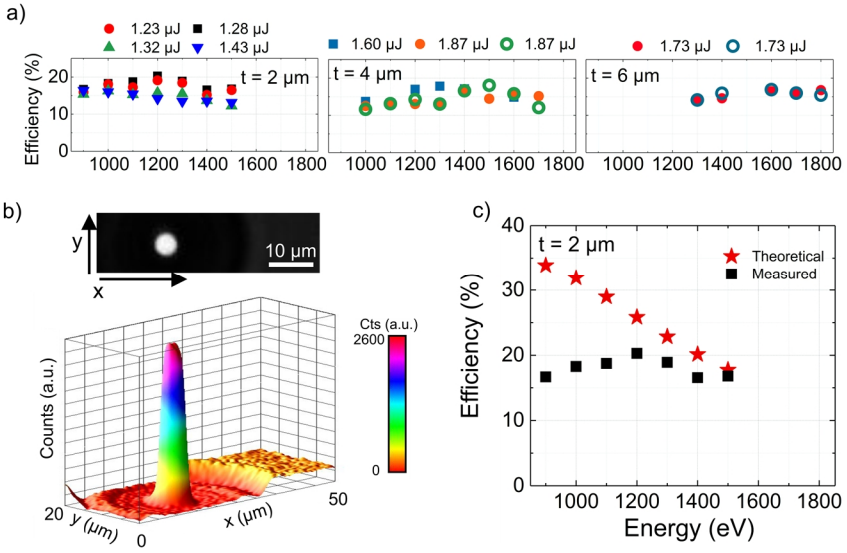

Figure 5.10 Diffraction efficiency performance of the 3D printed kinoforms. a) The measured diffraction efficiencies of kinoform lenses with optical thicknesses 2-(left graph), 4-(middle graph) and 6-µm (right graph). Four kinoform lenses with an optical thickness of 2-µm were evaluated. Each of those 2-µm thick kinoforms was printed using different printing dose as labeled in the figure legend. For testing the reproducibility of the fabrication method, two lenses with the same printing parameters were tested both for 4-µm and 6-µm optical thicknesses. b) top: A STXM image of a 4.4 µm wide pinhole taken without an OSA between the pinhole and the lens, showing the relation of the 1st order focus intensity to the 0th order and the incident intensity. Energy 1300 eV step size 500 nm dwell time 1 ms. Bottom: 3D surface profile of the image on top, showing that the 0th order

is completely suppressed c) 2 µm thick kinoform lens with highest DE (1.28 µJ/µm) compared to its theoretical DE. The figure is adapted from Sanli *et al*.[30]

Radiation resistance

The radiation resistance of ML-FZPs was discussed in the previous chapter. Owing to their strong bonding, the ceramic multilayers of the ML-FZPs are expected to show a high radiation resistance. However, polymeric lenses for focusing X-rays raises concerns regarding the radiation damage. During the synchrotron testing over several days, no degradation was observed in the imaging properties of lenses. To confirm the structural fidelity further, SEM imaging of the kinoforms were made, showing no structural damage on the lenses (Figure 5.11). However, the long-term stability of 3D printed lenses has not been tested.

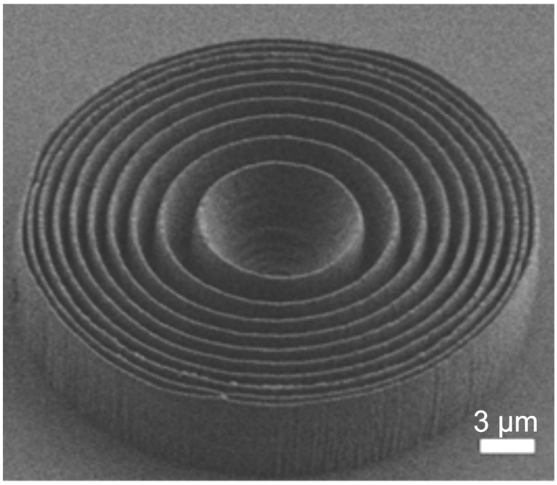

Figure 5.11 SEM image of a 3D printed kinoform lens after synchrotron tests. The figure is taken from Sanli *et al*.[30]

5.3.1. Patterning Time of 3D Nanoprinting Compared to IBL

3D nanoprinting allows the realization of kinoform zone plates with virtually unlimited aspect ratios while keeping the patterning times at least an order of magnitude shorter.

As previously discussed, the kinoform optics have an optimum optical thickness (for achieving the highest diffraction efficiencies) depending on the lens material and the X-ray energy. The optimum optical thickness increases for higher X-ray energies and for lens materials with lower atomic numbers.

Fabrication of kinoform optics in the optimum thickness using top-down fabrication methods is not realistic for higher energy X-rays due to the long patterning times as well as the required high aspect ratios.

In Figure 5.12, the patterning times are calculated for different optical thicknesses of the kinoform lenses, and their corresponding theoretical diffraction efficiencies are calculated accordingly. The 3D nanoprinting method is compared the ion beam lithography (IBL) for three different materials. Figure 5.12a shows calculations for an X-ray energy of 1 keV. In this soft X-ray regime, the optimum thicknesses can be achieved by both 3D nanoprinting and the IBL. The patterning time for IBL changes for different materials owing to different ion beam sputter yields of different materials. Au with 15.75 atoms/Ga^+ ions (under normal incidence for 30 keV ions, crystallinity effects disregarded) has the 5th highest sputter yield of the elements of the periodic table allowing for relatively fast milling.[61] Thanks to the chemical stability of Au, the gallium implantation into Au as a side effect of the IBL process does not pose any adverse effects.

The required optical thickness for a kinoform made out of Au is less, owing to the high electron density of Au. For these reasons, the patterning time for a Au kinoform at the optimum thickness should be about 10 minutes for soft X-rays at 1 keV. This is much faster than patterning other materials to desired optical thicknesses such as the previously published Si or Pd_8Si_2.[128] Nevertheless, 3D nanoprinting is still about an order of magnitude faster than the Au milling process using IBL.

Furthermore, the low X-ray absorption of the plastic material used in 3D nanoprinting offers theoretical diffraction efficiencies 4 to 5 times higher than that of Au made kinoforms. In the hard X-ray regime, 3D nanoprinting truly excels. In Figure 5.12b, the theoretical efficiencies are calculated for Cu-Kα radiation (E = 8.05 keV). In this region, the X-ray absorption is less pronounced and allows much higher theoretical efficiencies for the discussed materials. However, the optimum lens thicknesses are higher. Therefore, much longer patterning times are required to achieve the optimum thicknesses. Moreover, the aspect ratios that can be achieved using IBL is limited. This means that the fabrication is not only impractical due to long patterning times, but also not realistic due to the limitations of the fabrication method. The solid curves show what is achievable with the current technology using the suggested fabrication method and materials, and the short dotted curves represent theoretical calculations but cannot be achieved by using gray-scale direct-write IBL as the suggested fabrication method, if the same aspect ratio is to be kept.

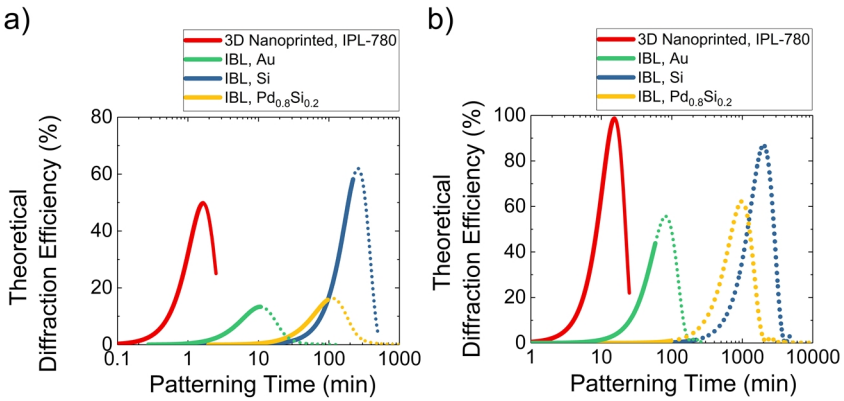

Figure 5.12 Patterning time vs. theoretical DE graphs comparing 3D printing to the state of the art ion beam lithography technique for various materials. a) for soft X-rays at 1 keV and b) for hard X-rays at 8.05 keV. The dotted curves show the theoretical calculations which are not realistic due to the limitations of the IBL fabrication method. The figure is adapted from Sanli *et al*.[30]

5.4. On-Chip Integrated X-ray Lenses using 3D printing

Horizontally Stacked Kinoform Lenses

Arbitrary geometries in the nanoscale can now be realized using 3D nano-printing. This allows the realization of new optics that have been considered impossible or unfeasible before. For instance, on-chip stacking of various 2D or 3D optics can now be realized. These new types of integrated, high-efficiency, high-performance X-ray optics can unlock new applications in both hard and soft X-ray imaging. Integration of various optical elements is conceptually shown in Figure 5.13a. Focusing optics can be integrated with any optical device such as wavefront shaping and correction plates[129] and combine various functions even for hard X-rays. As an example, on-chip horizontal stacking of 9 kinoform lenses of 2 µm optical thickness achieving an effective aspect-ratio of 45 is shown in Figure 5.13b. The estimated theoretical DE as a function of the number of stacked lenses significantly expands the energy range to several tens of keV (Figure 5.13c). This configuration offers the same focal spot size as the single-lens configuration, which is an order of magnitude better than the recently realized printed hard X-ray CRLs.[130]

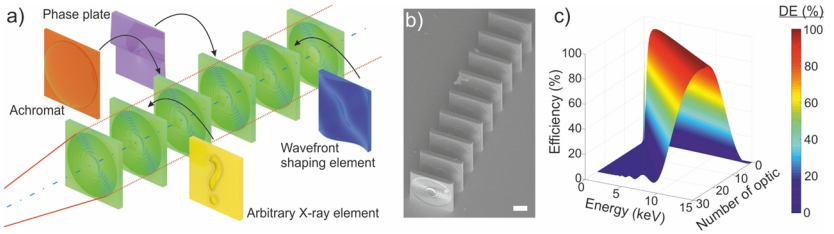

Figure 5.13 Applications of 3D nano-printing to advanced X-ray optics. a) The conceptual design that allows integrating any type of X-ray optical element into a stack of lenses. The optical elements can be kinoforms with achromatic elements, beam splitters, phase plates, wavefront shaping and aberration correcting elements b) Horizontally stacked kinoform lenses, each lens having 2 µm optical thicknesses. A 1 µm thick support element is printed along with the kinoforms. The combined filtering of incident radiation due to the support structure is in the order of a few percents at 8 keV and strongly decreases as energy increases. Scale bar 10 µm. c) The diffraction

efficiency of stacked lenses as a function of energy and number of lenses each having a 2 µm optical thickness (does not include the effect of support). The figure is adapted from Sanli *et al*.[30]

Horizontally stacked 3D nano compound refractive lenses

The described method also impacts other types of X-ray optics, such as nanofocusing lenses (NFLs), which are composed of a multitude of miniaturized refractive lenses. Owing to the challenging geometries, point-focusing 3D NFLs have been unavailable until recently. Instead, two sets of line focusing planar NFLs have been perpendicularly stacked ex-situ to achieve a point focus. Only very recently three groups have shown the realization of 3D printed NFLs.[130-132]. Fabrication of on-chip stacked 2D NFLs, and 3D NLFs, which are printed using IPL-780, are presented in Fig. 5.14. These optics are printed on a standard glass substrate as there is no need for an X-ray transparent substrate in this application.

While only individual refractive lenses of cylindrical and spherical geometries are presented here for simplicity, as one would expect, the concept explained in Figure 5.143 applies here as well. So, any individual lens geometry can be imagined such as parabolic, elliptic, achromatic, holographic and wavefront correcting elements and even non-symmetric optical elements (overall named as free-form optics) can be integrated into one, compact and monolithic X-ray lens thanks to the possibilities of additive manufacturing.

The attractive possibility for arrangements of multiple lenses and other optical elements in the near field will allow reaching the ultimate performance, especially in the hard X-ray range where absorption is much less. The integration of several additional optical components would allow aberration corrections and wave-front manipulation with ease. Therefore, the 3D-printed plastic optics will open new capabilities in X-ray focusing and have a strong impact for the optimal use of new highly brilliant X-ray source as well advanced laboratory sources, where radiation intensity is still the most critical issue.

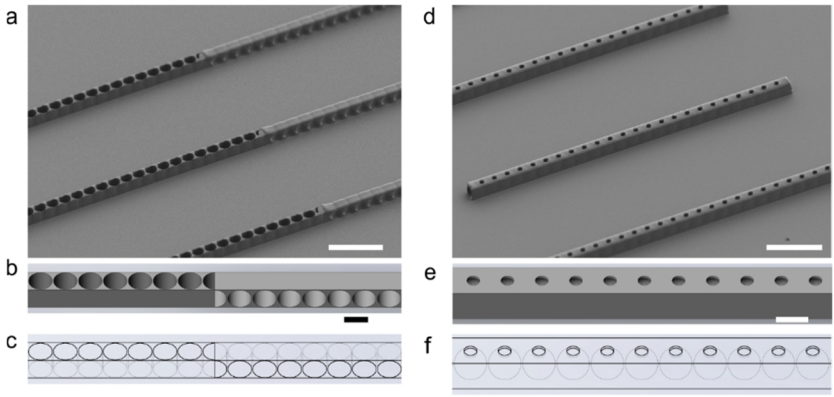

Figure 5.14 Application of 3D nano-printing to Nano-Focusing Lenses (NFLs). a) An SEM image of nano-printed 2D NFLs shows two sets of perpendicular NFLs, stacked on-chip by direct 3D printing. The diameter of each cylindrical lens is 5 µm. Scale bar 20 µm b) CAD drawing of 2D NFLs where scale bar of 5 µm corresponds to the diameter of a single lens. c) Transparent CAD drawing shows the perpendicular alignment of 2D NFLs. d) An SEM image is showing the 3D NFL. Each 3D NFL is composed of 25 spherical refractive lenses with a diameter of 5 µm. The openings on top of each spherical element are left for the evacuation of the un-exposed resin during development and CPD. Scale bar 20 µm. e and f) Solid and transparent CAD drawing of 3D NFLs, respectively, showing the internal structure of 3D NFLs with spherical cavities serving as individual lenses. Scale bar 5 µm. The figure is taken from Sanli *et al*.[30]

Table 5.3 Overview of the laser power and scan speed parameters used for 3D printing Stacked kinoforms and NLFs.

Type	Resist	Optical thickness	Laser Power (mW)	Scan Speed (mm/s)	Contour Number	Dosage (µJ/µm)
Horizontally stacked kinoform	IP-S	9 x 2 µm	32	15	3	2.13
2D NFLs	IPL-780	25 x 5 µm	32	15	3	2.13
3D NFLs	IPL-780	50 x 5 µm	32	25	3	1.28

5.5. Summary and Conclusions

Over the last decade, the macro-scale 3D printing went beyond being a rapid prototyping technique and has become a mainstream manufacturing method with applications

from aerospace to medical technology, including printing of the cartilage for lab-grown organs.

The developments in materials chemistry and laser technology brought about a new type of nano-scale 3D printing technology that allows printing structures with sub-micron dimensions, namely the two-photon polymerization (2PP). In a typical 2PP process, an intense IR-laser beam is spatiotemporally compressed into a small spot leading to a significant increase in the probability of two infrared photons to be absorbed as a single UV photon. This process happens only above a threshold intensity value that is much smaller than the Gaussian beam waist of a tightly focused beam allowing structures significantly smaller than the wavelength to be written.

While most of the high-resolution lithography techniques are limited to binary or quasi-three-dimensional structures, a unique feature of 2PP is to allow for the fabrication of true-3D structures with overhang features and extremely high aspect ratios. This true-3D structuring capability is impressive from the standpoint of X-ray optics because many theoretical types of X-ray optics with high diffraction efficiencies or high resolutions remain out of reach due to the limits of available fabrication methods.

Here, in Chapter 5, the successful nanofabrication of X-ray kinoform lenses was demonstrated using 2PP. Kinoform lenses can theoretically focus 100 % of the incident radiation into a single focus. In reality, however, fabrication difficulties and the absorption in the material decrease the efficiency of the optics. In literature, various approximations to actual kinoforms were shown. While some of these studies achieved efficiencies in the order of 50 % in the hard X-ray energies, the resolving power remained low mainly due to the various limitations fabrication methods and routes such as e-beam lithography. More recently, it was possible to utilize a gray-scale ion beam lithography method to produce quasi-3D structures. However, the final aspect ratio achievable in via this route is limited by the ability to transport material from the milled trenches,[58] which puts a geometrical limit on the aspect ratio that can be achieved using the gray-scale IBL route.

2PP based nano-printing overcomes these limitations almost by its nature. The polymer resins used in the 2PP process have high carbon contents resulting in an X-ray performance virtually on par with another carbon-based material that is ideal for X-ray optics but very difficult to micro-machine, diamond.

It has been demonstrated that absolute diffraction efficiencies reaching 20 % are achievable using lenses that are printed within a minute using 2PP, achieving up to 95% of their theoretical efficiencies, meeting the demands of the emerging coherent diffractive imaging method called ptychography excellently. The lenses had a direct imaging resolution of about 240 nm (half-pitch, cut-off) thanks to a spot size that is an order of magnitude smaller than 3D-printed CRLs reported in the literature. The images did not show any hint of astigmatism. Moreover, the lenses were used for ptychography, where the smallest features of 30 nm in an SS test pattern were resolved. Direct imaging and ptychography experiments matched-up with theoretical estimations confirming the high-quality of the optics, and the fabrication method.

The flexibility of the 2PP method allows fabrication of complex X-ray optics geometries. For instance, a train of optics with various properties can be printed on a substrate to serve several purposes. The desired function could be, for instance, beam shaping, wavefront correction, or focusing. To demonstrate the on-chip integration capability, a train of 9 kinoforms were printed on a glass carrier with an equivalent aspect ratio of 45. This type of flexibility extends the energy range where these optics can be useful, well into the hard X-ray regime. Looking into the future, I believe the 3D printed X-ray optics will become ubiquitous in a variety of X-ray focusing, imaging, and microscopy applications.

Appendix

A. Diffraction Efficiency Measurements

Pinhole scan method for DE estimation

To estimate the measured DE of the FZPs, a pinhole with a diameter of $4.4\ \mu m$ was raster scanned in the 1^{st} order focal plane while recording the incident intensity, projected 0^{th} order of the lens and the 1^{st} order focal spot at the same time. Figure A1a shows an example pinhole scan. The first order intensity the intensity through the reference illumination and the intensity passing through the Au layer (in the case of IBL-FZPs) is denoted in the figure. The intensities per pixel are calculated by dividing the measured intensities to the area of the pinhole. The intensity incident on the FZP area is calculated by integrating the intensity/pixel to the active area of the FZP. The diffraction efficiency is then given by the ratio of the intensity at the focal spot and the intensity incident on the FZP zones.

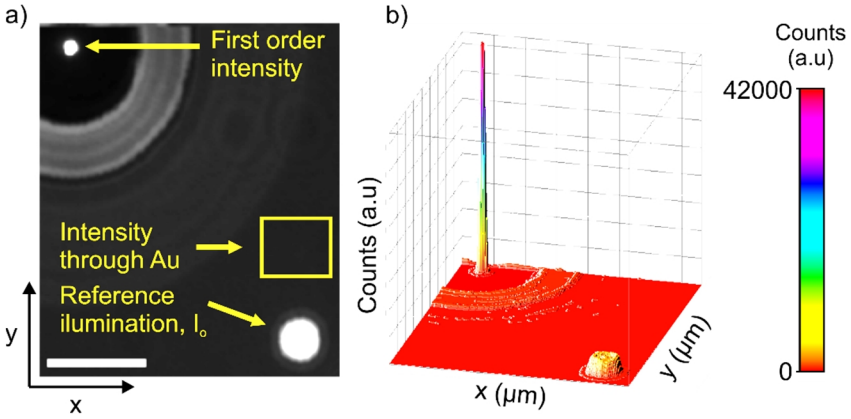

Figure A.1. Experimental DE with a reference hole.

Estimation of the incoming intensity in the case of no reference hole

In some of the IBL-FZPs, there was no reference hole present on the membrane. In such cases, the I_o was calculated using the beer lambert law.

$$I = I_0 e^{-\rho\mu x}$$

Experimentally obtained values of μ (the mass absorption coefficient or photo-absorption cross-section) for discrete X-ray emission energies have been collected and published by Henke *et al*.[12] The μ values used in this work is estimated by linear interpolation of the experimental data points. The I_o has an exponential dependence on the volumetric mass density of Au. Therefore, the precision of the estimation of the I_o depends on the preciseness of the density.

In this study, the density of Au was estimated using the IBL-P5 efficiency scan at 1100 eV to be 19.15 g/cm^3 (see table below for the parameters). The intensity through the reference in the membrane of IBL-P5 allows the use of the beer lambert law to estimate the density of the Au layer.

Table A.1 Parameters used for Au density estimation

I_o (counts)	I (counts)	μ (cm^2/g)	x (nm)	d (g/cm^3)
2850	193	4015	350	19.15

Avalanche Photo Diode (APD) Calibration Curve

The detection efficiency of the APD depends on the number of incident photons. Especially for high photon fluxes the detected intensities deviate from real intensities as shown in Figure A.2 and have to be calibrated using the calibration curve below for higher accuracy.

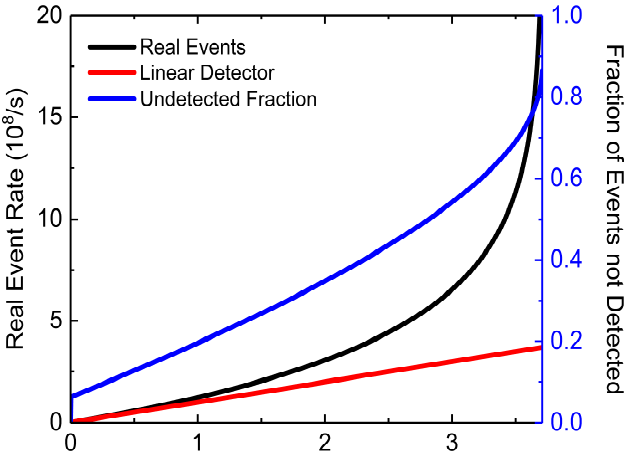

Figure A.2 APD calibration curve showing the relationship between real events and detected events. Figure adapted with permission from[19] with the updated calibration values.

B. Beamstop Deposition and Estimation of the Spillover Deposition

A separate FIBID Pt deposition was made on Au coated Si_3N_4 membrane to investigate the amount of spillover deposition on the FZP zones during beamstop deposition. The beamstop for ML-FZPs is deposited generally in 4 steps as detailed in the Figure below. The FIB cross-section reveals an average of 115 nm Pt spill over deposition on the region (denoted with a pink ring in Figure B1) of the FZP zones considering an FZP diameter of 39.5 and a beamstop diameter of 25 µm.

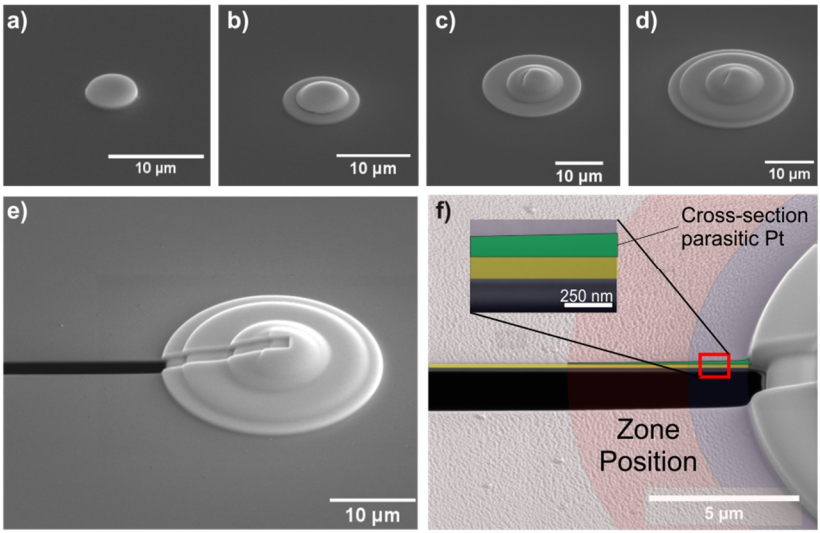

Figure B.1 Scanning electron microscopy (SEM) images of ion beam induced Pt-Ga-C test deposition on Si_3N_4 membrane coated with Au showing the significance of parasitic effects during beamstop deposition. The beamstop is usually deposited in 4 consecutive steps at 30 keV accelerating voltage. a) Diameter of d = 5 µm, beam current I = 100 pA b) Diameter of d = 10 µm, beam current of I = 300 pA c) Diameter of d = 20 um, beam current of I = 1 nA d) Diameter of d = 25 µm, beam current of I = 1 nA, e) a cross-section in the FIB was milled out to determine the thickness of the Pt-Ga-C layer. f) Cross-section image of a higher magnification image of the Pt-Ga-C parasitic deposition. The pink area represents the location of the FZP zones. Green area shows the thickness of the Pt-Ga-C layer. The yellow area shows the deposited Au layer. The figure is adapted from Sanli et al.[33]

C. Ptychography Set-Up details

Properties of the pnCCD detector

The physical properties of the pnCCD detector are listed in Table C.1 below.

Table C.1 Properties of the pnCCD detector. Data were taken from [53,133]

Parameter	Value
Number of pixels	264 × 264
Pixel size	48 µm
Image area	12.7 × 12.7 mm^2
Frame rate	up to 1 kHz
Quantum efficiency	95 % at 3-10 keV
Readout speed	28 MPixel/s
Readout noise (RMS)	<3 e^-/pixel
Full well capacitance	10^5 e^-
Charge transfer efficiency	0.99995

D. Details of the SENTECH ALD Instrument

Schematic Representation of the SENTECH ALD System at the MPI-IS.

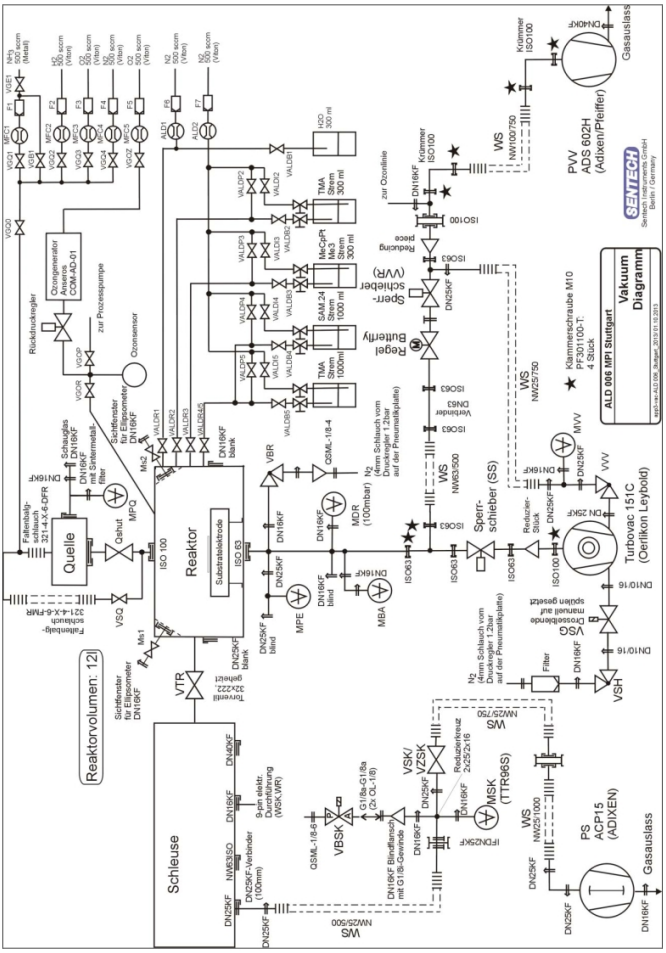

Figure D.1. Diagram showing the design of the ALD Instrument. Taken from SENTECH user manual.

Graphical User Interface (GUI) of the SENTECH ALD Instrument

The SENTECH ALD system has a GUI to control. From the GUI the ALD valves, shutters, gas flows temperatures plasma parameters, pumps, ellipsometry, etc. can be adjusted. A picture of the user interface is shown in Figure D.2 below.

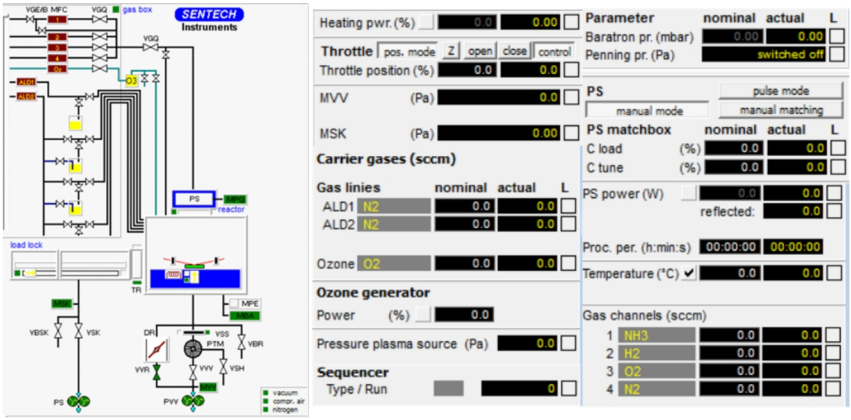

Figure D.2 Graphical user interface of the SENTECH ALD instrument.

However, the parameters of the depositions should be programmed. The process parameters, as well as the thickness of the deposition, are delivered to the ALD instrument using a recipe, which is a Delphi based programming language developed by SENTECH Instruments GmbH. The ALD cycles defined by the pulse and purge times of the precursors, which are controlled by the opening and closing times of the ALD valves, are assigned separately using a sequencer (see Figure D.3). A Call function for the sequencer is included in the recipe to execute the deposition in the desired number of cycles. The optimized pulse and purge times for one ALD cycle for alumina deposition at 290 °C is shown in Figure D.3. Here, the sequencer is responsible for opening the ALD valve for TMA (denoted as the VALDB5) for 20 ms, wait for 1980 ms for the first half-reaction to finish, and then pulse the H_2O for 20 ms and wait another 1980 ms to complete one ALD cycle.

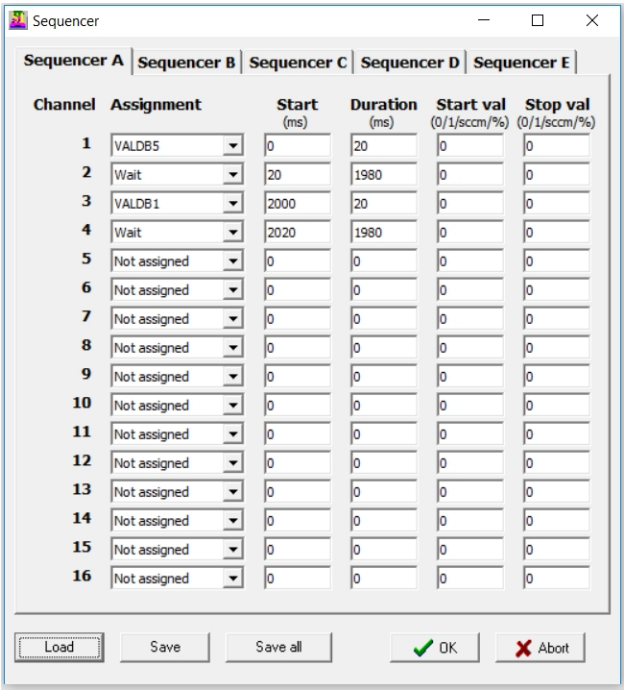

Figure D.3 Sequencer written for controlling the valves for one cycle Al_2O_3 deposition. VALDB5 is the ALD valve for TMA, and VALDB1 is the ALD valve for H_2O.

The programming based input system of the SENTECH ALD system allows complex depositions such as the FZP deposition, where the structure requires generally more than 100 multilayers with each layer having a different thickness. The number of cycles required to achieve the desired thickness for each FZP zone is calculated from the given GPC values using the zone plate law directly in the ALD software. The recipe for the tilted FZP deposition is given as an example below:

Recipe used for the ALD of the Tilted ML-FZP

' Use following carrier gas flows during processing:
Dim Purge_Flow_H2O As Real = 80
Dim Purge_Flow_TMA As Real = 80
Dim Purge_Flow_SAM_24 As Real = 40
Dim Source_O2_Flow As Real = 200
'
' Use following throttle valve positions during processing:
Dim Al2O3_Throttle_Valve_Position As Real = 100
Dim SiO2_Throttle_Valve_Position As Real = 30.2
'
' Use following plasma source parameters during processing:
Dim Source_Power As Real = 200
Dim SiO2_C_Load_Position As Real = 66.1
Dim SiO2_C_Tune_Position As Real = 45.8
'
' Assume following growth per cycles (nanometers/cycle)
Dim Al2O3_GPC As Real = 0.059
Dim SiO2_GPC As Real = 0.1304
'
' Use following variables for FZP zone calculation
Dim ZH As Real = 0.0
Dim NI2 As Integer = 0
Dim BS As Real = 0
Dim TH As Real = 0.0
Dim RN As Real = 0
Dim LAM As Real = 0
Dim RN1 As Real = 0.0
Dim NZ_TMP As Real = 0
Dim NZ As Integer = 1
Dim DR As Integer = 0
Dim F As Real = 0.0
Dim NI As Integer = 0
Dim D As Integer = 0
Dim THI[NI] As Real = 0
Dim Al2O3_Number_of_Cycles[NI] As Real = 0
Dim SiO2_Number_of_Cycles[NI] As Real = 0
Dim Target_LAYER_Cycles As Real = 0
Dim Cycle As Integer = 0
Dim Return_Value As Integer = 0
Dim Actual_Value_PRESSURE_PLASMA_SOURCE As Real = 0

```
Dim Actual_Value_PRESSURE_REACTOR As Real = 0
Dim START_TIME As Real = 0
Dim I As Integer = 0
RxDruck 0.00 Pa
'
' Save the following variables
LogOn Var C1 TH
LogOn Var C2 NZ
LogOn Var C3 ZH
LogOn Var C4 RN1
LogOn Var C5 THI[NI]
LogOn Var C6 NI
LogOn Var C7 RN
LogOn Var C8 Target_LAYER_Cycles
LogOn Var C9 Cycle
'
' Calculate the number of zones of the FZP using the following parameters
Calc BS = 31500                 %Beamstop diameter
Calc LAM = 1.239                % Wavelength
Calc DR = 20                %Outermost zone width
Calc D = 39500              % FZP Diameter
Calc NZ_TMP = D/(4*DR)          % Number of zones
:loop
Calc NZ = NZ+1
If NZ <= NZ_TMP Goto loop
Calc NZ_TMP = 0
Calc F = ((D*D)-(NZ*NZ*LAM*LAM))/(4*NZ*LAM)          %Focal length
'-------------------------------------------------------------------------------------
'                                Deposition Recipe
'-------------------------------------------------------------------------------------
Close Shuttter ellipsometer
'*****************Formula for Calculating Zone Thicknesses***************
Calc NI = 1
:Calculate_Zone_Thickness from FZP Law
Calc RN = sqrt(NI*LAM*F+NI*NI*LAM*LAM/4)
If RN < BS/2 Calc NI2 = NI2+1
If RN < BS/2 Goto Ni_Counter
Calc RN1 = sqrt((NI-1)*LAM*F+(NI-1)*(NI-1)*LAM*LAM/4)
Calc TH = RN-RN1
Calc THI[NI] = TH
Calc ZH = THI[NI]
Sleep 1000
:Ni_Counter
```

```
Calc NI = NI+1
If NI <= NZ Goto Calculate_Thickness
Calc RN = 0
Calc RN1 = 0
Calc TH = 0
Calc NI = 0
'****************************************
Call calculate_all_number_of_cycles
ALD line 1 Purge_Flow_H2O sccm ' N2, H2O
ALD line 5 Purge_Flow_TMA sccm ' N2, Precursor 5
Throttle position Al2O3_Throttle_Valve_Position %
Waittime 1:00
Calc NI = NI2
:deposit_multilayer
Calc NI = NI+1
Call Al2O3_layer
Calc NI = NI+1
If NI > NZ Goto end_of_multilayer
Call SiO2_layer
If NI < NZ Goto deposit_multilayer
:end_of_multilayer
Calc NI = 0
Call shutdown
Exit
'
'------------------------------
'----- CALL Functions ------
'------------------------------
:calculate_all_number_of_cycles
If Use_Different_Thickness_for_First_Layer <> 1 Goto skip_first_layer_thickness_mod-
ification
Calc NI = NI2+1
' %A new zone theoretically might not start at the exact same point where the glassfi-
ber ends. This is to have the first zone suit the law
Calc THI[NI] = (sqrt(NI*LAM*F+NI*NI*LAM*LAM/4))-(BS/2)
:skip_first_layer_thickness_modification
If Use_Different_Thickness_for_Last_Layer <> 1 Goto skip_last_layer_thickness_modi-
fication
Calc NI = NZ+1
Calc THI[NI] = Different_Thickness_for_Last_Layer
:skip_last_layer_thickness_modification
'
Calc NI = NI2
```

```
:calculate_numbers_of_cycles_loop
Calc NI = NI+1
Calc Al2O3_Number_of_Cycles[NI] = THI[NI]/Al2O3_GPC
'
Calc NI = NI+1
If NI > NZ+1 Goto end_calculation_of_numbers_of_cycles
Calc SiO2_Number_of_Cycles[NI] = THI[NI]/SiO2_GPC
'
If NI < NZ+1 Goto calculate_numbers_of_cycles_loop
:end_calculation_of_numbers_of_cycles
'
Calc NI = NI2
WZeit 1
:display_calculated_layer_values
Calc NI = NI+1
Calc TH = THI[NI]
Calc Target_LAYER_Cycles = Al2O3_Number_of_Cycles[NI]
Sleep 1000
'
Calc NI = NI+1
If NI > NZ Goto end_display_calculated_layer_values_in_datalogging
Calc TH = THI[NI]
Calc Target_LAYER_Cycles = SiO2_Number_of_Cycles[NI]
Sleep 1000
'
If NI < NZ Goto display_calculated_layer_values
:end_display_calculated_layer_values_in_datalogging
'
Calc NI = NI2
Calc TH = 0
Calc Target_LAYER_Cycles = 0
Return
'
:Al2O3_layer
' Set up process parameters:
ShutZu Q
ALD 1 Purge_Flow_H2O sccm ' N2, H2O
ALD 5 Purge_Flow_TMA sccm ' N2, Precursor 5
Calc Cycle = 0
Calc I = 0
Calc Target_LAYER_Cycles = Al2O3_Number_of_Cycles[NI]
'
:Al2O3_layer_loop
```

```
Calc Cycle = Cycle+1
Calc I = I+1
Sequencer B 1
'
If Cycle+1 < Al2O3_Number_of_Cycles[NI] Goto Al2O3_layer_loop
' If the missing cycle part is equal to 0.5 or greater an additional ALD cycle is per-
formed.
If Al2O3_Number_of_Cycles[NI]-Cycle >= 0.5 Goto Al2O3_layer_loop
'
' Stop process gases and pump the reactor:
RxDruck 0.00 Pa
ALDAus 1 ' N2, H2O
ALDAus 5 ' N2, TMA
WZeit 1
Calc Target_LAYER_Cycles = 0
Calc Cycle = 0
Calc I = 0
Return
'
:SiO2_layer
' Set up process parameters:
Call open_plasma_suorce_shutter
ShutZu E
QMBMan SiO2_C_LOAD_Position % SiO2_C_TUNE_Position %
GasEin MFC 3 SOURCE_O2_Flow sccm ' O2
ALDEin 4 Purge_Flow_SAM_24 sccm ' N2, Precursor 4
Throttle position SiO2_Throttle_Valve_Position %
WZeit 25
Set SOURCE_POWER W
'
Calc Target_LAYER_Cycles = 0
Calc Cycle = 0
Calc I = 0
Calc Target_LAYER_Cycles = SiO2_Number_of_Cycles[NI]
'
:SiO2_layer_loop
Calc Cycle = Cycle+1
Calc I = I+1
Sequencer A 1
'
If Cycle+1 < SiO2_Number_of_Cycles[NI] Goto SiO2_layer_loop
' If the missing cycle part is equal to 0.5 or greater an additional ALD cycle is per-
formed.
```

```
If SiO2_Number_of_Cycles[NI]-Cycle >= 0.5 Goto SiO2_layer_loop
'
' Stop process gases and pump the reactor:
RxDruck 0.00 Pa
GasAus MFC 3 ' O2
ALDAus 4 ' N2, Precursor 4
WZeit 3
StopGases
Qaus
WZeit 1
ShutZu Q
WZeit 10
'
Calc Target_LAYER_Cycles = 0
Calc Cycle = 0
Calc I = 0
WZeit 2
StopGases
Qaus
WZeit 1
ShutZu Q
Return
'
:shutdown
' Defined shut down sequence:
RxDruck 0.00 Pa
Qaus
WZeit 1
ALDAus 1 ' N2, H2O
ALDAus 2 ' N2, Precursor 2
ALDAus 3 ' N2, Precursor 3
ALDAus 4 ' N2, Precursor 4
ALDAus 5 ' N2, Precursor 5
WZeit 1
GasAus MFC 1 ' NH3
GasAus MFC 2 ' H2
GasAus MFC 3 ' O2
GasAus MFC 4 ' N2
WZeit 1
OzonPwrAus
OzonAus
WZeit 60
Call open_plasma_suorce_shutter
```

```
ShutZu E
OutAA AA_TEL 175.0 °C
WZeit 1:00:00
OutAA AA_TEL 150.0 °C
WZeit 1:00:00
OutAA AA_TEL 125.0 °C
WZeit 1:00:00
OutAA AA_TEL 100.0 °C
WZeit 1:00:00
OutAA AA_TEL 0.0 °C
Return
'
:open_plasma_suorce_shutter
' Compare the pressures in the plasma source and the reactor chamber. Open Source
bypass and wait till the difference is small enough if needed:
Set Actual_Value_PRESSURE_PLASMA_SOURCE = AE_MPQ ' Pa
Set Actual_Value_PRESSURE_REACTOR = AE_Bara ' Pa
If abs(Actual_Value_PRESSURE_PLASMA_SOURCE-Actual_Value_PRESSURE_REACTOR)
< 9 Goto open_shutter_immediately
ShutZu Q By
Sleep 20
Goto open_plasma_suorce_shutter
'
:open_shutter_immediately
' First, close bypass of the plasma source:
ShutZu Q
' Second, open the shutter of the plasma source:
ShutAuf Q
Return
```

Real-time data logging of the ALD processes

Every variable used during the ALD deposition can be monitored in real-time and saved. An example of logged real-time data is shown in the Figure below.

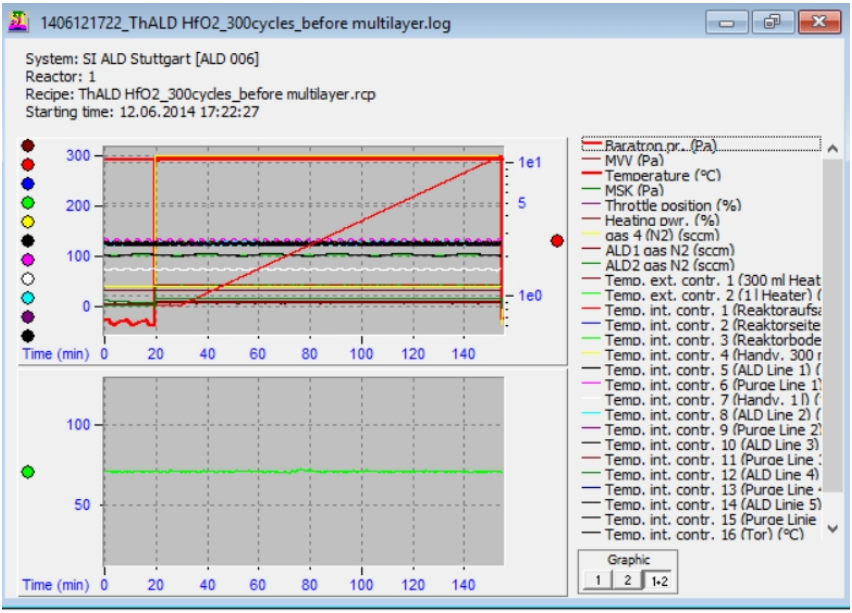

Figure D.4 Image showing graphs of the variables logged during ALD deposition.

E. Methods Used in Chapter 4

Atomic Layer Deposition

Optical quality glass fibers from Schott AG (Germany) with the product code A2/30 µm were used as the core. The Al_2O_3-HfO_2 thin films were deposited with a SENTECH SI ALD LL instrument (Germany) at 290 °C. For the Al_2O_3 deposition trimethylaluminum (TMA) (99.999+% Al) and deionized H_2O precursors were used. For the HfO_2 deposition $Hf[N(CH_3)_2]_4$ (98+%) and deionized H_2O precursors were used. Only $Hf[N(CH_3)_2]_4$ was heated to 70 °C to achieve higher vapor pressure. N_2 gas of purity 6.0 was used as the carrier gas for the precursors. Prior to FZP deposition, growth per cycles (GPC) of the Al_2O_3 and HfO_2 thin films were measured in a test deposition on Si Wafers manufactured via a spectroscopic ellipsometry and determined to be 0.078 and 0.097 nm per cycle, respectively. For the ML-FZP, nonstandard 1:2 line (HfO_2) to space (Al_2O_3) ratio was used instead of the standard 1:1, which allowed for faster deposition. ALD for Tapered ML-FZPs: Al_2O_3–SiO_2 multilayers of 1:1 line to space ratio were deposited on tapered micropillars prepared by PFIB (see Micropillar Fabrication via PFIB) using a SENTECH SI ALD LL instrument (Germany) at 200 °C. For the Al_2O_3 deposition, TMA (99.999+% Al) and deionized H_2O precursors were used. For the SiO_2 deposition bis[diethylamino]silane (BDEAS) and O_2 plasma (O_2 gas of purity 6.0) were used. The plasma power was 200 W. Only BDEAS was heated to 70 °C to achieve the necessary vapor pressure. N2 gas of purity 6.0 was used as carrier gas for the precursors. Prior to FZP deposition, GPC of the Al_2O_3 and SiO_2 thin films were measured in a test deposition on Si Wafers via spectroscopic ellipsometry and determined to be 0.059 and 0.1304 nm per cycle, respectively.

Wavelength-Dispersive X-Ray Spectroscopy

Al_2O_3 and HfO_2 thin films were deposited via ALD on separate 4 in. Si wafers using the ALD parameters of Table 2. Wavelength-dispersive X-ray spectroscopy was performed

with a Cameca SX100 Electron Probe Micro Analyzer. Al_2O_3 and HfO_2 thin films were measured using an accelerating voltage of 5 kV, a beam current of 40 nA and a beam diameter of 5 µm. To eliminate the instrument effects, analysis with matched standards was performed. A pure sapphire mineral was used as a standard for the elements Al and O, and a Hf crystal was used as a standard for the element Hf. Background correction was done by measuring the mean intensity of the background radiation on both sides of the peak and subtracting this value from the intensity of the element characteristic X-rays. To account for the matrix effects, a ZAF (Z: atomic number, A: absorption, F: fluorescence excitation) correction was done in the WDX software. An iterative procedure was followed using the K-ratios for calculating the stoichiometry.

X-Ray Photoelectron Spectroscopy

Al_2O_3 and HfO_2 thin films were deposited via ALD on separate 4 in. Si wafers using the ALD parameters in the Table 2. XPS analysis was performed via a Thermo VG Theta probe 300 system with monochromatic Al-K_α radiation (1468.68 eV; spot size 400 µm). Both samples suffered from high C concentration in the surface due to atmospheric exposure which does not affect the optical performance. To confirm, the XPS measurements were repeated after an in situ Ar^+ sputter-etching (2 keV, 30 s, raster 3 × 3 mm). The XPS analysis with in situ Ar^+ sputter-etching showed <1.5 at% C concentration. The very low C1s peak present at the XPS data of Figure 4.9are related to the surface C–C and C–H contamination during the XPS measurement, which was not visible directly after the Ar^+ sputter-etching. This suggests that the C content in the Al_2O_3 and HfO_2 films should be well below <1.5 at%.

Scanning- and High-Resolution Transmission Electron Microscopy and Sample Preparation with the Dual Beam system

The EELS and EDX measurements were performed on a JEOL JEMARM200F microscope equipped with a cold field-emission electron source, a DCOR probe corrector (CEOS Co.

Ltd.), a 100 mm^2 JEOL Centurio EDX detector and a Gatan GIF Quantum ERS spectrometer. The microscope was operated at 200 kV, a semi-convergence angle of 21 mrad, giving rise to a probe size of 1 Å for analytical measurements. A collection semiangle of 112 mrad was used for EELS measurements. HRTEM experiments were performed at 200 kV with JEOL JEMARM200F, equipped with a cold field-emission gun and a CETCOR image corrector (CEOS Co. Ltd.). For the STEM, HRTEM, EELS and EDX analysis shown in Figure 4.8, a TEM sample was prepared from the deposited glass-fiber *via* the lift-out preparation technique using an FEI Nova Nanolab 600 Ga^+ Dual Beam system with an in-situ Omniprobe micro-manipulator and a gas injection system (GIS) that uses (methylcyclopentadienyl)trimethyl platinum as a precursor. The essential steps for a successful sample preparation that enabled the analysis in Figure 4.8 are presented in Appendix F.

X-ray Reflectometry

X-ray reflectometry measurements were conducted with a Siemens D5005 diffractometer equipped with an X-ray mirror for Cu Kα radiation on the same samples explained in XPS section. The data were fitted with the LEPTOS (Bruker) software.

Synchrotron Measurements

MAXYMUS beamline was utilized for the synchrotron experiments. For the diffraction efficiency measurements a pinhole of diameter, d = 4 µm was scanned over an area of 85 × 60 µm to image the ML-FZP mounted on the lift-out grid as in Figure 4.11b for each energy. The diffraction efficiency was calculated by dividing the average intensity of the 1^{st} order focus to the total intensity on the FZP zones. For imaging, an OSA of 15 µm width was placed between the ML-FZP and the sample. Michelson contrast was used for image contrast determination of the BAM-L200 sample in Figure 4.11d,e. For both of the images, the contrast was normalized to the highest (Michelson) contrast region

of the Figure 4.11d (the peak and minimum left to the feature P1). A background subtraction was done in the intensity profile of Figure 4.11e.

Diffraction Efficiency calculations

The CWT parameters used in Chapter 4 are summarized in the table below.

Table E.1 CWT parameters used for diffraction efficiency calculations. The magnification stands for the ratio of the distance of the source and focal distance. A magnification of 10000 is selected to mimic a plane wave illumination as in the case of the STXM set-up.

	Materials	Density (g/cm^3)	Local or Integrated	Line/Space
Table 4.3	Al_2O_3/HfO_2	3.0/8.9	Local (Only outermost period)	1:2
Fig. 4.14	Al_2O_3/HfO_2	3.0/8.9	Local (Only outermost period)	1:1
Fig. 4.20	Al_2O_3/SiO_2	3.0/2.1	Integrated (All zones)	1:1

F. Details of the TEM Sample Preparation using FIB

Deposition of a protection layer

It is well known that a focused ion beam will damage the sample upon interaction. The incident ions will penetrate into the sample and displace atoms by collision cascades and change the microstructure of the sample even deeper than the ion penetration depth. During the interaction, some ions may be implanted to the sample, and some of the atoms in the sample may be sputtered out. Therefore, prior to the use of the focused ion beam, a Pt protection layer using the electron beam is deposited over the area of interest. The area of the protection layer is generally larger than the final sample. Here, the area of the protection layer was a rectangle of 3x15 µm. The thickness of the electron beam deposited layer was about 300 nm. An additional >3 µm of protection layer was deposited on the same area by using the focused ion beam. The reason for using focused ion beam induced deposition is that the deposition is much faster compared to electron beam induced deposition.

Lift-out and transfer

Bulk out

Trenches are milled out on two sides of the protection layer by using regular cross-section (RCS) scanning pattern. The RCS milling is done with the sample stage tilted to 52° to have the focused ion beam column perpendicular to the area of interest. This is shown in Figure F1b. The depth of the RCS milling is deeper and wider than the area of interest to avoid ion beam damage in the following lift-out steps. The RCS is done at 30 kV acceleration voltage and 7 nA beam current. During the milling out of the trenches, the long glass-fiber sample may drift due to charging effects and long milling times. Therefore, the area of the RCS is not selected directly adjacent to the protection layer, but about half a micron further apart. A cleaning cross-section (CCS) pattern is used to

mill out the area left between the protection layer and the trenches. A smaller beam current of 3 nA is used in the CCS pattern.

U-cut

To separate the lamella from the rest, three rectangle patterns are milled out on the edges of the lamella resulting in a U-shape. The rectangles are about 2 µm wide and have an overlap of about 2 µm. A 2×2 µm of material is left connected to the bulk, which will be milled out after the lamella is connected to the Omniprobe micro-manipulator. The rectangular milling is done with the sample stage tilted to 7°, 30 kV acceleration voltage, and 3 nA beam current. The resulting structure is shown in Figure F.1d.

Lift-out and transfer

At 0° tilt, the Omniprobe micro-manipulator is inserted and attached to the lamella from the side using focused ion beam induced Pt deposition. This is shown in Figure F.1e. The remaining material (on the upper right corner of Figure F.1d) is milled out to separate the lamella from the bulk. The lamella is then mounted on an Omniprobe Mo Lift-out Grid using the FIBID again and cut free from the micro-manipulator using a rectangle pattern. It is essential that during the lift-out and mounting steps, the micro-manipulating needle is in the Eucentric height.

Thinning, window milling and polishing

The thinning is done in several steps with each step having many iterations using the CCS pattern. There is no one single procedure but rather some rule of thumbs to follow. The thinner the lamella gets, the smaller the beam voltage and current should be. This is done to avoid ion beam damage in the sample.

In the first step, the lamella is thinned down to about 1.5 µm by using 30 kV and 0.3-0.5 nA. This is done from both sides of the lamella with the sample stage tilted to 51° and 53° for different sides. The resulting structure is shown in Figure F.1h.

In the second step, the lamella is thinned down to about 250 nm by using 20 kV and 0.1 nA from both sides. The sample was analyzed after this step for the STEM images in Figure 4.8b and c.

The third step is the *window milling step.* In this step, the aim is to mill out several windows on the lamella with a thickness of below 100 nm using CCS pattern. This is done using 5 kV and 30 pA with the stage tilted to about 50° and 54° for different sides.

The final step is the *polishing* step. In this step, 2 kV and 10 pA rectangle milling are used. The sample stage is tilted away from the perpendicular position of 52° by ± 6° to the ion beam. The polishing step is applied to both sides and 2 min per side.

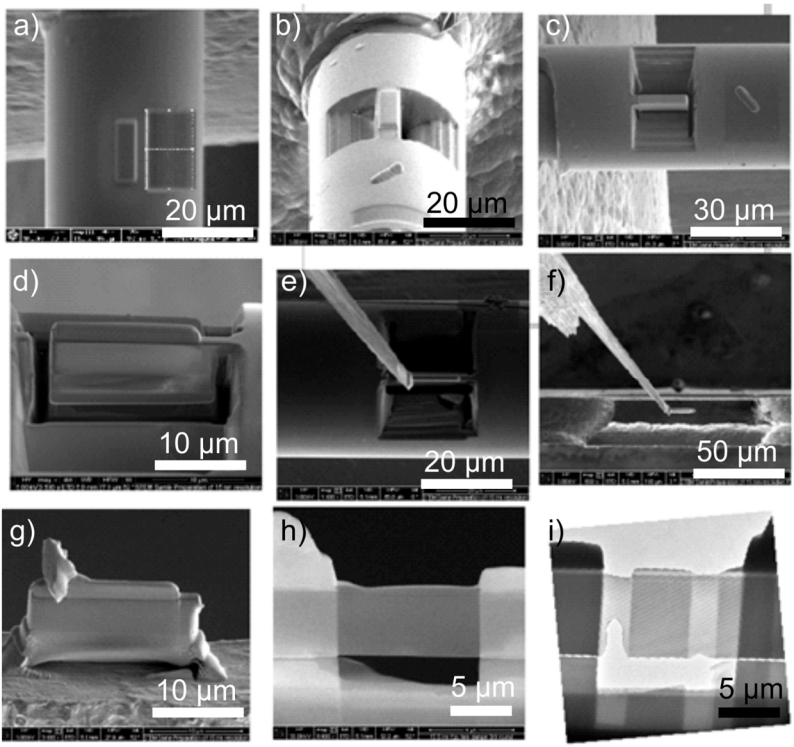

Figure F.1 TEM lamella preparation using the FIB

G. Methods used in Chapter 5

X-ray Microscopy Tests

Ptychography was done using a 2-µm thick kinoform at 800 eV using the 3rd undulator harmonic with exit slits set to 15×15 µm. The image with a 3-µm field of view was recorded with a dwell time of 100 ms per pixel, 50 nm steps (60 points) with a sample to camera distance of 15.5 cm. The direct X-ray detection camera consists of 264×264 pixels. At the energy of 800 eV, this corresponds to a reconstructed pixel size of 19 nm. The reconstruction was done using the SHARP ptychography package[54] performing 1000 iterations of relaxed averaged alternating reflection (RAAR) algorithm. Fourier beam propagation method was used to propagate the beam backward/forwards.

Electron microscopy analysis

For the SEM analysis, a ZEISS Gemini 500 SEM with a Field Emission electron source was used. The samples were coated with 20 nm of carbon prior to SEM analysis. To minimize charging effects, beam deceleration was used while acquiring the SEM images.

Chemical Composition Determination

The chemical composition of the IPL-780 photo-resist was determined by ELTRA-CS-800 Carbon-Sulphur determinator and ELTRA-ONH-2000 Oxygen-Nitrogen-Hydrogen determinator. The composition of the polymer was estimated to be 3.0 wt% hydrogen, 24.9 wt% oxygen, 0.8 wt% nitrogen, and 71.2 wt% carbon.

References

1 Röntgen, W. On a new kind of rays. *Nature* **53**, 274-276 (1896).

2 Röntgen, W. *Sitzungsberichte der Wurzburger Physik-medic* (1895).

3 Wind, C. H. Ueber die Deutung der Beugungserscheinungen bei Röntgenstrahlen. *Annalen der Physik* **304**, 896-901 (1899).

4 Friedrich, W., Knipping, P. & Laue, M. Interferenzerscheinungen bei roentgenstrahlen. *Annalen der Physik* **346**, 971-988 (1913).

5 Bragg, W. L. The specular reflection of X-rays. *Nature* **90**, 410 (1912).

6 Kirkpatrick, P. & Baez, A. V. Formation of optical images by X-rays. *JOSA* **38**, 766-773 (1948).

7 Horowitz, P. & Howell, J. A. A scanning X-ray microscope using synchrotron radiation. *Science* **178**, 608-611 (1972).

8 Niemann, B., Rudolph, D. & Schmahl, G. X-ray microscopy with synchrotron radiation. *Applied Optics* **15**, 1883-1884 (1976).

9 Attwood, D. T. *Soft X-rays and extreme ultraviolet radiation: principles and applications*. (Cambridge Univ Press, 2000).

10 Hecht, E. Optics 4th. (2002).

11 Michette, A. G. *Optical systems for soft X rays*. (Plenum Press New York, 1986).

12 Henke, B. L., Gullikson, E. M. & Davis, J. C. X-Ray Interactions: Photoabsorption, Scattering, Transmission, and Reflection at E = 50-30,000 eV, Z = 1-92. *Atomic Data and Nuclear Data Tables* **54**, 181-342 (1993).

13 Schütz, G., Goering, E. & Stoll, H. (John Wiley & Sons, Ltd, 2007).

14 Schütz, G. *et al.* Absorption of circularly polarized x rays in iron. *Phys. Rev. Lett.* **58**, 737-740 (1987).

15 Spaldin, N. A. & Mathur, N. D. Magnetic Materials: Fundamentals and Device Applications. *Physics Today* **56**, 62-63 (2003).

16 Hemberg, O., Otendal, M. & Hertz, H. M. Liquid-metal-jet anode electron-impact X-ray source. *Applied Physics Letters* **83**, 1483-1485 (2003).

17 Khan, S. Study of the Bessy II beam lifetime. (1999).

18 Attwood, D. & Sakdinawat, A. *X-rays and Extreme Ultraviolet Radiation: Principles and Applications*. (Cambridge university press, 2017).

19 Weigand, M. *Realization of a new magnetic scanning X-ray microscope and investigation of Landau structures under pulsed field excitation*. (Cuvillier Verlag, 2015).

20 Mimura, H. *et al.* Breaking the 10 nm barrier in hard-X-ray focusing. *Nat Phys* **6**, 122-125 (2010).

21 Michette, A. in *The Optics Encyclopedia* (Wiley-VCH Verlag GmbH & Co. KGaA, 2007).

22 Snigirev, A., Kohn, V., Snigireva, I. & Lengeler, B. A compound refractive lens for focusing high-energy X-rays. *Nature* **384**, 49-51 (1996).

23 Wood, R. W. *Physical optics*. 3 ed edn, (The Macmillan Company, 1934).

24 Soret, J. L. Über die durch Kreisgitter erzeugten Diffractionsphänomene. *Annalen der Physik* **232**, 99-113 (1875).

25 Rayleigh, L. Wave Theory of Light (in Encyclopedia Britannica). *New York* (1888).

26 Wood, R. W. Phase-reversal zone plates and diffraction telescopes. *Phil. Mag, Ser. 6* **45**, 511-523 (1898).

27 Bajt, S. *et al.* X-ray focusing with efficient high-NA multilayer Laue lenses. *Light: Science & Applications* **7**, 17162 (2018).

28 Maser, J. & Schmahl, G. Coupled wave description of the diffraction by zone plates with high aspect ratios. *Optics Communications* **89**, 355-362 (1992).

29 Kirz, J. Phase zone plates for x rays and the extreme uv. *Journal of the Optical Society of America* **64**, 301-309 (1974).

30 Sanli, U. T. *et al.* 3D Nanoprinted Plastic Kinoform X-Ray Optics. *Advanced Materials* **30**, 1802503 (2018).

31 Kogelnik, H. H. Kogelnik, Bell Syst. Tech. J. 48, 2909 (1969). *Bell Syst. Tech. J.* **48**, 2909 (1969).

32 Schneider, G., Rehbein, S. & Werner, S. in *Modern Developments in X-Ray and Neutron Optics* Vol. 137 (eds Alexei Erko, Mourad Idir, Thomas Krist, & Alan Michette) 137-171 (Springer Berlin / Heidelberg, 2008).

33 Umut Tunca Sanli *et al.* 3D Nanofabrication of High-resolution Multilayer Fresnel Zone Plates. *Submitted to Advanced Science* (2018).

34 Dingemans, G. & Kessels, W. Status and prospects of Al2O3-based surface passivation schemes for silicon solar cells. *Journal of Vacuum Science & Technology A: Vacuum, Surfaces, and Films* **30**, 040802 (2012).

35 Carcia, P., McLean, R. & Reilly, M. High-performance ZnO thin-film transistors on gate dielectrics grown by atomic layer deposition. *Applied physics letters* **88**, 123509 (2006).

36 George, S. M. Atomic layer deposition: an overview. *Chemical reviews* **110**, 111-131 (2009).

37 Johnson, R. W., Hultqvist, A. & Bent, S. F. A brief review of atomic layer deposition: from fundamentals to applications. *Materials today* **17**, 236-246 (2014).

38 Puurunen, R. L. Growth per cycle in atomic layer deposition: a theoretical model. *Chemical Vapor Deposition* **9**, 249-257 (2003).

39 Pinna, N. & Knez, M. *Atomic layer deposition of nanostructured materials*. (John Wiley & Sons, 2012).

40 Puurunen, R. L. Surface chemistry of atomic layer deposition: A case study for the trimethylaluminum/water process. *Journal of applied physics* **97**, 9 (2005).

41 Kääriäinen, T., Cameron, D., Kääriäinen, M.-L. & Sherman, A. *Atomic layer deposition: principles, characteristics, and nanotechnology applications*. (John Wiley & Sons, 2013).

42 Profijt, H., Potts, S., Van de Sanden, M. & Kessels, W. Plasma-assisted atomic layer deposition: basics, opportunities, and challenges. *Journal of Vacuum Science & Technology A: Vacuum, Surfaces, and Films* **29**, 050801 (2011).

43 Seliger, R. & Fleming, W. Focused ion beams in microfabrication. *Journal of Applied Physics* **45**, 1416-1422 (1974).

44 Melngailis, J. Focused ion beam technology and applications. *Journal of Vacuum Science & Technology B: Microelectronics Processing and Phenomena* **5**, 469-495 (1987).

45 Takagi, T. Ion–surface interactions during thin film deposition. *Journal of Vacuum Science & Technology A: Vacuum, Surfaces, and Films* **2**, 382-388 (1984).

46 Hellborg, R., Whitlow, H. J. & Zhang, Y. *Ion beams in Nanoscience and Technology*. (Springer Science & Business Media, 2009).

47 Jacobs, D. C. The role of internal energy and approach geometry in molecule/surface reactive scattering. *Journal of Physics: Condensed Matter* **7**, 1023 (1995).

48 Fuchs, E. Particle beam microanalysis. (1990).

49 Utke, I., Moshkalev, S. & Russell, P. *Nanofabrication using focused ion and electron beams: principles and applications*. (Oxford University Press, 2012).

50 Juodkazis, S., Mizeikis, V., Seet, K. K., Miwa, M. & Misawa, H. Two-photon lithography of nanorods in SU-8 photoresist. *Nanotechnology* **16**, 846 (2005).

51 Senoner, M. *et al.* Lateral resolution of nanoscaled images delivered by surface-analytical instruments: application of the BAM-L200 certified reference material and related ISO standards. *Analytical and bioanalytical chemistry* **407**, 3211-3217 (2015).

52 Pfeiffer, F. X-ray ptychography. *Nature Photonics* **12**, 9 (2018).

53 Bykova, I. High-resolution X-ray ptychography for magnetic imaging. (2018).

54 Marchesini, S. *et al.* SHARP: a distributed GPU-based ptychographic solver. *Journal of Applied Crystallography* **49**, 1245-1252 (2016).

55 Schropp, A. & Schroer, C. G. Dose requirements for resolving a given feature in an object by coherent x-ray diffraction imaging. *New Journal of Physics* **12**, 035016 (2010).

56 Schropp, A. *et al.* Hard X-ray scanning microscopy with coherent radiation: Beyond the resolution of conventional X-ray microscopes. *APPLIED PHYSICS LETTERS* **100**, 253112-253113 (2012).

57 Schroer, C. *et al.* Coherent x-ray diffraction imaging with nanofocused illumination. *Physical review letters* **101**, 090801 (2008).

58 Keskinbora, K. Ion beam lithographic and multilayer fresnel zone plates for soft and hard X-rays: nanofabrication and characterization. (2015).

59 Volkert, C. A. & Minor, A. M. Focused Ion Beam Microscopy and Micromachining. *MRS Bulletin* **32**, 374-376 (2007).

60 Giannuzzi, L. A. & Stevie, F. A. A review of focused ion beam milling techniques for TEM specimen preparation. *Micron* **30**, 197-204 (1999).

61 Giannuzzi, L. A. & Stevie, F. A. *Introduction to Focused Ion Beams: Instrumentation, Theory, Techniques and Practice*. (Springer, 2005).

62 Joshi-Imre, A. & Bauerdick, S. Direct-Write Ion Beam Lithography. *Journal of Nanotechnology* **2014** (2014).

63 Froese, H., Lötgering, L. & Wilhein, T. in *Holography: Advances and Modern Trends V.* 102331A (International Society for Optics and Photonics).

64 Keskinbora, K., Grévent, C., Eigenthaler, U., Weigand, M. & Schütz, G. Rapid Prototyping of Fresnel Zone Plates via Direct Ga+ Ion Beam Lithography for High-Resolution X-ray Imaging. *ACS Nano* **7**, 9788-9797 (2013).

65 Nadzeyka, A. *et al.* Ion beam lithography for direct patterning of high accuracy large area X-ray elements in gold on membranes. *Microelectronic Engineering* **98**, 198-201 (2012).

66 Keskinbora, K. *et al.* Ion beam lithography for Fresnel zone plates in X-ray microscopy. *Opt. Express* **21**, 11747-11756 (2013).

67 Cattoni, A. *et al.* Sub-10 nm electron and helium ion beam lithography using a recently developed alumina resist. *Microelectronic Engineering* **193**, 18-22 (2018).

68 Manfrinato, V. R. *et al.* Aberration-corrected electron beam lithography at the one nanometer length scale. *Nano letters* **17**, 4562-4567 (2017).

69 Yamauchi, K. *et al.* Single-nanometer focusing of hard X-rays by Kirkpatrick-Baez mirrors. *Journal of Physics: Condensed Matter* **23**, 394206-394206 (2011).

70 Schroer, C. G. *et al.* Hard X-ray nanoprobe based on refractive X-ray lenses. *Applied Physics Letters* **87**, 1-3 (2005).

71 Alianelli, L., Laundy, D., Alcock, S., Sutter, J. & Sawhney, K. Development of Hard X-ray Focusing Optics at Diamond Light Source. *Synchrotron Radiation News* **29**, 3-9 (2016).

72 Yan, H., Conley, R., Bouet, N. & Chu, Y. S. Hard X-ray nanofocusing by multilayer Laue lenses. *Journal of Physics D: Applied Physics* **47** (2014).

73 Huang, X. *et al.* 11 nm hard X-ray focus from a large-aperture multilayer Laue lens. *Scientific reports* **3** (2013).

74 Huang, X. *et al.* Achieving hard X-ray nanofocusing using a wedged multilayer Laue lens. *Optics Express* **23**, 12496-12507 (2015).

75 Kubec, A. *et al.* Point focusing with flat and wedged crossed multilayer Laue lenses. *Journal of Synchrotron Radiation* **24**, 413-421 (2017).

76 Vila-Comamala, J. *et al.* Zone-doubled Fresnel zone plates for high-resolution hard X-ray full-field transmission microscopy. *Journal of Synchrotron Radiation* **19**, 705-709 (2012).

77 Rehbein, S., Lyon, A., Leung, R., Feser, M. & Schneider, G. Near field stacking of zone plates for reduction of their effective zone period. *Opt. Express* **23**, 11063-11072 (2015).

78 Mohacsi, I. *et al.* Interlaced zone plate optics for hard X-ray imaging in the 10 nm range. *Scientific Reports* **7** (2017).

79 Yin, G. C. *et al.* 30 nm resolution X-ray imaging at 8 keV using third order diffraction of a zone plate lens objective in a transmission microscope. *Applied Physics Letters* **89** (2006).

80 Chen, Y.-T. *et al.* Full-field hard X-ray microscopy below 30 nm: a challenging nanofabrication achievement. *Nanotechnology* **19**, 395302-395302 (2008).

81 Chang, C. & Sakdinawat, A. Ultra-high aspect ratio high-resolution nanofabrication for hard X-ray diffractive optics. *Nature Communications* **5** (2014).

82 Gleber, S.-C. *et al.* Fresnel zone plate stacking in the intermediate field for high efficiency focusing in the hard X-ray regime. *Opt. Express* **22**, 28142-28153 (2014).

83 Jefimovs, K. *et al.* Zone-Doubling Technique to Produce Ultrahigh-Resolution X-Ray Optics. *Phys. Rev. Lett.* **99**, 264801-264801 (2007).

84 Mohacsi, I. *et al.* Fabrication and characterization of highefficiency double-sided blazed X-ray optics. *Optics Letters* **41**, 281-284 (2016).

85 Mohacsi, I. *et al.* High-efficiency zone-plate optics for multi-keV X-ray focusing. *Journal of Synchrotron Radiation* **21**, 497-501 (2014).

86 Fabrizio, E. D. *et al.* High-efficiency multilevel zone plates for keV X-rays. *Nature* **401**, 895-898 (1999).

87 Feng, Y. *et al.* Nanofabrication of high aspect ratio 24 nm X-ray zone plates for X-ray imaging applications. *Journal of Vacuum Science and Technology B: Microelectronics and Nanometer Structures* **25**, 2004-2007 (2007).

88 Werner, S. R. S. G. P. S. G. Three-dimensional structured on-chip stacked zone plates for nanoscale X-ray imaging with high efficiency. *Nano Research* **7**, 528-535 (2014).

89 Seiboth, F. *et al.* Hard X-ray nanofocusing by refractive lenses of constant thickness. *Applied Physics Letters* **105** (2014).

90 Sanli, U. T. *et al.* Vol. 9592 95920F-95920F-95928-95920F (2015).

91 Hart, H. E., Scrandis, J. B., Mark, R. & Hatcher, R. D. Diffraction Characteristics of a Linear Zone Plate. *J. Opt. Soc. Am.* **56**, 1018-1023 (1966).

92 Rudolph, D. & Schmahl, G. High Power Zone Plates For a Soft X-ray Microscope. *Annals of the New York Academy of Sciences* **342**, 94-104 (1980).

93 Rudolph, D., Niemann, B. & Schmahl, G. Status of the sputtered sliced zone plates for X-ray microscopy. *Proceedings of the Society of Photo-Optical Instrumentation Engineers* **316**, 103-105 (1981).

94 Pratsch, C., Rehbein, S., Werner, S. & Schneider, G. Influence of random zone positioning errors on the resolving power of Fresnel zone plates. *Opt. Express* **22**, 30482-30491 (2014).

95 Eberl, C. *et al.* Fabrication of laser deposited high-quality multilayer zone plates for hard X-ray nanofocusing. *Applied Surface Science* **307**, 638-644 (2014).

96 Mayer, M. *et al.* Multilayer Fresnel zone plate for soft X-ray microscopy resolves sub-39 nm structures. *Ultramicroscopy* **111**, 1706-1711 (2011).

97 Tamura, S. *et al.* Quasi-kinoform type multilayer zone plate with high diffraction efficiency for high-energy X-rays. *Journal of Physics: Conference Series* **186**, 012075-012075 (2009).

98 Suzuki, Y., Takeuchi, A., Terada, Y., Uesugi, K. & Tamura, S. in *Proc. SPIE*. 885109.

99 Döring, F. *et al.* Sub-5 nm hard X-ray point focusing by a combined Kirkpatrick-Baez mirror and multilayer zone plate. *Opt. Express* **21**, 19311-19323 (2013).

100 Tunca Sanli, U., Keskinbora, K., Grévent, C. & Schütz, G. Vol. 9510 95100U-95100U-95109-95100U (2015).

101 Koyama, T. *et al.* Circular multilayer zone plate for high-energy x-ray nano-imaging. *Review of Scientific Instruments* **83**, 013705, doi:10.1063/1.3676165 (2012).

102 Osterhoff, M., Soltau, J., Eberl, C. & Krebs, H.-U. in *X-Ray Nanoimaging: Instruments and Methods III.* 103890T (International Society for Optics and Photonics).

103 Ashby, M. F. Materials selection in mechanical design. *MRS Bull* **30**, 995 (2005).

104 Schneider, G. *High-resolution X-ray microscopy of radiation sensitive material*. (Cuvillier, 2000).

105 Schneider, G. Zone plates with high efficiency in high orders of diffraction described by dynamical theory. *Applied Physics Letters* **71**, 2242-2244 (1997).

106 Mistry, K. *et al.* in *Electron Devices Meeting, 2007. IEDM 2007. IEEE International.* 247-250 (IEEE).

107 Cao, Z. H., Hu, K. & Meng, X. K. Diffusion barrier properties of amorphous and nanocrystalline Ta films for Cu interconnects. *Journal of Applied Physics* **106**, 113513-113513 (2009).

108 Rossnagel, S. M., Sherman, A. & Turner, F. Plasma-enhanced atomic layer deposition of Ta and Ti for interconnect diffusion barriers. *Journal of Vacuum Science and Technology B: Microelectronics and Nanometer Structures* **18**, 2016-2020 (2000).

109 Kim, H., Cabral, C., Lavoie, C. & Rossnagel, S. M. Diffusion barrier properties of transition metal thin films grown by plasma-enhanced atomic-layer deposition. *Journal of Vacuum Science and Technology B: Microelectronics and Nanometer Structures* **20**, 1321-1326 (2002).

110 Narayan, J. *et al.* Epitaxial growth of TiN films on (100) silicon substrates by laser physical vapor deposition. *Applied Physics Letters* **61**, 1290-1292 (1992).

111 Vladimirsky, Y. & Koops, H. W. P. Moiré method and zone plate pattern inaccuracies. *Journal of Vacuum Science & Technology B: Microelectronics and Nanometer Structures* **6**, 2142-2146 (1988).

112 Liddle, J. A. & Gallatin, G. M. Nanomanufacturing: A Perspective. *ACS Nano* **10**, 2995-3014 (2016).

113 Minin, I. V. & Minin, O. V. Control of focusing properties of diffraction elements. *Soviet Journal of Quantum Electronics* **20**, 198-198 (1990).

114 Webb, G. W., Minin, I. V. & Minin, O. V. Variable Reference Phase in Diffractive Antennas: Review, Applications, New Results. *IEEE Antennas and Propagation Magazine* **53**, 77-94 (2011).

115 Tao, T., Wilkinson, W. & Melngailis, J. Focused Ion Beam Induced Deposition Of Platinum For Repair Processes. *Journal of Vacuum Science and Technology B:Nanotechnology and Microelectronics* **9**, 162-164 (1991).

116 Kang, H. C. *et al.* Nanometer Linear Focusing of Hard X Rays by a Multilayer Laue Lens. *Physical Review Letters* **96**, 127401-127401 (2006).

117 Koyama, T. *et al.* Development of Multilayer Laue Lenses; (1) Linear Type. *AIP Conference Proceedings* **1365**, 24-27 (2011).

118 Nazaretski, E. *et al.* Pushing the limits: an instrument for hard X-ray imaging below 20nm. *Journal of Synchrotron Radiation* **22**, 336-341 (2015).

119 Koyama, T. *et al.* Development of Multilayer Laue Lenses; (2) Circular Type. *AIP Conference Proceedings* **1365**, 100-103 (2011).

120 Mayer, M. W. R. A new production method for Fresnel zone plates for high-resolution X-ray microscopy and investigation of their imaging properties. (2011).

121 Keskinbora, K. *et al.* Multilayer Fresnel zone plates for high energy radiation resolve 21 nm features at 1.2 keV. *Opt. Express* **22**, 18440-18453 (2014).

122 Evans-Lutterodt, K. *et al.* Single-element elliptical hard X-ray micro-optics. *Opt. Express* **11**, 919-926 (2003).

123 Snigireva, I. *et al.* Holographic X-ray optical elements: transition between refraction and diffraction. *Nuclear Instruments and Methods in Physics Research Section A: Accelerators, Spectrometers, Detectors and Associated Equipment* **467**, 982-985 (2001).

124 Takeuchi, A., Suzuki, Y., Uesugi, K., Okada, I. & Iriguchi, H. Performance Test and Evaluation of Multilevel Fresnel Zone Plate with Three-Step Profile

Fabricated with Electron-Beam Lithography. *Japanese Journal of Applied Physics* **51**, 022502-022502 (2012).

125 Keskinbora, K., Grévent, C., Hirscher, M., Weigand, M. & Schütz, G. Single-Step 3D Nanofabrication of Kinoform Optics via Gray-Scale Focused Ion Beam Lithography for Efficient X-Ray Focusing. *Advanced Optical Materials*, 10.1002/adom.201400411-201400410.201401002/adom.201400411 (2014).

126 Erko, A. I., Aristov, V. V. e. & Vidal, B. *Diffraction X-ray optics*. (Institute of Physics Pub., 1996).

127 Roth, T., Alianelli, L., Lengeler, D., Snigirev, A. & Seiboth, F. Materials for x-ray refractive lenses minimizing wavefront distortions. *MRS Bulletin* **42**, 430-436 (2017).

128 Keskinbora, K., Sanli, U. T., Grévent, C. & Schütz, G. in *X-Ray Nanoimaging: Instruments and Methods II.* 95920H (International Society for Optics and Photonics).

129 Seiboth, F. *et al.* Perfect X-ray focusing via fitting corrective glasses to aberrated optics. *Nature Communications* **8** (2017).

130 Petrov, A. *et al.* Polymer X-ray refractive nano-lenses fabricated by additive technology. *Optics Express* **25**, 14173-14181 (2017).

131 Mirzaeimoghri, M. *et al.* Nano-printed miniature compound refractive lens for desktop hard x-ray microscopy. *PloS one* **13**, e0203319 (2018).

132 Lyubomirskiy, M. *et al.* Ptychographic characterization of polymer compound refractive lenses manufactured by additive technology. *arXiv preprint arXiv:1812.05897* (2018).

133 Ordavo, I. *et al.* A new pnCCD-based color X-ray camera for fast spatial and energy-resolved measurements. *Nuclear Instruments and Methods in Physics Research Section A: Accelerators, Spectrometers, Detectors and Associated Equipment* **654**, 250-257 (2011).

Acknowledgments

Here, I would like to acknowledge and thank the following people who contributed to the realization of this thesis:

Prof. Dr. Gisela Schütz and Dr. Corinne Grévent for believing in me and giving me the opportunity to research on this very interesting topic. I would like to thank them also for having their doors open at all times.

Dr. Kahraman Keskinbora, whom I shared the office in the first three years of my Ph.D., who then became my group leader and supervisor. He was always ready to help. We survived the night-shift beamtimes together. I would also like to thank him for the cover image of the thesis.

Prof. Dr. van Slageren for accepting to be the "Mitberichter" of my thesis and for our regular meetings about my Ph.D. project, his valuable comments and suggestions and finally for his very supportive attitude which made me feel safe.

Dr. Markus Weigand, Dr. Iuliia Bykova and Michael Bechtel for their support during the beamtimes.

Bernd Ludescher and Frank Thiele for their help in solving problems related to technical problems in ALD.

Dr. Hassan Gargouri for instructing me on the SENTECH ALD instrument and his help in ALD process development.

Dr. Hakan Ceylan for the 3D printing sessions and his belief and contribution to the 3D printed kinoform project.

Prof. Dr. Mato Knez, for giving me the opportunity to research in his department as a visiting researcher and his post-doc Dr. Keith Gregorczyk for his extreme effort during those 3 weeks in San Sebastian.

Prof. Dr. Gerd Schneider and Dr. Stefan Rehbein for providing the CWT software, which contributed a lot to the theoretical calculations.

Ulrike Eigenthaler for introducing me to the Dual-beam system.

Dr. Chengge Jiao for fabricating the micropillar arrays.

Every member of the Schütz Department who made the tough times bearable.

Members of the STEM group for their help in TEM/WDX analysis and valuable discussions. Particularly Prof. Dr. Peter van Aken, Dr. Fritz Philip, Dr. Wilfried Sigle, Dr. Vesna Srot, Dr. Yi Wang, Dr. Ekin Simsek Sanli, Kersten Hahn, Dr. Julia Deuschle, Felicitas Predel and Sabine Kühnemann.

Christian Wolter and Sigfried Hansel for fabricating the tilt stage.

The members of the micro-nano optics group, especially, Gül Dogan, Margarita Baluktsian and Lea Griessbach.

Department secretary Monika Kotz for her positive attitude and her help whenever I needed.

My parents and my brother, who supported me emotionally during the moments of lost hope.

My wife, Dr. Ekin Simsek Sanli for sharing my stress, for her support and her love. I would also like to thank her for her help in ALD experiments and for being in the lab with me during the holidays, proofreading my manuscripts and my thesis.

Curriculum Vitae

Personal Data

Name	Umut Tunca SANLI
Birthday	07 September 1986
Place of birth	Istanbul / Turkey

Education and Work Experience

April 2013 – March 2019 Stuttgart, Germany	Ph.D. student in the Modern Magnetic Systems Department at the Max Planck Institute for Intelligent Systems under supervision of Prof. Dr. Gisela Schütz
February 2013 – April 2013 Stuttgart, Germany	Research assistant in the Modern Magnetic Systems Department at the Max Planck Institute for Intelligent Systems
November 2012 – February 2013 Stuttgart, Germany	Teaching assistant at the University of Stuttgart
May 2011 – July 2012 Stuttgart, Germany	Master's Student at Robert Bosch GmbH (CR/ARY2). Thesis supervisor: Prof. Dr. Helmut Föll
September 2009 – August 2012 Kiel, Germany	International Master's Program at the Christian Albrechts University of Kiel in Materials Science
November 2007 – February 2008 Hamburg, Germany	Intern at the EADS Airbus Deutschland GmbH
April 2007 – October 2007 Hamburg, Germany	Erasmus student at the Technical University of Hamburg-Harburg

September 2004 – August 2009 Eskisehir, Turkey	B. Sc. in Materials Science and Engineering at Anadolu University. Thesis supervisor: Prof. Dr. Gürsoy Arslan

Awards

* Best Student Paper Award at the SPIE Optics and Optoelectronics Conference in Prague in 2015
* MSA Student Poster Award at the Microscopy & Microanalysis 2015 Meeting
* Grassroot funding award of the Max Planck Insitute (at the year 2016)

International Patent Applications

1. High-resolution full material Fresnel zone plate array and process for its fabrication; Umut T. Sanli, Kahraman Keskinbora, Gisela Schuetz, Chengge Jiao, EP, Application number: 17161526.3 (2018)
2. 3D-Printed X-ray Optics and Method for Producing the Same; Kahraman Keskinbora, Umut T. Sanli, Hakan Ceylan Gisela Schuetz, Metin Sitti. EP Application number: 18161035.3 (2018)

Journal Articles

1. Controlling dislocation nucleation-mediated plasticity in nanostructures via surface modification; Jungho Shin, Lisa Y. Chen, Umut T. Sanli, Gunther Richter, Stéphane Labat, Marie-Ingrid Richard, Thomas Cornelius, Olivier Thomas, Daniel S.Gianola; Acta Materialia; DOI: 10.1016/j.actamat.2018.12.048 (2018)
2. 3D Nanoprinted Plastic Kinoform X-Ray Optics ;Sanli, U. T., Ceylan, H., Bykova, I., Weigand, M., Sitti, M., Schütz, G., & Keskinbora, K. Advanced Materials, 30(36), 1802503. (2018).
3. Correction of axial position uncertainty and systematic detector errors in ptychographic diffraction imaging; Lars Loetgering, Max Rose, Kahraman Keskinbora, Margarita Baluktsian, Gül Dogan, Umut Sanli, Iuliia Bykova, Markus Weigand, Gisela Schütz, Thomas Wilhein; Optical Engineering 57, 8, p.084106; DOI: 10.1117/1.OE.57.8.084106 (2018)

4. High-throughput synthesis of modified Fresnel zone plate arrays via ion beam lithography; Kahraman Keskinbora, Umut Tunca Sanli, Margarita Baluktsian, Corinne Grévent, Markus Weigand, Gisela Schütz; Beilstein journal of nanotechnology 9, 1, 2049-2056, DOI: 10.3762/bjnano.9.194 (2018)
5. 3D nanofabrication of high-resolution multilayer Fresnel zone plates; Umut Tunca Sanli, Chengge Jiao, Margarita Baluktisan, Corinne Grévent, Kersten Hahn, Yi Wang, Vesna Srot, Gunther Richter, Iuliia Bykova, Markus Weigand, Gisela Schütz, Kahraman Keskinbora; Advanced Science 5, 9, 10800346; DOI: 10.1002/advs.201800346 (2018)
6. Comparative study of ALD SiO_2 thin films for optical applications; Kristin Pfeiffer, Svetlana Shestaeva, Astrid Bingel, Peter Munzert, Lilit Ghazaryan, Cristian van Helvoirt, Wilhelmus MM Kessels, Umut Tunca Sanli, Corinne Grévent, Gisela Schütz, Matti Putkonen, Iain Buchanan, Lars Jensen, Detlev Ristau, Andreas Tünnermann, Adriana Szeghalmi; Optical Materials Express 6, 2, 660-670; DOI: 10.1364/OME.6.000660 (2016)
7. Multilayer Fresnel zone plates for high energy radiation resolve 21 nm features at 1.2 keV; Kahraman Keskinbora, Anna-Lena Robisch, Marcel Mayer, Umut T. Sanli, Corinne Grévent, Christian Wolter, Markus Weigand, Adriana Szeghalmi, Mato Knez, Tim Salditt, Gisela Schütz; Optics Express 22, 15 18440-18453; DOI: 10.1364/OE.22.018440 (2014)

Proceeding Articles

1. Soft X-ray ptychography for imaging of magnetic domains and skyrmions in sub-100 nm scales; Iuliia Bykova, Kahraman Keskinbora, Umut Sanli, Joachim Gräfe, Michael Bechtel, Guoqiang Yu, Eberhard Goering, Hermann Stoll, Gisela Schütz, Markus Weigand; Microscopy and Microanalysis 24, S2, 36-37; DOI: 10.1017/S1431927618012606 (2018)
2. New concepts for 3D optics in X-ray microscopy; Umut Tunca Sanli, Hakan Ceylan, Chengge Jiao, Margarita Baluktsian, Corinne Grevent, Kersten Hahn, Yi Wang,

Vesna Srot, Gunther Richter, Iuliia Bykova, Markus Weigand, Metin Sitti, Gisela Schütz, Kahraman Keskinbora; Microscopy and Microanalysis 24, S2, 292-293; DOI: 10.1017/S1431927618013788 (2018)

3. Micromachining of Si_3N_4 by Ga^+ ion implantation and dry etching; Margarita Baluktsian, Kahraman Keskinbora, Umut T. Sanli, Gisela Schütz; Microscopy and Microanalysis 22, S3, 170-171; DOI: 10.1017/S1431927616001707 (2016)
4. High-resolution high-efficiency multilayer Fresnel zone plates for soft and hard X-rays; Umut Tunca Sanli, Kahraman Keskinbora, Keith Gregorczyk, Jonas Leister, Nicolas Teeny, Corinne Grévent, Mato Knez, Gisela Schütz; Proceedings of SPIE Volume 9592, 95920F; DOI: 10.1117/12.2187795 (2015)
5. Fabrication and X-ray testing of true kinoform lenses with high efficiencies; Kahraman Keskinbora, Umut Tunca Sanli, Corinne Grévent, Gisela Schütz; Proceedings of SPIE Volume 9592, 95920H; DOI:10.1117/12.2187896 (2015)
6. Multilayer Fresnel zone plates for X-ray microscopy; Umut T. Sanli, Kahraman Keskinbora, Corinne Grevent, Adriana Szeghalmi, Mato Knez, Gisela Schütz; Microscopy and Microanalysis 21, S3, 1987-1988; DOI: 10.1017/S1431927615010715 (2015)
7. Focused ion beam micromachining enables novel optics for X-ray microscopy; Kahraman Keskinbora, Umut T. Sanli, Corinne Grevent, Michael Hirscher, Gisela Schütz; Microscopy and Microanalysis 21, S3, 1983-1984; DOI: 10.1017/S1431927615010697 (2015)
8. Overview of the multilayer-Fresnel zone plate and the kinoform lens development at MPI for Intelligent Systems; Umut Tunca Sanli, Kahraman Keskinbora, Corinne Grévent, Gisela Schütz; Proceedings of SPIE Volume 9510, 95100U; DOI: 10.1117/12.2186321 (2015)